El sesgo secundario de halos de materia oscura

Iker Fernández Sánchez

Tutors:
Dr. Andrés Balaguera Antolínez
Dr. Ginevra Favole

San Cristóbal de La Laguna, 2024

Este Trabajo de Fin de Máster está dedicado a todos aquellos que, con su apoyo y guía, han hecho posible la culminación de este proyecto.

Quiero expresar mi más sincero agradecimiento a mis tutores, los doctores Andrés Balaguera Antolínez y Ginevra Favole. Su constante guía, paciencia y apoyo han sido fundamentales para la realización de este proyecto. Sin su conocimiento y dedicación, este trabajo no habría sido posible. Agradezco profundamente las horas de discusión, las valiosas sugerencias y el ánimo incondicional que me han brindado a lo largo de todo el proceso.

También quiero agradecer a mis padres José Luis y Patricia, a mi hermano Jon y a mi pareja Iratxe, cuyo apoyo incondicional me ha dado la fuerza y la motivación para seguir adelante en los momentos más difíciles. Gracias por creer en mí y por estar siempre a mi lado. Habéis sido la luz que me ha iluminado estos últimos meses.

Finalmente quiero extender mi gratitud a mis amigos de toda la vida, en especial a HK, y a aquellos que han ido apareciendo durante mi formación académica, como mis compañeros de CF Ulrich y de Cosmo y Wanda. Vuestro apoyo, amistad y compañerismo han sido esenciales para mantenerme motivado y enfocado. Este logro es también vuestro.

Abstract

La mejora de las técnicas observacionales en experimentos (tales como Euclid, eBOSS, DESI, JPAS) ha permitido incrementar considerablemente el número de trazadores (galaxias, cúmulos de galaxias), el volumen observado del Universo y la precisión en las mediciones de distintos observables astrofísicos y cosmológicos a partir de los cuales es posible inferir información cosmológica. Para analizar e interpretar las señales medidas a partir de dichos experimentos, es necesario entender con exactitud los procesos físicos que dan lugar a la estructura a gran escala. Con este objetivo, se usan simulaciones de N-cuerpos, en los que la gravedad está resuelta de forma exacta y de donde es posible extraer las estadísticas más representativas de la distribución de trazadores, para ser comparadas con los modelos teóricos y las observaciones. En un escenario más realista, la necesidad de involucrar los efectos de bariones (que a pesar de representar $< 1\%$ de la materia visible, son los responsables del Universo observado) ha impulsado la producción de simulaciones hidrodinámicas tales como la IllustrisTNG. A partir de dichas simulaciones, podemos entender la conexión entre la materia visible (galaxias) y la componente de materia oscura (no observable directamente) que contiene la información cosmológica. El estudio de dicha conexión en distintos observables tanto astrofísicos como cosmológicos es el objetivo de este trabajo.

Para comenzar, se realiza una introducción al modelo cosmológico estándar, pasando a través del Universo homogéneo hasta la formación de los halos de materia oscura (bloques fundacionales para describir la distribución espacial de galaxias en el paradigma ΛCDM). Se discutirán algunas de sus propiedades estadísticas más relevantes (abundancia y distribución espacial). A continuación se ha analizado el contendido de las simulaciones TNG. En particular, se han medido las relaciones de escala entre propiedades de subhalos de materia oscura (masa, velocidad circular máxima, dispersión de velocidades, momento angular específico y metalicidad). Específicamente, estas relaciones han sido cuantificadas como función de la masa de los subhalos y halos que las hospedan. A través de la medición de los cuatro primeros momentos de estas relaciones de escala (media, varianza, oblicuidad y curtosis) y los coeficientes de correlación entre ellas, se han caracterizado las propiedades estadísticas de la misma, analizando por ejemplo la compatibilidad de esta con funciones conocidas (como la distribución normal). Las relaciones medias han sido ajustadas y comparadas con predicciones teóricas (basadas algunas en la suposición de equilibrio virial).

Como aporte fundamental del trabajo, hemos estudiado el comportamiento de las relaciones de escala de subhalos como función de variables asociadas con el ambiente (o entorno). En este trabajo, hemos introducido dos definiciones de entorno: la masa del halo que alberga a los subhalos y la estructura de la red-cósmica en la que residen estos halos.

Para determinar las propiedades de la red cósmica, en este trabajo realizamos un análisis de las propiedades del campo de materia oscura de la TNG. En particular, partiendo de la distribución de partículas de materia oscura, se ha construido el campo de densidad (mediante la implementación de métodos de interpolación) a partir del cual se han medido las distribuciones de densidad (estadística de un punto), el espectro de potencias (estadística de dos puntos) y el tensor de mareas. Estas mediciones han sido comparadas con predicciones teóricas y ajustes a simulaciones de materia oscura, mostrando pequeñas diferencias que son entendibles dadas las características de la TNG (resolución, contenido físico).

Basados en el campo de densidad de materia oscura de la TNG, se ha aplicado una clasificación de estructuras de la red cósmica que utiliza los autovalores del tensor de mareas como diagnósticos para discriminar ambientes tales como nudos o vacíos cósmicos. Con estos mismos autovalores hemos definido cantidades que caracterizan el grado de anisotropía del ambiente en que habitan los halos de materia oscura. Esto nos permite explorar el comportamiento de las relaciones de escala en distintos ambientes (es decir, en regiones con distintos niveles de anisotropia y/o densidad de materia oscura). Este tipo de análisis es de gran importancia para lograr establecer un vínculo galaxia-halo que ayude a interpretar de forma más exacta las observaciones de los censos de galaxias. Esto, ya que este análisis eventualmente introduce la necesidad de incluir dependencias secundarias dentro del llamado "modelo de ocupación de galaxias", pieza fundamental para entender la distribución espacial de galaxias en el Universo.

Finalmente, otro aporte de este trabajo consiste en el análisis de la estructura a gran escala en la TNG, tanto de la materia oscura como de los halos y subhalos. En particular, hemos implementado un método para asignar de forma individual información sobre agrupamiento a gran escala. Dicha información (denominada sesgo) representa la relación de escala entre el agrupamiento de trazadores y el agrupamiento de materia oscura subyacente, como respuesta a la gravedad. Tal y como se han analizado las relaciones de escala, el estudio del sesgo como función de la masa de los halos y subhalos se realiza en distintos ambientes cosmológicos mostrando cómo dichos ambientes (caracterización a pequeñas escalas) tienen un efecto directo sobre la distribución espacial de trazadores a gran escala. Por último, se estudia la señal de sesgo secundario (o sesgo de ensamblaje), la cual presenta relevancia a nivel teórico como observacional.

Las conclusiones que se obtienen de este trabajo son que los entornos considerados, efectivamente, afectan en las relaciones de escala. La principal razón del cambio de estas con respecto a la masa del halo en el que residen radica en las fuerzas de marea, las cuales serán más intensas en los halos más masivos. Las relaciones de escala, teniendo en cuenta las estructuras de la red cósmica, nos muestran que los entorno más anisotrópicos tenderán a tener unas pendientes más pronunciadas. Finalmente, vemos con respecto al sesgo, veremos que el agrupamiento es mayor tanto en los halos como en los subhalos a redshifts altos, debido a la rareza de picos de fluctuaciones de densidad donde se forman los halos. Veremos también que tanto los halos como los subhalos presentan una señal de sesgo secundario con respecto a la densidad de la materia oscura y a las propiedades de los subhalos, respectivamente.

Contents

1. Introduction

1.1. Preliminaries

1.1.1. Objectives

The main objectives of this master's thesis were

- To understand the physical processes that give rise to the large-scale structure.
- To study the connection between visible matter and dark matter in different astrophysical and cosmological observables.
- To characterize the scaling relations of the properties of the subhalos as a function of the mass of the subhalos and halos in which they live.
- To analyze how different environments, such as the mass of halos or the structure of the cosmic-web, in which the subhalos live affect the scaling relations, the distribution and the abundance of subhalos, and their evolution with redshift.
- To understand and measure the density distribution (one-point statistics), the power spectrum (two-point statistics), and compare them with theoretical predictions and fits from dark matter simulations
- To calculate the effective bias of the halos and subhalos and see its connection to the large-scale analysis.
- To calculate the secondary bias of the halos and the subhalos with respect to different properties.

1.1.2. Main bibliography sources

The main sources from which this first section we are based on a number of textbooks and reviews, among others: (Weinberg, 1972 ; Rindler, 1977 ; Peebles, 1980 ; Dodelson, 2003 ; Cepa, 2007 ; Mo et al., 2010).

1.1.3. Organization of this work

The structure of this master's thesis is as follows. In the following subsections within §1, an introduction to the standard cosmological model is given, passing through the homogeneous Universe up to the formation of dark matter halos. In §2 we introduce the Illustris TNG simulation. In addition we also present the populations of halos and subhalos. The theoretical framework and predictions of the scaling relations are presented in §3 together with the most basic scaling relations. §4 discusses the relationship between the scaling relations and the large-scale structure. The connection between bias and large scale is developed in §5. Finally, the conclusions of this master's thesis are presented in §6.

1.2. The large-scale Universe

The Standard Cosmological Model is based on the "cosmological principle" according to which the Universe is statistically homogeneous and isotropic on very large scales. This model combines the theory of General Relativity with assumptions on the content of matter and energy to describe the evolution of the Universe on large-scales. The so-called ΛCDM model is the most successful model as it has been shown to explain a wide range of cosmological observations and measurements (e.g. Cosmic Microwave Background radiation, Type Ia supernovae and galaxy clustering, weak lensing). This model is mainly based on two concepts: the cosmological constant, Λ, responsible for the accelerated expansion of the Universe (and an special form of what is called dark energy), along with a cold dark matter component (Planck Collaboration, 2016a), a type of matter that only interacts through gravitation and whose velocity is well below the relativistic limit. The presence of this component is a necessary condition for the formation of structures.

In the Standard Cosmological Model, the geometry of space-time is determined by the matter/energy content of the Universe through the Einstein field equation

$$R_{\mu\nu} - \frac{1}{2}g_{\mu\nu}R - g_{\mu\nu}\Lambda = \frac{8\pi G}{c^4}T_{\mu\nu}, \tag{1}$$

where $R_{\mu\nu}$ is the Ricci tensor, describing the local curvature of space-time, $g_{\mu\nu}$ is the metric (defined as $\mathrm{d}s^2 = g_{\mu\nu}\mathrm{d}x^\mu\mathrm{d}x^\nu$), R is the Ricci curvature scalar (defined as the trace of the Ricci tensor), $T_{\mu\nu}$ is the energy-momentum tensor of the matter

content in the Universe. Under the assumption of homogeneity and isotropy, the energy-momentum tensor adopts the ideal fluid (i.e., a fluid in which viscosity forces can be neglected) form

$$T_{\mu\nu} = (\rho + p/c^2)u_\mu u_\nu + pg_{\mu\nu}, \tag{2}$$

where u_α is the four-velocity of the fluid, ρc^2 is the energy density and p is the pressure. For a homogeneous and isotropic Universe, an anzats for the solution of the field equation (which is a differential equation for the metric $g_{\mu\nu}$) is given by the Friedmann-Robertson-Walker (FRW) metric, expressed in spherical coordinates as

$$ds^2 = g_{\mu\nu}dx^\mu dx^\nu = -dt^2 + a^2(t)\left[\frac{dr^2}{1 - Kr^2} + r^2 d\Omega^2\right], \tag{3}$$

where $a(t)$ denotes the scale factor and K the curvature. The curvature is normalized as $K \in -1, 0, 1$ for open ($K = -1$), flat ($K = 0$) or closed ($K = 1$) Universe (curvature) respectively. The FRW metric is the way to measure distances in a Universe whose physical separations are modulated by the evolution of the scale factor, such that the proper coordinates **r** and the comoving coordinates **x** are related as $\mathbf{r} = a(t)\,\mathbf{x}$. The comoving separation between two observers corresponds to the distance of two points that share the same angular location in the sky but at different times. From Eq. (3), and assuming that an observer is at t=0 and other observer is at time t, this distance is written as

$$\xi(t) = \int_0^t \frac{dt'}{a(t')} = \int_0^z \frac{a}{\dot{a}}dz', \tag{4}$$

where z is the cosmological redshift defined as $z = 1/a - 1$. From Eq. (3), the proper distance between two observers located at some radial coordinate ξ can be written as

$$d_T \equiv r[\xi(z)] = \begin{cases} a \sin\left(\int_0^z \frac{a}{\dot{a}}dz'\right) & k = +1 \\ \int_0^z \frac{a}{\dot{a}}dz' & k = 0 \\ a \sinh\left(\int_0^z \frac{a}{\dot{a}}dz'\right) & k = -1. \end{cases} \tag{5}$$

The measurement of cosmological distances helps us to infer the cosmological parameters because the distance depends directly on these parameters through the so-called Hubble function which is defined as $H = \dot{a}/a$ and represents the expansion rate of the Universe. There are other distances, such as the luminosity distance, which is used to calculate the distance to objects that emit radiation, $d_L(z) = d_T(z)(1 + z)$.

The time-variation of the different energy-density components can be specified as solutions to the conservation laws. In particular, the conservation of the energy-momentum tensor (i.e. Eq. 2), can be shown to reduced to a cosmological mass conservation equation of the form

$$\dot{\rho} + 3(\rho + p)\frac{\dot{a}}{a} = 0. \tag{6}$$

This equation states that the energy density of the Universe ρ varies due to the expansion of the Universe. The mass conservation equation is complemented with an equation of state $p = \omega\rho^\gamma$, characterizing the cold dark matter ($\omega = 0$), radiation ($\omega = 1/3, \gamma = 1$), cosmological constant ($\omega = -1, \gamma = 1$), dark energy ($-1 < \omega < 0$). The integration of Eq. (6) yields to solutions of the form $\rho(t) \propto a(t)^{3(1+\omega)}$. The energy density is often written in terms of the density parameter

$$\Omega_i(z) \equiv \frac{8\pi G\rho_i(t)}{3H^2(z)} \equiv \frac{\rho_i(z)}{\rho_{crit}(z)}, \tag{7}$$

where ρ_{crit} is the so-called *critical density* which is the density required to make the Universe geometrically flat. If $\rho > \rho_{\text{crit}}$ ($\rho < \rho_{\text{crit}}$) the Universe is closed (open). Introducing the solutions of the FRW metric (Eq. 3) into the field equations (Eq. 1) using the momentum-energy tensor of an ideal fluid (Eq. 2), we obtain the Friedman equation:

$$H(z) \equiv \frac{\dot{a}}{a} = \left(\Omega_{de}(1 + z)^{-3(\omega+1)} + (1 - \Omega_0)(1 + z)^2 + \Omega_{m,0}(1 + z)^3 + \Omega_{r,0}(1 + z)^4\right)^{1/2} H(z = 0), \tag{8}$$

where $H(z = 0) \equiv H_0$ is the Hubble parameter. Equation (8) determines the evolution of the scale factor as a function of a

cosmic time t and the cosmological parameters. Friedman equation can be then understood as a cosmic normalization rule $\sum_i \Omega_i = 1$.

1.3.   The inhomogeneous Universe

In the Standard Cosmological Model the Universe is assumed to be highly homogeneous at early times and on large scales. The structures observed today are assumed to have grown from small density perturbations due to the action of gravity. As demonstrated by *Cosmic Microwave Background* (CMB) experiments (see e.g., FIRAS, Fixsen et al., 1996; WMAP, Bennett et al., 2013; PLANCK, Planck Collaboration, 2016a), these perturbations are shown to be drawn from a Gaussian distribution. Departures from the large-scale homogeneous Universe reveal fluctuations in the density of matter which evolve under the influence of gravity, leading to the formation of structures we observe today. The analysis of the growth of these fluctuations can be developed using perturbative approach, where the basic equations of the dynamics of a fluid (conservation laws for momentum, mass and energy) can be expressed as a function of density perturbations $\delta(\mathbf{r})$

$$\delta(\mathbf{r},z) = \frac{\rho(\mathbf{r},z) - \bar{\rho}(z)}{\bar{\rho}(z)}, \tag{9}$$

where $\bar{\rho}(z)$, is the mean matter density of the Universe as a function of the redshift defined as $\bar{\rho}(z) = \rho_{\rm crit}(z)\Omega_m(z)$. It can be shown that in the linear order of cosmological perturbations ($\delta \ll 1$) for a pressureless fluid, the fluctuations in Fourier space $\delta(\mathbf{k},z)$ evolve independently following (see e.g., Mo et al., 2010)

$$\frac{{\rm d}^2\delta(\mathbf{k},z)}{{\rm d}t^2} + 2H(t)\frac{{\rm d}\delta(\mathbf{k},z)}{{\rm d}t} = 4\pi\bar{\rho}\delta(\mathbf{k},z). \tag{10}$$

Heath (1977) showed that this equation has a growing solution,

$$\delta_+(\mathbf{k},z) \propto H(z) \int_z^\infty \frac{(1+z')}{E^3(z')} {\rm d}z', \tag{11}$$

where $E(z) = H(z)/H(z=0)$. This is usually dubbed as the "growing mode", with analytical solutions for some particular cosmological models (see e.g., Peebles, 1980; Percival, 2005; Ryden, 2017). This growing solution tells us how perturbations in matter grow linearly in time.

The level of inhomogeneity in the Universe can be determined by assessing the statistical properties of the spatial distribution of matter and its tracers (see e.g. Dodelson, 2003; Padmanabhan, 1993; Peebles, 1980). In particular, we can mention the *two-point statistics* of the spatial distribution, both in configuration (correlation function) and in Fourier space (the power spectrum). In configuration space, the two-point statistics is represented by the *correlation function* $\xi(r)$ defined as $\xi(r = |\mathbf{r}|) = \langle\delta(\mathbf{r}')\delta(\mathbf{r}+\mathbf{r}')\rangle_{\mathbf{r}}$, where the symbols $\langle\rangle$ denotes an ensemble average, which according to the ergodic theorem can be equivalent to an average over the volume, and $\delta(\mathbf{r})$ denotes an overdensity at position $\mathbf{r}$ in space. This quantity is interpreted as the excess probability of having pairs separated by a distance $\mathbf{r}$ with respect to a random distribution (Peebles, 1980). Its Fourier counterpart, the *power spectrum $P(k)$*, is defined as

$$\langle\delta(\mathbf{k})\delta^*(\mathbf{k} + \mathbf{k}')\rangle = (2\pi)^3 P(k = |\mathbf{k}|)\delta_D^3(\mathbf{k} + \mathbf{k}'), \tag{12}$$

where the underlying assumption of isotropy is encapsulated in the fact that all information can be condensed as a function of $k = |\mathbf{k}|$(and $r = |\mathbf{r}|$ for the correlation function). Theoretical predictions for the linear dark-matter power spectrum can be produced from the solution of Boltzmann equation and the so-called transfer functions $T(k)$ (see e.g., Dodelson, 2003), with $P(k,z) = Ak^n|T(k)|^2(\delta_+(z)/\delta_+(z=0))^2$ where n is the "index of primordial fluctuations" and the amplitude A a normalization (proportional to the variance of the mass distribution). These examples of two-point statistics are sufficient to statistically describe the large scale distribution of matter in the Universe if the overdensity follows a Gaussian distribution. At low redshift, higher-order statistics (e.g., the bispectrum or the three-point correlation function) are developed through gravitational instability (see e.g., Pollack et al., 2012; Smith et al., 2007).

A perturbative approach on top of the cosmological model can predict the clustering of dark matter in virialized structures called dark-matter halos which represent the building blocks for the spatial distribution of galaxies. The formation of dark matter halos can be understood using the spherical collapse model (see e.g., Gunn and Gott, 1972), in which a region with (dark)

matter decouples from the Hubble expansion and collapse to generate bound structures in approximated virial equilibrium ($2K = -W$ where K is the total kinetic energy and W the gravitational potential energy), characterized by an overdensity $\Delta_{\mathrm{vir}} \approx (18\pi^2 + 60x - 32x^2)/\Omega_{\mathrm{m}}$, where $x = \Omega_m(z) - 1$ (Bryan and Norman, 1998). Baryons fall into these potential wells and radiate, according to the depth of these potential wells, to build visible structures such as galaxy clusters and galaxies (see e.g., Mo et al., 2010).

A key quantity in the statistical analysis of dark matter tracers is the abundance (one-point statistics or halo mass function), which quantifies the number of tracers in a certain halo mass bin in a cosmological volume at a given redshift. In order assess this quantity, theoretical attempts such as the abundance of peaks (Bardeen et al., 1986a)or the excursion set (Press and Schechter, 1974; Sheth and Tormen, 1999) can be applied. In general, dark matter halos are assumed to be the result of collapsing regions with a linearly extrapolated overdensity above a critical value $\delta_c \approx 1.68$. The statistics of halos usually described n terms of the peak height $\nu = \delta_c/\sigma(M,z)$, where

$$\sigma(M,z)^2 = \langle (\delta(\mathbf{r}) \otimes W_R(\mathbf{r}))^2 \rangle = \frac{1}{2\pi^2} \int_0^\infty P(k)W_R^2(kR)k^2 \mathrm{d}k, \tag{13}$$

is the variance in the density fluctuations filtered at a scale $R \sim 8$ Mpch^{-1} (where the symbols $\langle \rangle$ denotes an ensemble average[1]) enclosing a mass $M \propto \bar{\rho}(z)R^3$. The mass function is defined as

$$n(M,z)\mathrm{d}M = \frac{\bar{\rho}(z)}{M}f(\nu)\left|\frac{\mathrm{d}\ln\nu}{\mathrm{d}\ln M}\right|\mathrm{d}M, \tag{14}$$

where $f(\nu)$ denotes the so-called "multiplicity function", accounting for the fraction of mass associated with halos in a given bin of $\ln\nu$ (see e.g. Sheth and Tormen, 1999).

The spatial distribution of tracers in redshift space (where peculiar velocities alter the clustering pattern) can also be modeled to certain extent using linear perturbation theory (see e.g., Kaiser, 1987; Peebles, 1980). The link between the clustering of dark matter halos and its underlying dark matter density filed is dubbed "bias" (see e.g., Dekel and Lahav, 1999; Mo et al., 2010; Peacock, 1998; Peebles, 1980, for a few examples). The concept of bias is very broad and has several definitions, such as stochastic bias or deterministic bias, among others (Mo et al., 2010). It is well known that the bias of dark matter tracers must be considered beyond the linear scale-independent scheme (see e.g., Desjacques et al., 2018, , and references therein), where the fluctuations of the halo number density δ_h can be written as a bias factor $b(\mathbf{r}, z)$ multiplied by the fluctuations of the underlying matter density δ_{dm}, i.e., $\delta_h(\mathbf{r}, z) = b(\mathbf{r}, z)\delta_{dm}(\mathbf{r}, z)$. In order to make the distinction between large and small scales, we start from perturbations of the density field in Fourier space, where perturbations in the linear regime evolve independently. In this work, we aim at measuring the large-scale effective bias, which is based on the renormalization of the linear coefficients involved in the perturbative expansion of the density field. In Fourier space, the effective bias estimators are built from the ratio of the halo $P_{hh}(k)$ and matter power spectra as $P_{\mathrm{dm}}(k)$ (see e.g., Pollack et al., 2012; Smith et al., 2007):

$$b_{hh}(k) = \sqrt{\frac{P_{hh}(k)}{P_{\mathrm{dm}}(k)}}, \tag{15}$$

or as the ratio of the halo-matter cross spectrum $P_{hm}(k)$ to the matter spectrum:

$$b_{hm}(k) = \frac{P_{hm}(k)}{P_{\mathrm{dm}}(k)}. \tag{16}$$

In both cases, the estimate of effective bias can be obtained by averaging the its values over a wavenumber range $k < k_{max}$ in which the ratio between the halo and dark matter power spectra is constant. As mentioned, we discuss the bias and the connection to large-scale analysis in §5.

The clustering of light-emitting tracers (such as galaxies, galaxy clusters) demands another level of biasing schemes, linking these to the distribution of dark matter halos, in what is usually called "the halo model of galaxy distribution" (Cooray and Sheth, 2002).

---

[1]Ensemble average refers to the mean of a quantity over all possible realizations of a system under the same macroscopic conditions (see e.g,, Peebles, 1993).

1.4. Cosmological probes

There are different observables we can measure in the Universe using e.g., galaxy and/or galaxy cluster surveys, from which cosmological information can be inferred through a likelihood analysis (see e.g., Appleby et al., 2023; Bennett et al., 2013; DESI Collaboration, 2024; Euclid Collaboration et al., 2020; Ivanov et al., 2020; Planck Collaboration, 2016a). Such approach allows us to constraint the set of parameters of a given model, or to assess whether a model is sufficient to describe the observations. The theory of general relativity has passed several tests on a wide ranges of scales, such as the prediction of the precession of Mercury's perihelion (Einstein, 1915), time dilation in everyday applications like GPS (Ashby, 2003) (where relativistic corrections are necessary), or the deflection of light due to massive objects (Eddington, 1919).

The ΛCDM model has a minimum number of parameters, namely, the baryon fraction $\Omega_b h^2$, the CDM fraction $\Omega_c h^2$, the reionization optical depth τ, the scalar spectral index n_s, the Hubble parameter H_0 and the amplitude of the primordial density fluctuations A_s. These parameters can be constrained using measurement of a number of statistical properties of the distribution of different tracers, such as galaxies, galaxy clusters, the cosmic-microwave background radiation, Supernovae and weak lensing. Each of this probe generate constants on different combinations of the cosmological parameters and, depending on the properties of the experiment, with different precision.

Bennett et al. (2013); Fixsen et al. (1996); Planck Collaboration (2016a) measured the angular fluctuations of the CMB temperature and from these measurements the six parameters describing the ΛCDM model are obtained. These parameters are a function of the reduced Hubble parameter which is defined as the dimensionless value of the current Hubble parameter, i.e. $h \equiv H_0/(100 \mathrm{kms}^{-1}\mathrm{Mpc}^{-1})$. Table 4 in Planck Collaboration (2016a) and Table 17 in Bennett et al. (2013) show the best fit for the parameters of the ΛCDM model with their uncertainties derived from the measurements of angular power spectrum in the cosmic-microwave background radiation (see **CMB**, below).

- **Clustering.** Several important experiments have been designed to measure the main statistical properties, such as the power spectrum and the two-point correlation function of the galaxy distribution (Balaguera-Antolínez et al., 2018; Dawson, 2016; DESI Collaboration, 2024; Lahav, 2002; Planck Collaboration, 2016b; Sánchez et al., 2009), in order to measure some cosmological information, like the expansion of the Universe.

  In general, the correlation function and the power spectrum deliver the same cosmological information. However, they are measured using different estimators which are prone to different systematic effects which must be taken int account in order to deliver unbiased cosmological information (see e.g. Feldman et al., 1994; Tegmark et al., 1998, and references therein)

- **CMB.** Since the discovery of the cosmic-microwave background radiation (CMB) (Penzias and Wilson, 1965), the physical and statistical properties of this radiation became a fundamental probe in modern cosmology. Over the last three decades several experiments (see e.g. Bennett et al., 2013; Fixsen et al., 1996; Planck Collaboration, 2016a) have been carried out, aiming to improve the accuracy and precision of the observations and characterize the properties of the CMB. The CMB radiation is characterized by a black-body spectrum with a temperature of $T_{\mathrm{CMB}} = 2.725 \pm 0.001K$ (Fixsen and Mather, 2002; Fixsen et al., 1996), which yields to a density parameter of radiation $\Omega_{\mathrm{rad}} \simeq 2.5h^{-2} \times 10^{-5}$. On the other hand, in spite of the isotropy it shows on the sky, most information is encoded in its anisotropies (White et al., 1994) which were measured as one part in $\Delta T/T \sim 10^{-5}$ (Smoot et al., 1992). The statistical properties of these anisotropies, represented by the angular power spectrum, have demonstrated the success of linear perturbation theory and general relativity to describe the physics of the early Universe.

- **Abundance.** One method to extract cosmological information is the measurements of the abundance of dark matter tracers, (e.g., galaxies or galaxy clusters), as a function of their intrinsic properties, such as stellar mass or luminosities in a given band (see e.g., Abbott and DES Collaboration, 2020; Fumagalli et al., 2024; Lesci et al., 2022). The mass function has cosmological information but we cannot observe it, since the mass of the halos is not a direct observable. Therefore, we have to observe the abundance of the tracers through another intrinsic property θ, which will be given by the θ function $\Phi(\theta,z)$. The observed abundance is linked to cosmological information through the so-called scaling relations (see e.g., Balaguera-Antolinez et al., 2012; Mo et al., 2010) which translate the observed properties into quantities in which models of abundance are directly written, such as the mass of dark matter halos. For example,

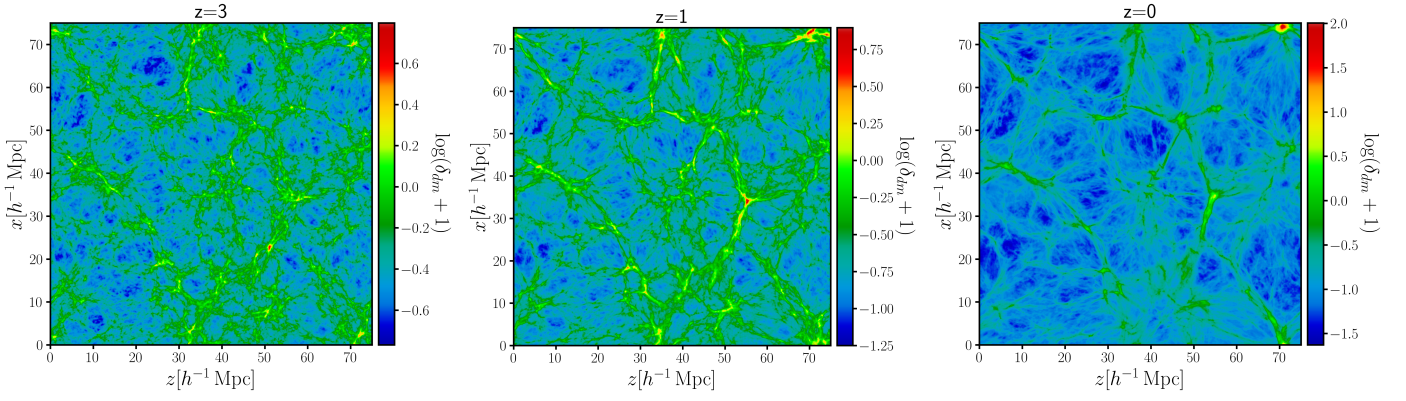$$\Phi(\theta,z) = \int_0^\infty P(\theta|M,z)n(M,z)\mathrm{d}M \tag{17}$$

Figure 1: TNG100 slices, with $10 \times 75 \times 75 \ h^{-3}$ Mpc^3 size, showing the dark matter density field at different redshifts using CIC interpolation and a grid of 512^3 cells. From left to right, the redshifts are $z = 3$, $z = 1$ and $z = 0$. The maps are color-coded by the value of the logarithm of density in each cell of the grid.

is the abundance as a function of θ at redshift z where $n(M,z)$ is the mass function of dark matter halos at redshift z, and $P(\theta|M,z)$ is the probability distribution of the property θ conditional to the halo mass at a redshift z (here θ means an specific property). Throughout this work we will refer to this type of conditional probability distributions as to "scaling relations" (or CDF).

- **Weak lensing.** Gravitational lensing is the deflection of light rays from distant objects due to matter along their path to us. Weak lensing is the limit in which these deflections cause modifications to the properties of the object without being visually apparent, of the order of 1% on angular scales of a few arcminutes (see e.g.. Kilbinger, 2015 ; Dodelson, 2017). Light rays coming from objects that are close in the sky must have passed through the same structures in the cosmic web, so the shape of the lights we see will be correlated by the lensing. This correlation decreases with separation on the sky (see e.g., Bartelmann and Maturi, 2016), and its amplitude can be used to determine the underlying matter distribution and thus the evolution in time of the cosmic structure. Hence, the information of the dark energy properties can be obtained.

- **Supernovae.** Type Ia supernovae, which are exploding stars, are among the most luminous events in the Universe. These processes usually have well-calibrated light profiles and constitute an important field of research (see e.g., Arnett, 1996; Branch and Wheeler, 2017). Most importantly, type Ia supernovae provided the first evidence that the Universe is expanding at an accelerated rate (Perlmutter et al., 1999; Riess et al., 1998).

  The cosmological relevance of the supernovae is that they represent standard candles from which cosmological distances can be inferred. Supernovae light curves (i.e, the change in luminosity over time) rise very rapidly and decay gradually over time, enabling us to measure both their apparent magnitude m and absolute magnitude M. The latter is measured by fitting the light curve with empirical and calibrated observations using supernovae in galaxies with known distances (or redshifts) (Riess et al., 1998). These can be linked to the cosmological information through the luminosity distance, namely $M(z) = m + 5 - 5\log(d_L(z)/10\text{pc})$ (see e.g., Cepa, 2007; Mo et al., 2010).

2. N-body hydro-simulations: Illustris TNG

2.1.   Description of the simulation

The analysis presented in this master's thesis is based on the IllustrisTNG[2] (Weinberger et al., 2016 ; Marinacci et al., 2018 ; Naiman et al., 2018 ; Nelson et al., 2018 ; Pillepich et al., 2018 ; Springel et al., 2018) magneto-hydrodynamical cosmological simulations that model the formation and evolution of galaxies within the ΛCDM paradigm. It builds upon the scientific achievements of the Illustris simulation (Vogelsberger et al., 2014a,b ; Genel et al., 2014), run with the AREPO moving-mesh code (Springel, 2010). Among other things, TNG updates include magnetic fields, a revised galactic wind scheme and a new Active Galactic Nuclei (AGN, hereafter) feedback model. The simulations include sub-grid models that take into account star

---

[2]https://www.tng-project.org/

formation, chemical enrichment of SNII, SNIa and AGB stars, stellar feedback, radiative cooling of metallic lines and AGN feedback. The IllustrisTNG simulations adopt the standard ΛCDM cosmology (Planck Collaboration, 2016a), with parameters $\Omega_m = 0.3089$, $\Omega_b = 0.0486$, $\Omega_\Lambda = 0.6911$, $H_0 = 100h$ km s^{-1} Mpc^{-1} with $h = 0.6774$, $\sigma_8 = 0.8159$, and $n_s = 0.9667$. The TNG simulation consists of three volumes and 18 simulations in total. In this work we use TNG100-1 ("TNG100" hereafter), which are the second largest simulated boxes and with the highest resolution available on the database. TNG100 spans a side length of 75 h^{-1} Mpc and includes periodic boundary conditions. In the TNG100 simulation, the evolution of an initial set of $N_p = 1820^3$ gas cells, each with a mass of $9.4 \times 10^5 h^{-1} M_\odot$ is tracked, along with dark matter particles of mass $5.1 \times 10^6 h^{-1} M_\odot$.

TNG simulations are a proven tool for studies of the connection between halos and galaxies and have provided important insights for several scientific cases in the field of large-scale structure and cosmology (see, e.g., few examples in Bose et al., 2019; Contreras et al., 2021; Engler et al., 2021; Favole et al., 2022; Hadzhiyska et al., 2021, 2020; Martizzi et al., 2019, 2020; Montero-Dorta et al., 2021a, 2020, 2021b; Montero-Dorta and Rodriguez, 2024; Montero-Dorta et al., 2024; Pillepich et al., 2018; Shi et al., 2020; Springel et al., 2018), proving they are a suitable tool for the goal of this work. In the next section we describe the set of properties used.

Figure 1 shows the matter distribution at three different redshifts. At $z = 0$ a large difference between the areas with higher and lower density compared to the images of the other (higher) redshifts. We can also see that the amount of voids has increased significantly and that almost all dark matter particles are clustered in areas with a higher density.

2.2. Halo and subhalo populations

We have used the TNG100 galaxy and dark matter catalogues available on the database. The dark-matter halos (called "groups" in TNG) are derived with a standard friends-of-friends (FOF) algorithm with linking length of 0.2 times the mean inter-particle separation (Davis et al., 1985). This algorithm is run on the dark matter particles and the other types (gas, stars, BHs) are attached to the same groups as their nearest DM particle. On the other hand, the SUBFIND algorithm (Springel et al., 2001 ; Dolag et al., 2009) is used to identify subhalos (called "subhalos" in TNG). Galaxies in this context are defined as subhalos containing a non-zero stellar mass component. Therefore, we will treat the subhalos and the galaxies interchangeably

As mentioned in §1.4, the halo mass function is one of the basic tools in modern cosmology to quantify the abundances. Understanding the structure and formation of dark matter halos plays a pivotal role in the understanding of formation and evolution of galaxies since dark matter halos are the hosts of galaxies. Figure 2 shows the halo mass function from the TNG100 at the three redshifts analyzed throughout the work: $z = 0$, $z = 1$ and $z = 3$ (with Poisson error bars, $\sigma(M) = n(M)/\sqrt{N}$ where N denotes the number of halos in each mass bin). The shape of the mass function is a consequence of merging history of dark matter halos. In the ΛCDM model, structure formation occurs in a hierarchical *bottom-up* way, meaning that smaller halos develop earlier and subsequently merge into larger and larger halos. The rate of mergers decreases as the halo mass increases and thus more massive halos are less common (Mo et al., 2010). This figure also shows the predictions from fits to N-body simulations by Tinker et al. (2008) and Watson et al. (2013). The differences observed between measurements and predictions are expected as the latter are obtained from pure dark matter simulations, with different definitions of halo masses and in dynamical ranges different o the ones presented here. Nevertheless, they show good agreement with the abundance of seen in the TNG.

Along with the halo mass, in this work we have analyzed the following set of properties:

- $V_{\max}$ [km / s]: Maximum value of the spherically-averaged rotation curve of the subhalo. This corresponds to the "subhaloVmax" TNG100 property.

- σ_v [km / s]: One-dimensional velocity dispersion of all the member particles/cells of the subhalo (note that is the 3D dispersion divided by $\sqrt{3}$. This corresponds to the "subhaloVelDisp" TNG100 property.

- Spin [(Mpc / h)(km / s)]: Total spin, computed as mass weighted sum of the relative coordinate times relative velocity of all particles/cells of the subhalo. This corresponds to the norm of the "subhalospin" TNG100 property, because this property shows us the total spin per axis. Actually this parameter is the specific angular momentum of the subhalo, therefore during the work we will call it indistinctly as j or as spin.

- Metallicity: Mass-weighted average metallicity (M_z/M_{tot}, where M_z refers to the mass in the form of any element heavier than Helium) of the gas cells bound to the subhalo, but restricted to cells which are star forming. This corresponds to the "subhaloGasMetallicitySfr" TNG100 property.
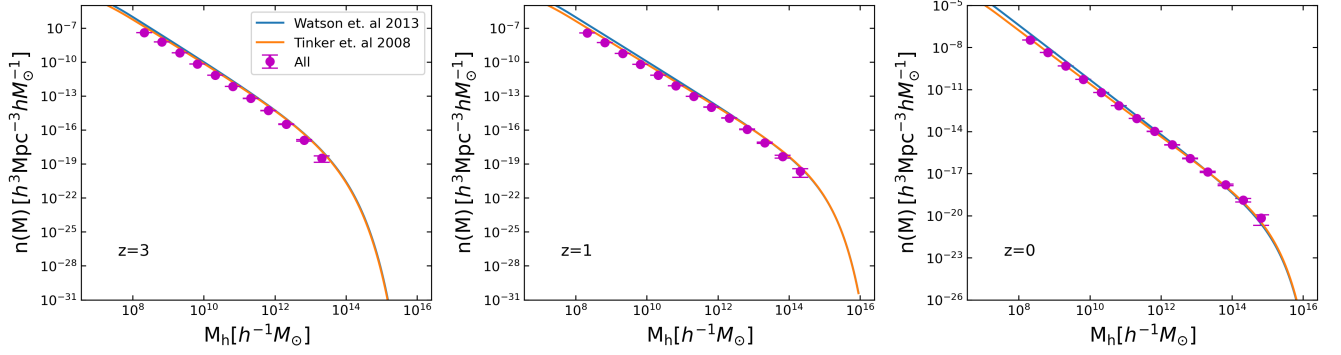
Figure 2: Binned halo mass function of TNG100 haloes at the redshifts analyzed throughout the work, from left to right $z = 3$, $z = 1$ and $z = 0$. The error bars are Poisson's bars. The blue line is the fit for the mass function by Watson et al. (2013) and the orange line is the fit by Tinker et al. (2008), both computed using the `CosmiCCodes` library (Balaguera-Antolinez, A, 2024).

In Fig. 3 we show the distribution of the properties presented in this section at redshifts $z = 3$ and $z = 0$. According to Eq. (17), these distributions are described by mass functions (showed in Fig. 2) and scaling relations that we will measure in the next section. In this figure we see that the $V_{\max}$, σ_v and spin have a very similar shape. We would then expect that the scaling relations would also be very similar. The metallicity distribution is different from that of the other three distributions, so we can expect that its link to the halo mass has a different dependency.

3. Scaling relations of dark matter halos

In this section we will assess the scaling relations between some of the main properties of halos and subhalos in the TNG100 simulation. We will describe the statistical properties at a number of orders and present the theoretical expectations and the measurements made in this work. Finally we will define the dependencies on the environment and show the dependence of the scaling relations on the mass of the halos.

3.1. Theoretical framework and predictions

The current study has been performed by separating the scaling-relations into two groups, namely:

1. **First-order scaling relations** are those relationships concerning the properties of subhalos.

2. **Second-order scale relations** are those that correlate the various properties of subhalos, with the properties of their host halos, mainly with the halo mass.

In general, these two scaling relations are linked by the scaling relation between M_s and M_h, as

$$P(\theta|M_h) = \int_{-\infty}^{\infty} P(\theta|M_s)P(M_s|M_h)\mathrm{d}M_s, \tag{18}$$

where θ are the subhalo properties explained before, M_h is the halo mass and M_s is the subhalo mass.
In Fig. 4 we shown an example of the scaling relation $P(V_{\max}|M_s)$ in a given bin if subhalo mass (at $z = 3$). The plot compares the actual distribution form the TNG and a normal distribution computed using the measured mean and variances, showing how the current distribution. In general, the mean value of the property θ with respect to M_h is

$$\langle\theta|M_h\rangle = \int_{-\infty}^{\infty} P(M_s|M_h)\langle\theta|M_s\rangle\mathrm{d}M_s, \tag{19}$$

where $\langle\theta|M_s\rangle$ denotes the mean value of the property θ as a function of the subhalo mass. As a toy model, let us assume that the $M_s - M_h$ relation has no scatter. For this, let us assume that this ratio is a Dirac delta, centered on the mean $\langle M_s|M_h\rangle$ so that the scaling ratio is $P(M_s|M_h) = \delta_D(M_s - \langle M_s|M_h\rangle)$. Hence $\langle\theta|M_h\rangle = \langle\theta|\tilde{M}_s(M_h)\rangle$, where $\tilde{M}_s = \langle M_s|M_h\rangle$. If we assume that the the mean of the $M_s - M_h$ and the $\theta - M_s$ follow a power-law ($\langle M_s|M_h\rangle = AM_h^\alpha$ and $\langle\theta|M_s\rangle = BM_s^\beta$), then, $\langle\theta|M_h\rangle \propto M_h^{\alpha+\beta}$ is also a power-law.
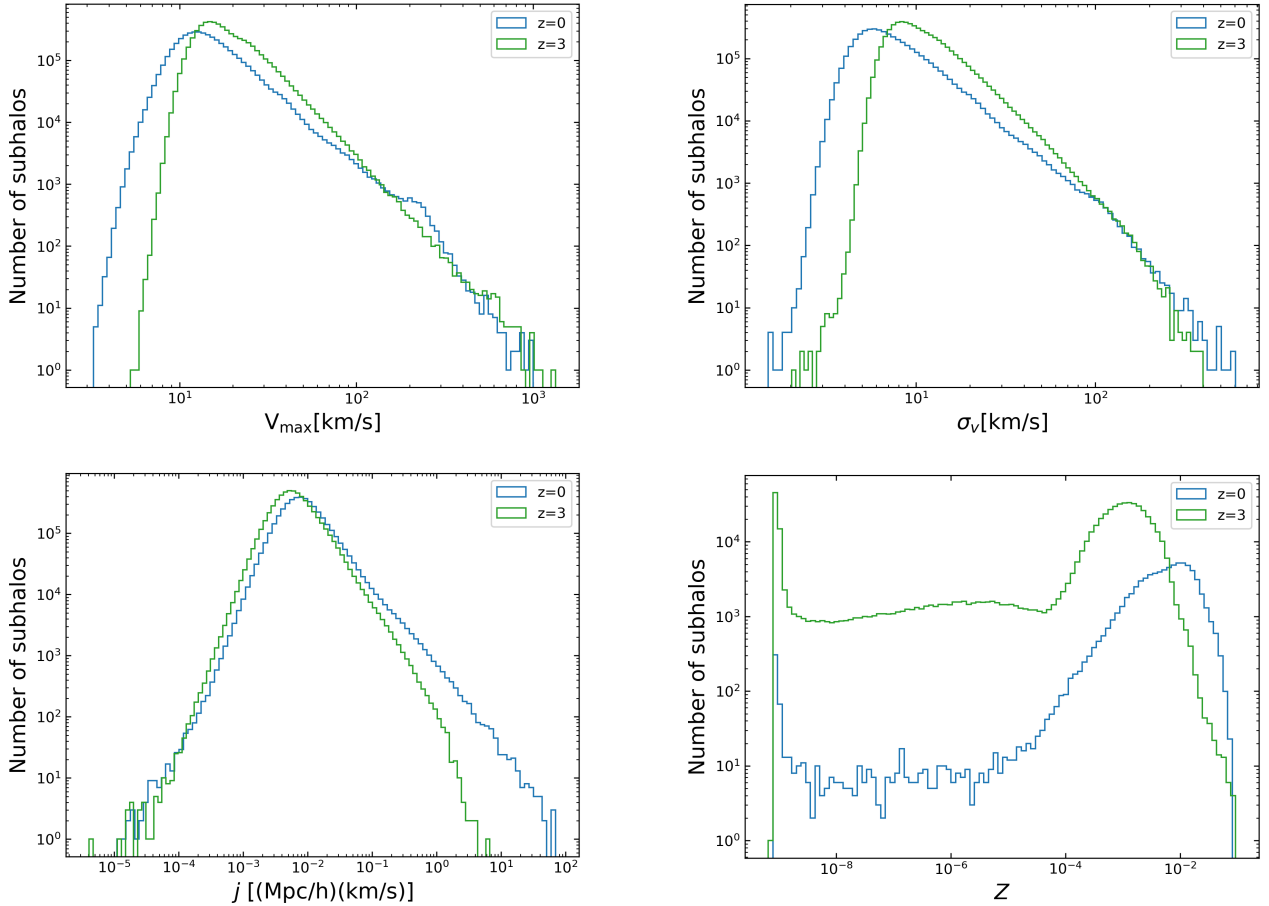
Figure 3: Distribution of the TNG100 subhalo properties at $z = 3$ (in green) and $z = 0$ (in blue). The properties analyzed are: in the upper row, from left to right, $V_{\max}$ and σ_v, respectively and, in the lower row, from left to right, j and Z, respectively

From the virial theorem we can forecast the shape of the $M - V_{\max}$ scaling-relation. Writing the kinetic energy (associated to internal motions) of a halo as $K \propto MV_{max}^2$, and the gravitational potential energy as $W \propto M^2R^{-1}$, the virial theorem yields $V_{max}^2 \propto MR^{-1}$. The typical size R of the halo is related to the mass as $R \propto M^{1/3}$, such that $V_{max} \propto M^{1/3}$. The velocity dispersion σ scales in the same way as $V_{\max}$, i.e. $\sigma \propto M^{1/3}$ (see e.g., Mo et al., 2010; Peebles, 1993).

Using the same arguments, we can derive the $M-$spin relation using some approximations. From the definition showed in §2.2, the total spin for subhalos is calculated as

$$ j = \frac{1}{M} \int \mathrm{d}^3r\rho(\mathbf{x})(\mathbf{r} \times \mathbf{v}) = \frac{4\pi}{V} \int_0^R \mathrm{d}r r^3 \sqrt{M/r} \propto M^{1/2}R^{1/2} \propto M^{2/3}. $$

where the last scaling-law is obtained assuming circular orbits and constant density.

The scaling relation between metallicity and mass can not be derived from the virial theorem since it comes from the Boltzmann equation and the latter does not take into account star formation, which explains how metals are produced. Metals are synthesized in stars and then ejected into the interstellar medium (ISM) by stellar winds and supernovae (Tutukov et al., 2000). The metal-enriched ISM acts as the raw material for next-generation stars. This metal content in the ISM can be altered by the inflow of gas from the intergalactic medium or by the outflow of gas due to stellar winds and supernovae. Thus, the metallicity in star-forming galaxies will depend on the star formation and gas outflows (Zahid et al., 2014). Lequeux et al. (1979) saw that the gas-phase metallicity of star-forming galaxies scales with the stellar mass in the so-called mass-metallicity (MZ) relation. This MZ relation is a power law that flattens or saturates at large stellar masses (see e.g., Tremonti et al., 2004 ; Zahid et al., 2013 ; Zahid et al., 2017). The point where metallicity saturates occurs when the mass of metals produced and returned to the ISM equals the mass of metals trapped in the low-mass stars (Zahid et al., 2014).
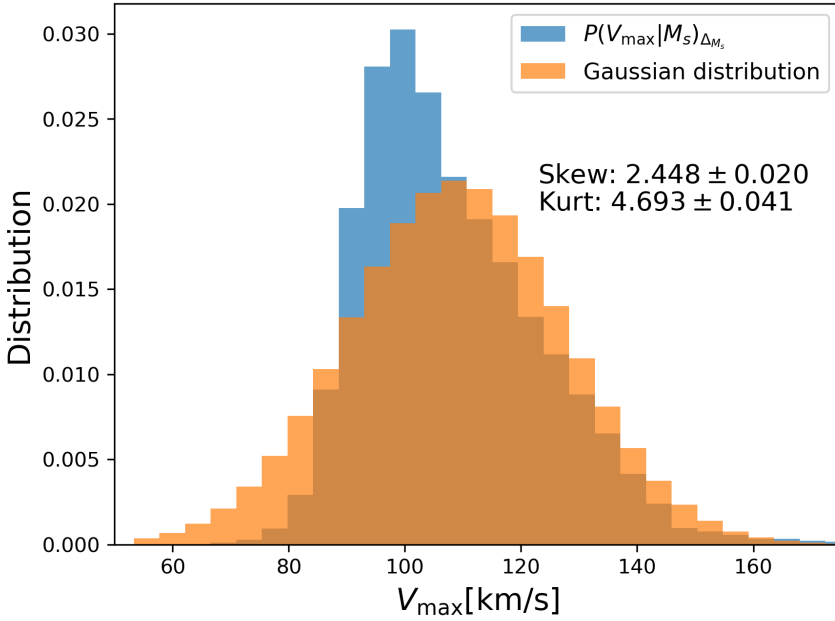
Figure 4: Comparison between the distribution of the $V_{\max}$ within the $M \sim 10^{10-10.5}h^{-1}M_\odot$ bin at $z = 3$ and the Gaussian distribution defined with the same mean and variance.

3.2. First-order scaling relations

In this section we show the most general first-order scaling relations in the simulation and the skewness and kurtosis of the CDF's that are defined within each mass bin. To that aim, the whole mass range of the subhalos has been divided into $10^{0.5}$ $h^{-1}M_\odot$ intervals. And from here obtain the distribution and its higher-order moments for each property (see Appendix A). Figure 5 shows the first-order scaling relations of the subhalo properties presented in §2.2. In Tab. 1 we show the slopes and the correlation between the subhalo properties with respect to the subhalo mass.

The trend of $V_{\max}$, i.e. the top-left of Fig. 5, shows almost the same slope at the three redshifts, as shown in Tab. 1. These slopes are very similar to the theoretical value $(1/3)$ while the amplitude decreases with decreasing redshift. We have also computed the Pearson correlation coefficient (see Appendix A), which for this case decreases with decreasing redshift, which means that for fixed subhalo masses the $V_{\max}$ tends to display a larger scatter. In overall, this behavior can be linked to the fact that sub-structures are subject to stronger tidal interactions as long as redshift decreases. Such tidal interactions can arise from the internal distribution of sub-structures in the parent halos, as well as coupling with the external tidal field where the latter reside. The top-right panel of Fig. 5, shows the first-order $M_s - \sigma_v$ scaling relation. As expected from the behavior of maximum circular velocity (these two are probes of the depth of the potential well) the amplitude increases with redshift, while from Tab. 1 we read that the slopes are in good agreement with theoretical expectations (i.e., $1/3$). Similarly the correlation decreases as long as redshift decreases.

The subhalo mass-spin scaling relation for the (bottom-left panel in Fig. 5) shows us that unlike two properties shown above, the differences in the amplitudes are only noticeable for high-mass subhalos. One evident difference arises from the presence of high mass halos at lower redshift, but in general, at $M_s \sim 10^{13}h^{-1}M_\odot$ the spin increases as long as redshift decreases. This can also be explained by tidal interactions, since at lower redshift, subhalos experience more frequent and stronger tidal interactions due to the high density where these structures reside. This increase the angular momentum of subhaloes, especially in high-mass subhaloes (see e.g., Porciani et al., 2002). The ratio of spin to subhalo mass is very similar to the theoretical value shown in §3.1 (i.e., $2/3$). We do not observe large changes in correlation from one redshift to another.

Finally, the mass-metallicity $(M - Z)$ relation (bottom-right of Fig. 5) shows a very rapid increase in value (2-3 orders of magnitude) for masses between $10^8 - 10^{12}h^{-1}M_\odot$ and a subsequent saturation. This trend can be modeled by two power-laws, the first displaying a positive slope and the second showing saturation. The values of these two slopes are shown in the Tab. 1. This is consistent with the trends explained in § 3.1, i.e., the $M - Z$ relation is a power law that flattens at large stellar masses. The correlation also show two different values: for subhalos with $M_s > 10^{12}h^{-1}M_\odot$, metallicity and mass weakly correlated, with $\rho \sim 0$ while for lower masses there is somewhat more correlation between subhalo mass and metallicity ~ 0.5. Note that the value of the metallicity at the first mass bin (i.e., $M_s \lesssim 10^{7.5}h^{-1}M_\odot$) tend to 0. We omit that bin for the calculation of the skewness and kurtosis.

In Fig. 6 we present the skewness and kurtosis of the CDF's as a function of subhalo mass for the four properties $\theta =$
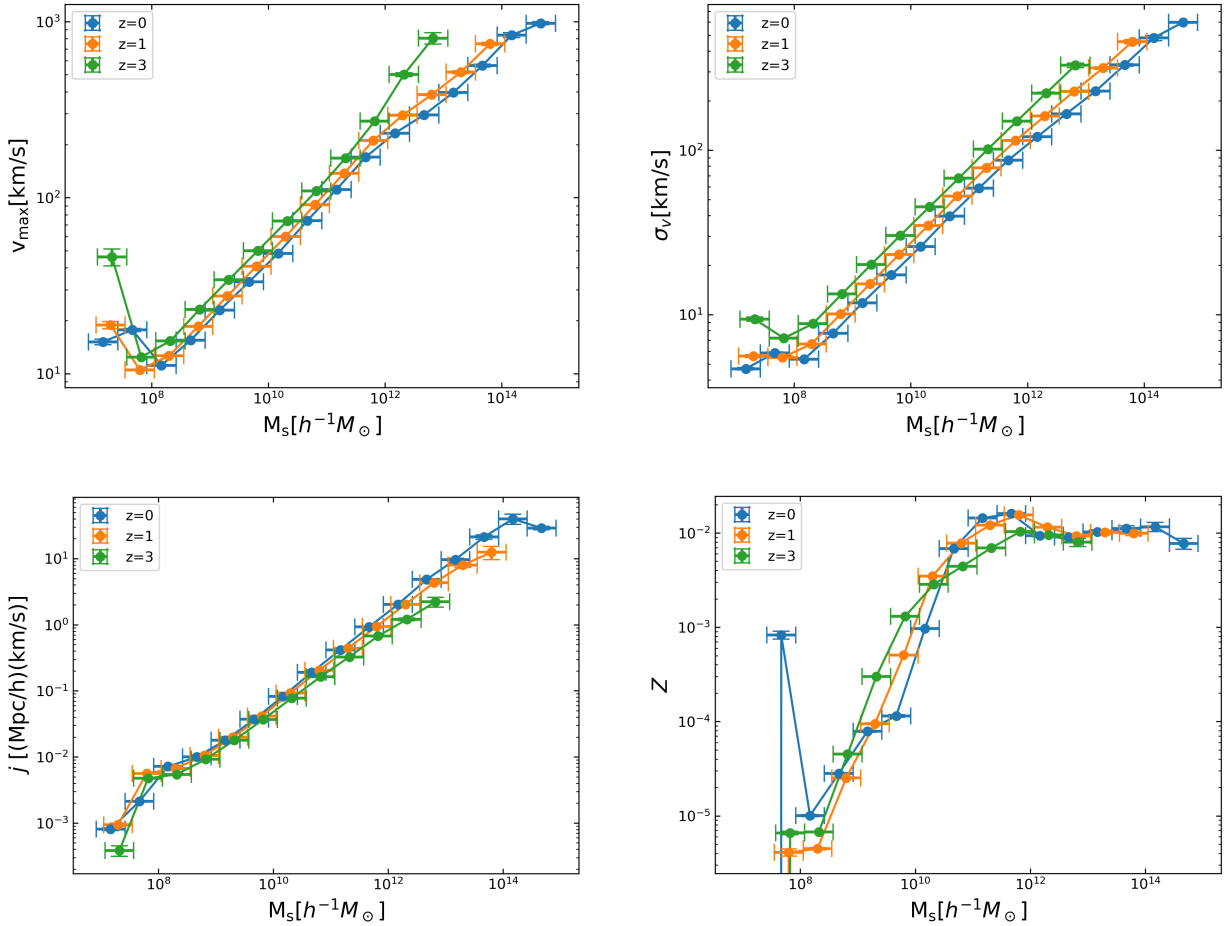
Figure 5: First-order scaling relations of the TNG100 subhalo properties (i.e., with respect to M_s) at three different redshifts: $z = 3$ (in green), $z = 1$ (in orange) and $z = 0$ (in blue). The properties analyzed are: in the upper row, from left to right, $V_{\max}$ and σ_v, respectively and, in the lower row, from left to right, j and Z, respectively

$\{V_{\max}, \sigma_v, j, Z\}$) under analysis. The skewness of the scaling relations $P(\theta|M_s)$ is positive for masses up to $\sim 10^{12} M_\odot\, h^{-1}$. Therefore, we conclude that at all mass scales (except for the very high mass bins), the scaling relation $P(\theta|M_s)$ is not compatible with a Gaussian distribution.

The CDF of the properties defined at the lowest mass-bin at $z = 1$ and $z = 0$ and the two lowest mass-bins at $z = 3$ have a negative kurtosis, meaning that they have flat peaks. The CDF's of the properties of the subhalos that have masses between $10^8 - 10^{11} h^{-1} M_\odot$ have, in general, a positive kurtosis. At high masses, the properties of subhalos have a flatten distribution again. Finally, the distributions that can be compatible with the normal distribution (within the error bars are): the last two mass bins of $z = 0$ and the last mass bin of both $z = 1$ and $z = 3$, for all properties (except j at $z = 3$).

3.3.   Second-order scaling relations

For the second-order scaling relations we have proceeded in an analogous way but this time the range of the halos has been divided into bins of halo mass. As explained in §3.1, the first and second order scaling relations are related through the scaling relation between the subhalo mass and the halo mass (see Eq. 18).

To properly understand some of the results, we analyze in first place how galaxies (subhalos) are distributed in the haloes according to their mass. To this aim, we measure a *halo occupation distribution* (HOD hereafter), which assess the average number of subhalos being hosted by halos of a given mass.

As shown in Eq. (18), we know that the second-order scaling relations can be derived from the convolution between the distribution of a θ property conditional on mass with a mass function. To this aim, in Fig. 7 we provide the distribution of the subhalos within the halos and the scaling relation between them. The top left plot shows that this scaling relation has two clear tendencies. The first occurs at low masses (the first three bins of halo mass, i.e. $M_h \leq 10^{10} h^{-1} M_\odot$) where the subhalo mass evolves very rapidly and the slopes shown in Tab. 2. From the top right plot we can say that in this low mass range the HOD

z=3		Slope	Correlation coefficient
$v_{\max}$		0.30 ± 0.03	0.533
σ_v		0.32 ± 0.02	0.480
j		0.62 ± 0.03	0.695
Z	$M < 10^{12}h^{-1}M_\odot$	0.88 ± 0.10	0.524
	$M > 10^{12}h^{-1}M_\odot$	0.03 ± 0.01	-0.187
z=1		Slope	Correlation coefficient
$v_{\max}$		0.30 ± 0.02	0.339
σ_v		0.32 ± 0.01	0.347
j		0.62 ± 0.02	0.688
Z	$M < 10^{12}h^{-1}M_\odot$	1.06 ± 0.10	0.555
	$M > 10^{12}h^{-1}M_\odot$	-0.06 ± 0.02	-0.082
z=0		Slope	Correlation coefficient
$v_{\max}$		0.28 ± 0.01	0.259
σ_v		0.30 ± 0.01	0.280
j		0.64 ± 0.01	0.701
Z	$M_s < 10^{12}h^{-1}M_\odot$	1.02 ± 0.08	0.509
	$M_s > 10^{12}h^{-1}M_\odot$	-0.05 ± 0.03	0.051

Table 1: Slopes and correlation coefficients of the first-order scaling relations for subhalos (i.e., with respect to M_s). From top to bottom: $V_{\max}, \sigma_v, j$ and Z, shown in Fig. 5. The Z trends are divided between subhalos with $M_s < 10^{12}h^{-1}M_\odot$ and those with $M_s > 10^{12}h^{-1}M_\odot$. From top to bottom are shown the 3 redshifts analyzed in this work, $z = 3$, $z = 1$ and $z = 0$ respectively. The slope and its error are obtained from a linear regression made in GNUPLOT.

		Slope			Correlation coefficient		
		z=3	z=1	z=0	z=3	z=1	z=0
	Low-mass	0.77 ± 0.01	0.80 ± 0.02	0.85 ± 0.02	0.670	0.727	0.790
M_s	Mid-mass	0.30 ± 0.02	0.30 ± 0.03	0.30 ± 0.04	0.080	0.077	0.078
	High-mass	0.08 ± 0.01	0.05 ± 0.02	0.03 ± 0.01	0.005	0.003	0.001
	Low-mass	0.29 ± 0.02	0.30 ± 0.03	0.28 ± 0.05	0.523	0.475	0.440
HOD	Mid-mass	0.71 ± 0.02	0.71 ± 0.03	0.72 ± 0.04	0.891	0.894	0.889
	High-mass	0.79 ± 0.04	0.87 ± 0.03	0.93 ± 0.02	0.95	0.989	0.994

Table 2: Slopes and correlation coefficients of the second-order scaling relations of the subhalo mass and the HOD (i.e., as a function of M_h), shown in Fig. 7. Note that three trends are shown which are called: *Low-mass* to the halos with $M_h < 10^{10}h^{-1}M_\odot$, *Mid-mass* to those with masses between $10^{10}h^{-1}M_\odot - 10^{12}h^{-1}M_\odot$ and *High-mass* to those with $M_h > 10^{12}h^{-1}M_\odot$. Three redshifts are shown, from left to right $z = 3$, $z = 1$ and $z = 0$.
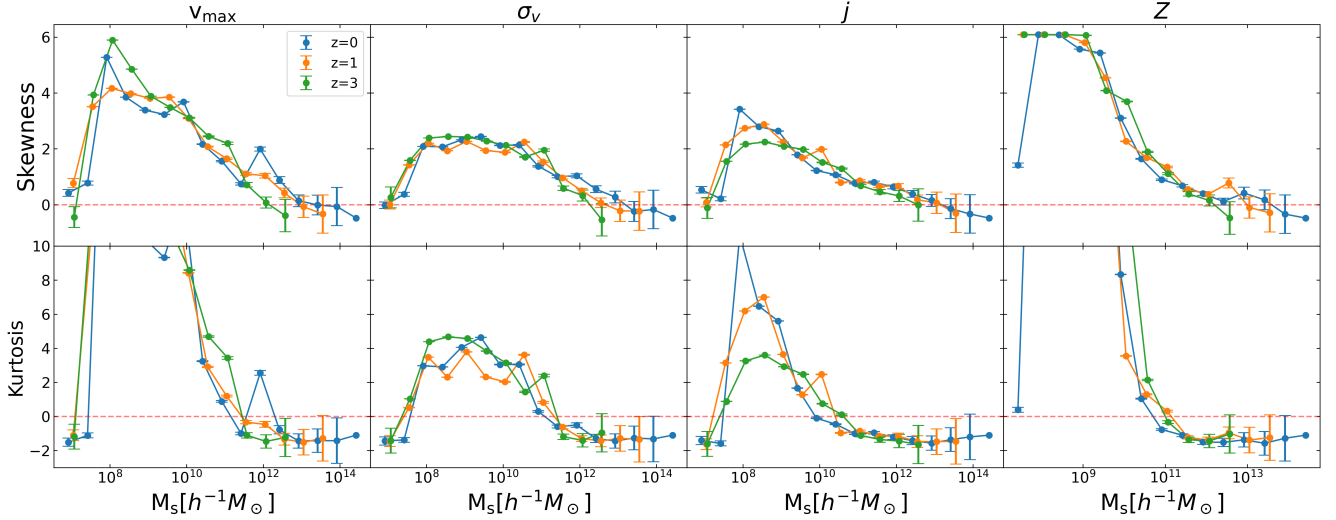
Figure 6: Evolution of the skewness and kurtosis of the CDF of the subhalo properties at the TNG100 simulation defined within each subhalo mass bin, due to the fact we are analyzing the first-order scaling relations, at three different redshifts: $z = 3$ (in green), $z = 1$ (in orange) and $z = 0$ (in blue). The properties analyzed are, from left to right, the V_{max}, σ_v, j and Z, respectively. The dashed red line at the 0 value on the horizontal axis represents the value at which the skewness and kurtosis take the same value that a Gaussian distribution would take.

gives us approximately 1. With this, most of the halos in these masses have no substructures beyond the individual subhalos in each halo. This is confirmed with the value of the correlation which is high, meaning that the scatter of the subhalo masses with respect to the mean values is low. Furthermore, from the two lower plots in Fig. 7, we can deduce that the distribution of subhalos in low-mass halos tends to be centered or slightly shifted at low values in mass (the skewness value is $\gtrsim 0$) but with smoother values at the peak than a Gaussian distribution would show (the kurtosis value is < 0).

The link between the mass of the subhalos and the mass of the halos with in halo masses called *Mid-mass*, show a trend that has a lower mass dependence than shown above, since the scaling ratio decreases (see Tab. 2). This, coupled with the very low value of the correlation coefficient ($\rho \sim 0.08$), indicates that subhalos with a wide mass range can live in these halos, which is confirmed by the HOD trend that shows that the higher the mass of the halo, the more substructures it will have. In addition, the upward trend of skewness of the subhalo masses with respect to halo mass indicates that most subhalos in this mass range will be of low mass. This can be explained by the accumulation of substructures. Mid-mass halos may have accumulated subhalos of different masses throughout their formation history, contributing to a more skewed distribution of subhalo masses.

Finally, at the high-mass end ($M_h \geq 10^{12} h^{-1} M_\odot$), the ratio between the mass of the subhalos and the mass of the halos remains relatively constant, as shown in Tab. 2. Despite this, the average number of subhalos in each halo is very large ($\sim 10^3 - 10^4$) at the last halo mass bin. This, together with the very high skewness and kurtosis values, suggests that the most massive halos host a number of low-mass subhalos much larger than the high-mass subhalos.

With the information in Fig. 7, we can say that the assumption that the scaling relationship between M_s and M_h follows a power law has to be modified. For this purpose, following Balaguera-Antolinez et al. (2012) we adopt a mass-dependent slope to parameterize the mean of the scaling relation $M_s - M_h$. Defining $m_s \equiv \log_{10}(M_s)$ and $m_h \equiv \log_{10}(M_h)$, our model of the mean scaling relation $M_s - M_h$ has the form of a quadratic function

$$m_s(m_h) = a + bm_h + cm_h^2. \tag{20}$$

where a is the amplitude, b is the slope and c is the curvature of the function. Some works have already analyzed this relation. Shankar et al. (2006), for example, analyzed the scaling relation between halo mass and several galaxy properties (including the stellar mass, among others) concluding that all the scaling relations shown are well represented by a double power law with a break in $M_{h,break} \sim 3 \times 10^{11} M_\odot$, in agreement with Fig. 7.

We now compute the second-order scaling relations for the other properties analyzed in this work which is shown in Fig. 9. As mentioned at the beginning of this section, the first- and second-order scaling relations are related by the scaling relation between the subhalo mass with respect to the halo mass. Figure 9 show that the second-order scaling relations have a maximum in all the properties when $M_h = 10^{10.5-11} h^{-1} M_\odot$. Up to that mass, the trend of the second-order scaling relations has a trend
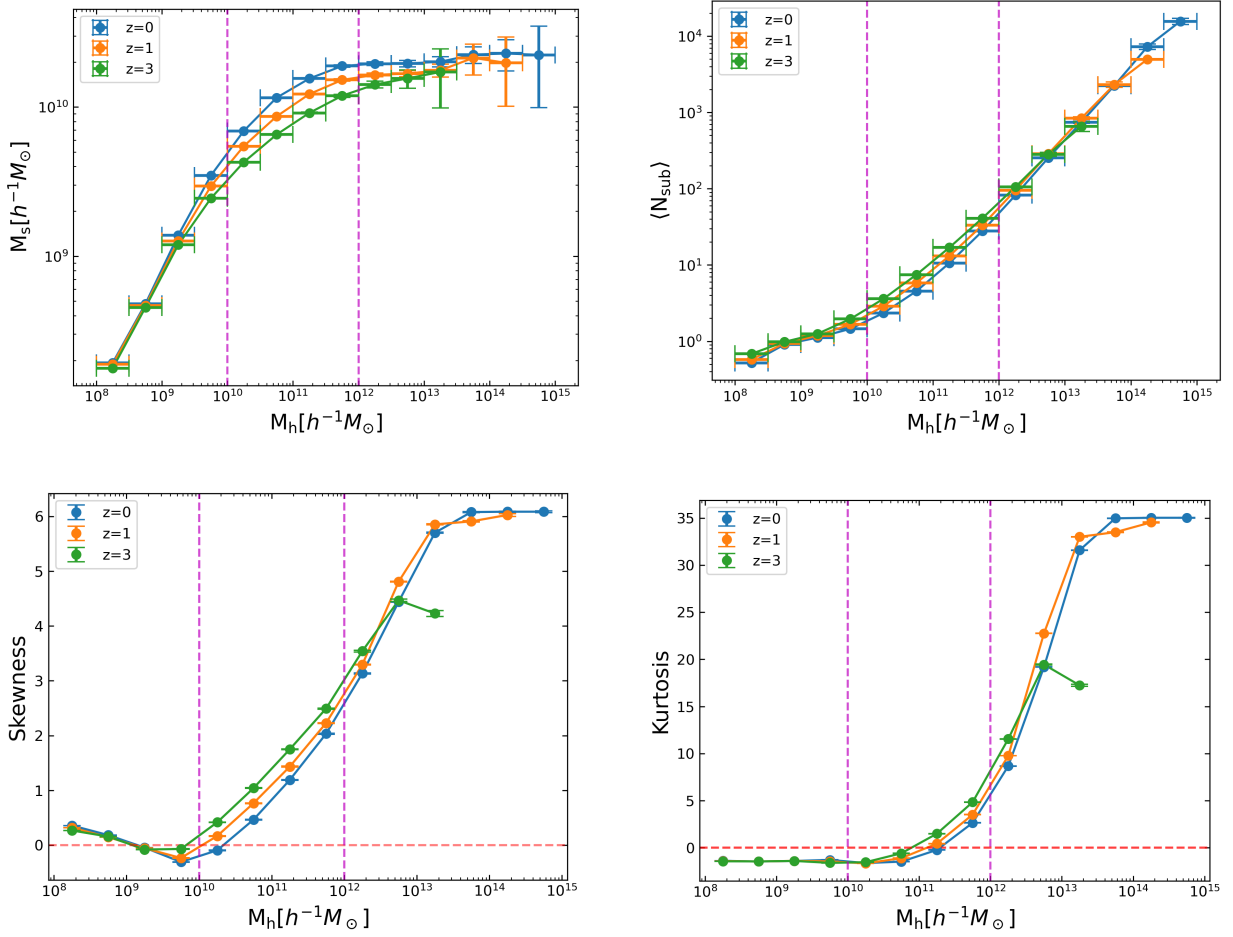
Figure 7: Top left: Scaling relation of M_s with respect to M_h. Top right: Halo occupation distribution. Bottom left: Skewness of the second-order scaling relation of M_s. Bottom right: Kurtosis of the second-order scaling relation of M_s. All this four plots are computed at the TNG100 simulation at three different redshifts: $z = 3$ (in green), $z = 1$ (in orange) and $z = 0$ (in blue). Dashed vertical lines separate the plot into *low-mass* halos, *mid-mass* halos and *high-mass* halos.
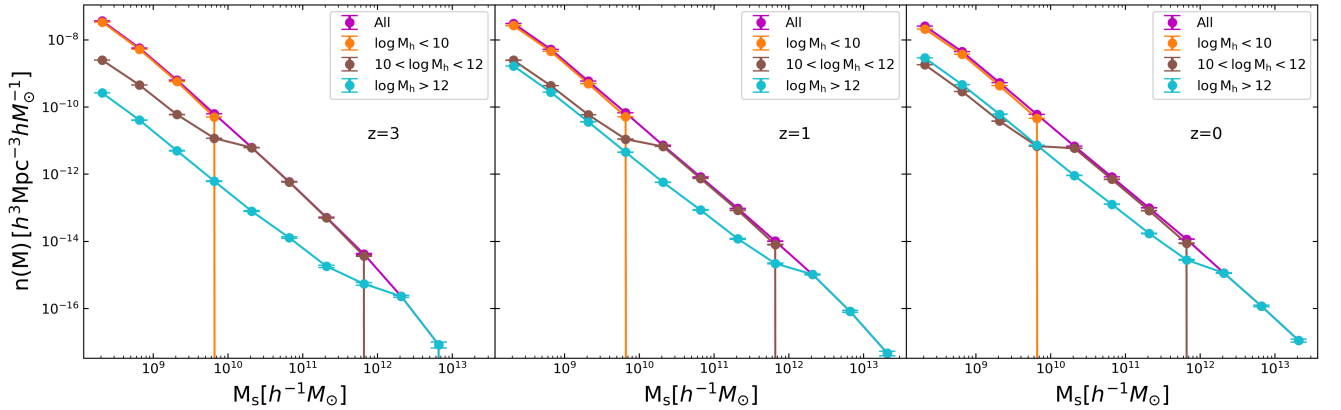

Figure 8: Binned subhalo mass function of the TNG100 simulation for those subhalos living in three halo mass bins: halos with $M_h \leq 10^{10} h^{-1} M_\odot$ (in orange), halos with masses between $10^{10} h^{-1} M_\odot - 10^{12} h^{-1} M_\odot$ (in brown) and halos with $M_h > 10^{12} h^{-1} M_\odot$ (in blue). From left to right, three different redshifts: $z = 3$, $z = 1$ and $z = 0$, respectively. The error bars are Poisson's bars. The labeled as *All* gives us the total subhalo mass function.

similar to that of the first-order scaling relations seen in Fig. 5. We know that the mean scaling-relation of the $M_s - M_h$ is that which follows the model presented in Eq. (20), and that the mean scaling relation of θ follow a power law (see §3.2), defined as $\tilde{\theta} = d + em_s$, where $\tilde{\theta} = \log_{10}(\theta)$. Qualitatively, and using Eq. (19), we know that the function of the second-order mean-scaling relation of $\tilde{\theta}$ is
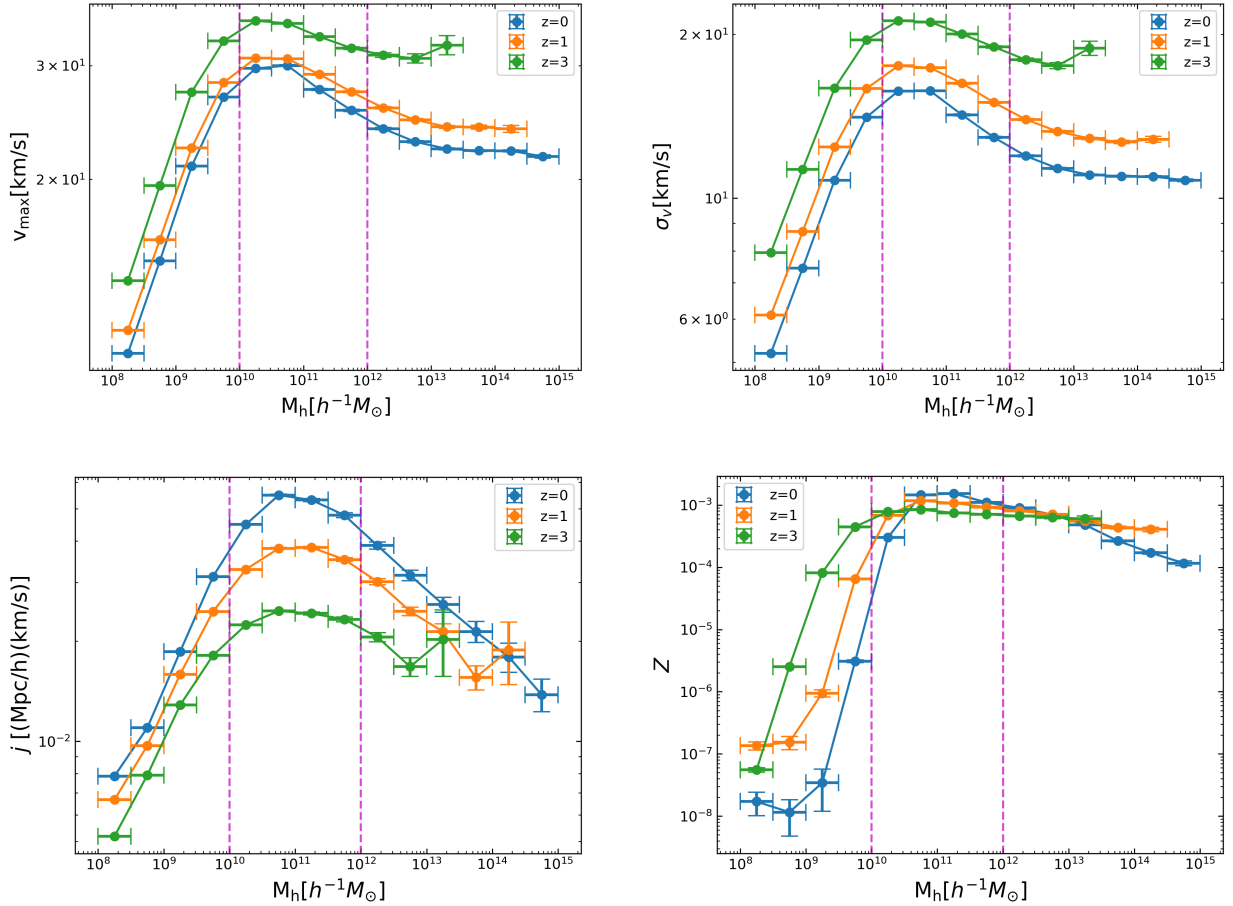
Figure 9: Second-order scaling relations of the subhalo properties (i.e., with respect to M_h) at the TNG100 simulation at three different redshifts: $z = 3$ (in green), $z = 1$ (in orange) and $z = 0$ (in blue). The properties analyzed are: in the upper row, from left to right, the $V_{\max}$ and σ_v, respectively and, in the lower row, from left to right, j and Z, respectively. Dashed vertical lines separate the plot into *low-mass* halos, *mid-mass* halos and *high-mass* halos, as in Fig. 7.

$$\tilde{\theta}(m_h) = d + e\left[a + bm_h + cm_h^2\right] = a' + b'm_h + c'm_h^2, \tag{21}$$

where $a' = d + ea$, $b' = e * b$ and $c' = ec$. This as a critical point at $m_h = -b'/(2c')$, which is a maximum if $c' < 0$. We have fitted the parameters of Eq. (20) using a least squares fit[3] for each redshift and the best fit values are: $a = -5.14 \pm 0.58$, $b = 2.40 \pm 0.11$ and $c = -0.09 \pm 0.01$ at $z = 3$, $a = -4.71 \pm 0.83$, $b = 2.31 \pm 0.15$ and $c = -0.09 \pm 0.01$ at $z = 1$, and $a = -4.70 \pm 1.01$, $b = 2.31 \pm 0.18$ and $c = -0.09 \pm 0.01$ at $z = 0$, From Tab. 1, we know that the scaling relation of $V_{\max}$, σ_v and j is defined as a positive power law, meaning that the parameter e of Eq. (21) is positive, from which we verify the conditions $c' < 0$.

Fig. 8 shows the subhalo mass function for the subhalos hosted by the halos in the three mass-ranges considered. For all halo mass ranges, the abundance of low mass subhalos is higher than that of high mass subhalos. The mean value of the relation $M_s - M_h$ saturates because the statistics of subhalos living in high-intermediate mass halos is dominated by low-mass subhalos. This saturation, causes the second-order scaling relations to have that maximum in all properties when $M_h = 10^{10.5-11}h^{-1}M_\odot$. Up to that mass, the trend of the second-order scaling relations has a trend similar to that of the first-order scaling relations seen in Fig. 5.

In Tab. 2 we have seen that at the low-mass end, $M_s - M_h$ grows in a significantly monotonic manner. This occurs because for these masses, the halos have few substructures, as seen in the HOD of Fig. 7. In Fig. 9 we see that both $V_{\max}$ and the σ_v grows with halo mass, which means that the average potential well of the subhaloes will be deeper. As the halo increases in mass, it will start to accrete more and more subhalos and will begin to have a larger substructure. At $M_h = 10^{10.5-11}h^{-1}M_\odot$, the

---

[3]Least squares fitting is a statistical method used to fit a mathematical function to a set of data by minimizing the sum of squares of the vertical differences between the observed values and those predicted by the function (see e.g., Molugaram et al., 2017)
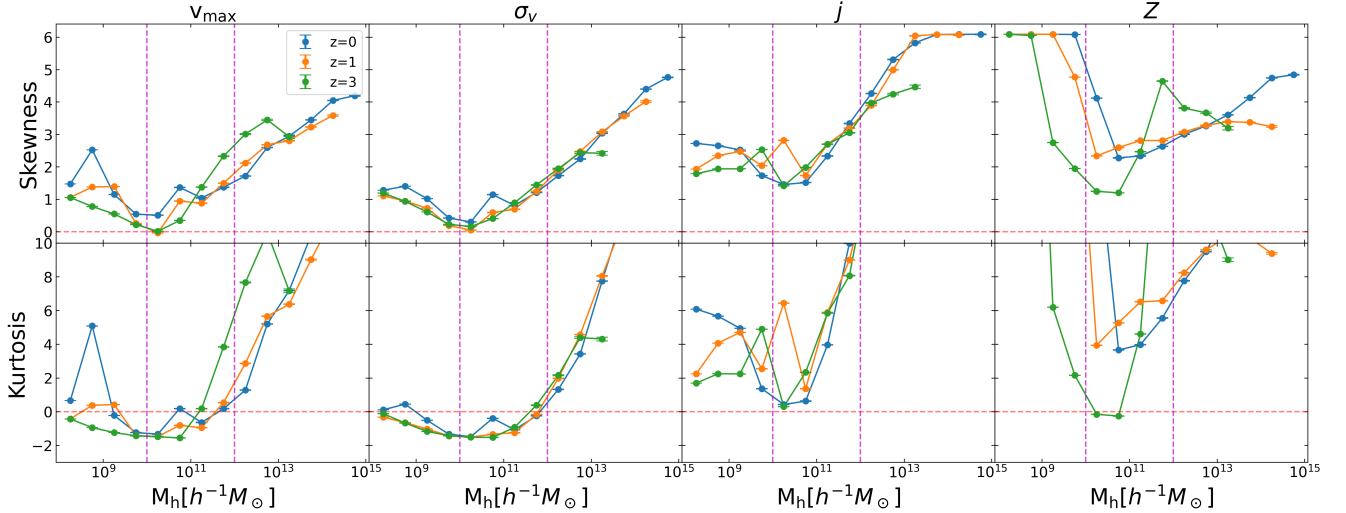
Figure 10: Evolution of the skewness and kurtosis of the CDF of the subhalo properties at the TNG100 simulation defined within each halo mass bin, due to the fact that we are analyzing the second-order scaling relations, at three different redshifts: $z = 3$ (in green), $z = 1$ (in orange) and $z = 0$ (in blue). The properties analyzed are, from left to right, the $V_{\max}$, σ_v, j and Z, respectively. The dashed red line at the 0 value on the horizontal axis represents the value at which the skewness and kurtosis take the same value that a Gaussian distribution would take. Dashed vertical lines separate the plot into *low-mass* halos, *mid-mass* halos and *high-mass* halos, as done in Fig. 7.

mean value of the relations of $V_{\max}$ and σ_v with respect to M_h stop growing. This is because low-mass subhalos, which have lower $V_{\max}$ and σ_v values, are more abundant than high-mass subhalos, causing the mean to start to drop. For halo masses greater than $\sim 10^{13} h^{-1} M_\odot$ this trend stabilizes. Consequently, we know that the mean potential well of the subhalos will tend to have a decreasing value.

The $j - M_h$ relation has a shape that after arriving the flatten mentioned above, starts decreasing. This trend does not stabilize since the difference between the j of low-mass and high-mass subhalos is relatively larger than in the previous cases, since the slope of the first-order scaling relation is higher.

We should not be surprised that the $Z - M_h$ relation does not show the same shape as the previous property relations, since the first-order scaling relation of Z can be described not by a simple but by a double power law (see Tab. 1), where the slope up to $M \sim 10^{12} h^{-1} M_\odot \sim 1$ and the slope thereafter is ~ 0. Up to $\sim M_{\mathrm{h,break}}$ the relation $Z - M_h$ is ascending and from that point it becomes constant or even a little descending. This is because the slope of the second power law of the first order scaling relation is ~ 0 so that, from Eq. (21), $\tilde{\theta}(m_h) \approx a'$. We can also notice that at high masses, the mean value of subhalo metallicity descends with redshift. This is due to the high abundance of low-mass subhalos in these halos, which tends to be higher with redshift. (see Fig. 8). As seen in the previous section, the mean metallicity of the low-mass subhalos is very small, so it will affect the mean of the second-order scale ratio, lowering it.

The correlation coefficients of Tab. 3, indicate that the properties of subhalos tent to be more correlated with the mass of the halo at low mas halos, where the trend is similar to those of first-order scale relationships. For the intermediate-high mass range, the properties of galaxies and the mass of halos tend to be uncorrelated ($\rho \sim -0.01 - 0$). We also see that as the redshift decreases, the correlation tends to be higher in the first range of masses analyzed and to be lower for the rest. In the case of metallicity, the low-mass correlation decreases when the redshift is lowered, rises for intermediate masses and falls again for high masses.

In Fig. 10 we can see the skewness and kurtosis of the distributions of the second-order scaling relations. No property at any redshift is statistically compatible with the assumption of being drawn from a Gaussian distribution within each mass bin, since for no halo mass bin the skewness and kurtosis are compatible with 0 (within error bars) at the same time. For all the properties analyzed, the skewness tends to be positive so that low values of the properties dominate the distribution. The lowest values appear at $\sim 10^{10-11} h^{-1} M_\odot$, which coincides with the value of the maximum of the function. This confirms our reasoning; from these halo masses, the statistics of the second-order scale relations of the subhalo properties are dominated by low-mass subhalos.

The distributions of $V_{\max}$ and σ_v exhibit negative kurtosis at low masses and positive kurtosis at high masses. This suggests a

		Slope			Correlation coefficient		
		z=3	z=1	z=0	z=3	z=1	z=0
$V_{\max}$	Low-mass	0.25 ± 0.02	0.26 ± 0.01	0.27 ± 0.01	0.664	0.687	0.702
	Mid-mass	-0.03 ± 0.01	-0.04 ± 0.01	-0.05 ± 0.01	-0.040	-0.054	-0.068
	High-mass	0.02 ± 0.01	-0.02 ± 0.01	-0.01 ± 0.01	0.001	-0.015	-0.015
σ_v	Low-mass	0.26 ± 0.02	0.28 ± 0.02	0.29 ± 0.01	0.677	0.708	0.733
	Mid-mass	-0.03 ± 0.01	-0.05 ± 0.01	-0.06 ± 0.01	-0.045	-0.066	-0.085
	High-mass	0.02 ± 0.02	-0.02 ± 0.01	-0.02 ± 0.01	0.000	-0.019	-0.015
j	Low-mass	0.37 ± 0.02	0.38 ± 0.01	0.41 ± 0.03	0.468	0.493	0.526
	Mid-mass	0.01 ± 0.02	$0.0.2 \pm 0.03$	0.01 ± 0.04	0.001	-0.001	-0.003
	High-mass	-0.01 ± 0.10	-0.12 ± 0.04	-0.17 ± 0.1	-0.008	-0.015	-0.014
Z	Low-mass	2.6 ± 0.3	1.8 ± 0.6	1.4 ± 0.7	0.469	0.195	0.047
	Mid-mass	-0.04 ± 0.02	0.1 ± 0.1	0.3 ± 0.3	-0.020	0.006	0.036
	High-mass	-0.05 ± 0.01	-0.16 ± 0.02	-0.37 ± 0.02	-0.011	-0.033	-0.059

Table 3: Slopes and correlation coefficients of the second-order scaling relations of the $V_{\max}$, the σ_v, the j and the Z (i.e., with respect to M_h) in three halo mass bins: *Low-mass* to the halos with $M \leq 10^{10}h^{-1}M_\odot$, *Middle-mass* $(10^{10}h^{-1}M_\odot$-$-10^{12}h^{-1}M_\odot)$ and *High-mass* $(M > 10^{12}h^{-1}M_\odot)$, as shown in Fig. 9. Three redshifts are shown, from left to right $z = 3$, $z = 1$ and $z = 0$.

tendency towards flatter distributions in the former case and more peaked distributions in the latter. j and Z consistently show higher kurtosis across all masses and redshifts, indicating a more concentrated range of values.

3.4. Environmental dependencies in scaling relations

Within the ΛCDM paradigm, galaxies are believed to form and reside in dark matter halos. The properties of galaxy populations can be thus related to the underlying density field through the properties of dark matter halo populations (Mo et al., 2010). In the following we will assess the behavior of subhalo scaling relations in different environments.

These environmental dependencies play a fundamental role in the formation and evolution of galaxies and can give us a more complete picture of the underlying physical processes. For example, the properties of galaxies will not be the same in a massive halo or in a less massive halo (as seen in §3.3). There are numerous ways to characterize the environment of a galaxy, such as the density of neighboring galaxies or the distribution of nearby galaxy types. In this work we separate these into two categories: a first one, related to the properties of the parent halo and a second one, linked to the cosmic-web environment. The mass of the haloes is presented as the first example of halo property to define an environment.

We define three ranges of parent halo masses, namely: i) *low-mass halos* $\log M_h[h^{-1}M_\odot] \leq 10$, ii) *mid-mass halos* $10 < \log M_h[h^{-1}M_\odot] \leq 12$ and finally iii) *high-mass* halos $\log M_h[h^{-1}M_\odot] > 12$. In Fig. 11 we show the first-order scaling relations for the properties expressed in the §3, i.e., velocity dispersion of the subhalos σ_v, spin of the subhalos, metallicity of the subhalos (restricted to cells which are star forming) and maximum velocity $V_{\max}$.

At $z = 3$, low-mass halos host subhalos with masses in the range $\log M_s[h^{-1}M_\odot] = 7.5 - 10$. The mid-mass halos host subhalos with masses in the range $\log M_s[h^{-1}M_\odot] = 7 - 12$ and high-mass halos host both subhalos in the lowest and the highest-mass range, i.e., $\log M_s[h^{-1}M_\odot] = 7 - 13$. The subhalo mass ranges are the same at $z = 1$, except that the low-mass halos also host subhalos in the range of $\log M_s[h^{-1}M_\odot] = 7 - 7.5$. At $z = 0$, subhalos of masses above $\log M_s[h^{-1}M_\odot] = 13$ are hosted in high-mass halos.

In Fig. 11 we show the first-order scaling relations of the subhalo properties divided according to the mass of the halo in which they live. This division is made into the three halo mass ranges specified above. The subhalos living in the less massive halos tend to have lower values of both $V_{\max}$ and σ_v at all redshifts.

The probability of having a greater number of objects increases with mass (see the second panel of Fig. 7), so there is more tidal interaction between subhalos living in the same halo. This means that in these halos, the dynamics of the dark matter particles living in each subhalo will not only be subject to the mass of the subhalo itself, but also to the tidal interaction with the other subhalos. This hypothesis is corroborated, since the correlation coefficient shown in Tab. 4 decreases as we consider higher mass halos. Moreover, as mentioned in §3.2, at $z = 3$ there are not so many tidal interactions so it makes sense that the correlation does not vary much between subhalos living in intermediate and massive halos. This causes that the potential wells
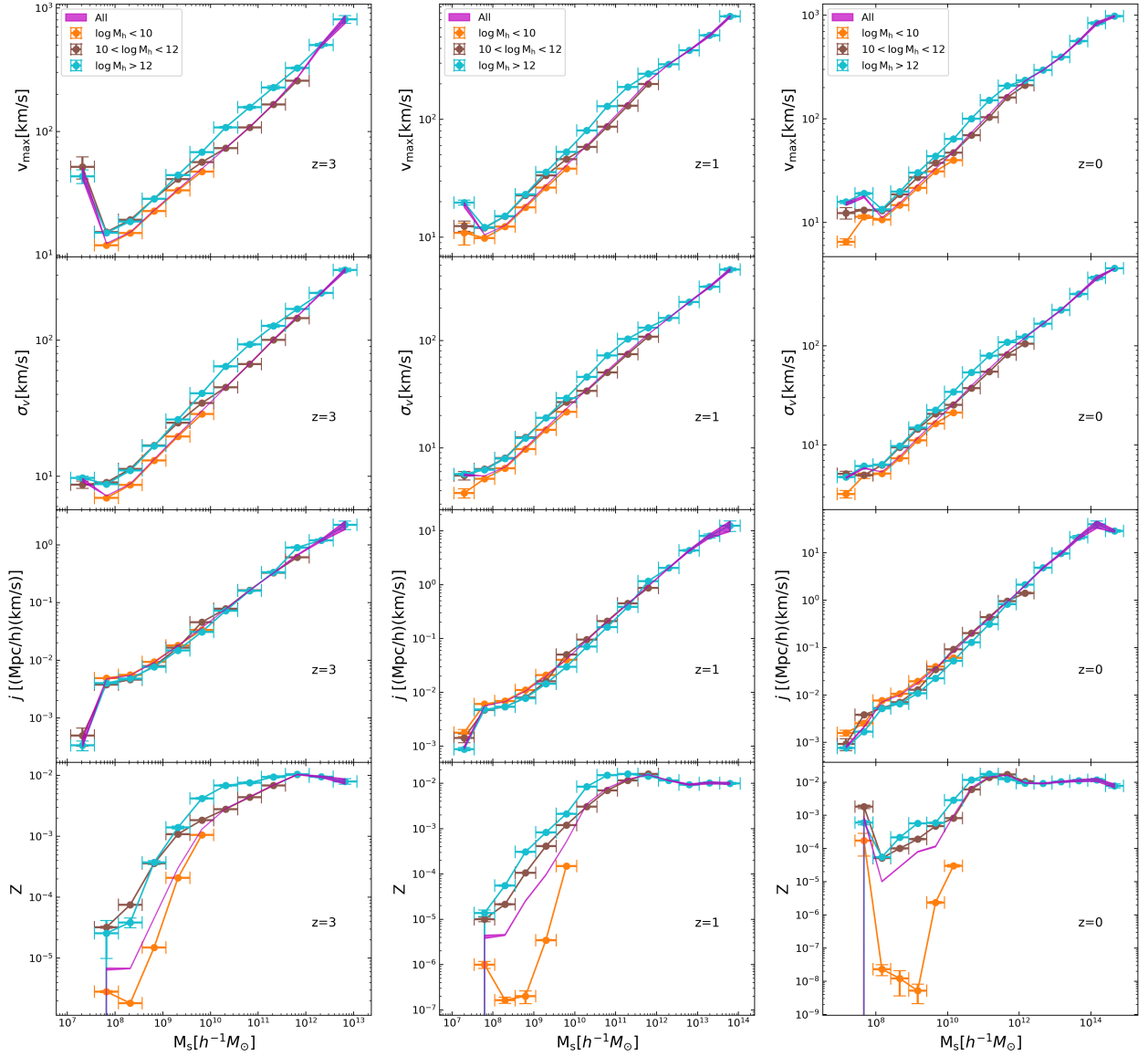
Figure 11: First-order scaling relations of the subhalo properties (i.e., with respect to M_s) at the TNG100 simulation at three different halo mass bins: $\log M_h[h^{-1}M_\odot] \leq 10$ (in orange), $10 < \log M_h[h^{-1}M_\odot] \leq 12$ (in brown) and $\log M_h[h^{-1}M_\odot] > 12$ (in blue). The properties analyzed from top to bottom are: $V_{\max}$, σ_v, j and Z, respectively and this has been done at three different redshifts, from left to right $z = 3$, $z = 1$ and $z = 0$.

of the halos of low masses are relatively small compared to those in the other mass ranges.

The third row of the Fig. 11, subhalos residing in less massive halos tend to have a higher angular momentum compared to those residing in more massive halos. One hypothesis that explains this phenomenon is based on tidal forces. In a higher mass halo, there are a greater number of substructures, resulting in more tidal interactions. These tidal forces cause the subhalos to lose their angular momentum, which is transferred to the more central subhalos or main halo. As a result, subhalos in more massive halos experience a greater decrease in angular momentum due to these interactions. The strength of the tidal forces increase as the redshift decreases, and consequently, the differences are amplified.

Subhalos in less massive halos tend to have lower metallicity because they are associated with smaller, less evolved galaxies with less star formation history. In contrast, more massive halos are found in denser regions of the universe, with metal-enriched ISM and IGM, which facilitates star formation and increases the *star formation rate* (SFR) in these subhalos (see e.g., Binney and Tremaine, 2011; Mo et al., 2010).

In Fig. 12, we can see the skewness and kurtosis of the properties of the subhalos we are analyzing for each subhalo mass bin, separated also into the three halo mass ranges in which they live, as previously done. The first two rows are at $z = 3$, the next two at $z = 1$ and the last two at $z = 0$.

		Correlation coefficient		
		z=3	z=1	z=0
$V_{\max}$	Low-mass	0.876	0.876	0.845
	Mid-mass	0.759	0.777	0.789
	High-mass	0.776	0.474	0.365
σ_v	Low-mass	0.890	0.893	0.874
	Mid-mass	0.739	0.756	0.766
	High-mass	0.730	0.511	0.403
j	Low-mass	0.698	0.687	0.679
	Mid-mass	0.792	0.819	0.825
	High-mass	0.832	0.741	0.724
Z	Low-mass	0.635	0.261	0.058
	Mid-mass	0.588	0.694	0.664
	High-mass	0.241	0.116	0.060

Table 4: Correlation coefficients of the first-order scaling relations of the $V_{\max}$, the σ_v, the j and the Z (i.e., with respect to M_s) for subhalos living in three halo mass bins: *Low-mass* to the halos with $M_h \leq 10^{10}h^{-1}M_\odot$, *Mid-mass* to those with masses between $10^{10}h^{-1}M_\odot - 10^{12}h^{-1}M_\odot$ and *High-mass* to those with $M_h > 10^{12}h^{-1}M_\odot$, shown in Fig. 11. Three redshifts are shown, from left to right $z = 3$, $z = 1$ and $z = 0$.

- From the two rows on top of Fig. 12, i.e., $z = 3$, we can observe that the tail of the CDF that represents all the properties for the mid-mass host halos is on the left of the distribution, since the skewness is positive for the whole sample (see Appendix A). On the other hand, the kurtosis for the σ_v and the $V_{\max}$ is negative. For the spin and the metallicity distributions, up to $10^{10}h^{-1}M_\odot$ has positive kurtosis and thereafter negative. Therefore, we cannot consider that at $z = 3$ the properties of the subhalos living in the mid-mass halos follow a Gaussian distribution. We arrive to the same conclusion for the properties of the subhalos living in the low-mass halos. Note that the value of the kurtosis in the metallicity is not showed since is > 30. For subhalos living in the high-mass halos the trend changes, since for subhalos within the 5 most massive bins, the skewness of all properties (within the error bars) are compatible with zero. This, together with the fact that for σ_v, for the metallicity and for $V_{\max}$ the kurtosis of the most massive subhalos are compatible with zero, it may be that for the last bin of this mass the distribution can be considered normal.

- For $z = 1$ (the third and fourth rows of Fig. 12), none of the distributions of the subhalos living in the medium-mass halos and those living in the high-mass halos can be considered to follow a Gaussian distribution. For subhalos living in low-mass halos, those with a mass within the first mass bin have σ_v, spin and $V_{\max}$ distributions that are compatible with zero (within the error bars). For subhalos living in low-mass halos, those with a mass within the first mass bin have distributions of σ_v, spin and $V_{\max}$ that are compatible with the normal distribution because skewness and kurtosis are compatible with zero (within the error bars).

- At last, for $z = 0$ (from the fifth and sixth rows of Fig. 12) we come to the same conclusion as in the previous paragraph for the subhalos living in the low-mass halos, i.e., the only distribution that can be considered as normal is the one of the least massive mass bin for σ_v, spin and $V_{\max}$. None of the properties of subhalos living in mid-mass halos follow a normal distribution, since skewness and kurtosis cannot be considered zero at the same time for any mass bin. All properties of subhalos living in high-mass halos have a zero-compatible skewness (within the error bars), but the only mass bin that can be taken as following the normal distribution is found in metallicity and is the last mass bin.

4.   Halo scaling relations and the large-scale structure

In this section we will discuss about large-scale structure and structures in the cosmic web. We will first talk about the properties of the dark matter distribution in TNG100, and then define the cosmic web. Later we will talk about how the different structures of the cosmic web are classified, where we will see a method which uses the tidal field, which we will define and talk about its properties, and finally we will talk about the abundance of the halos in the different structures of the cosmic-web.
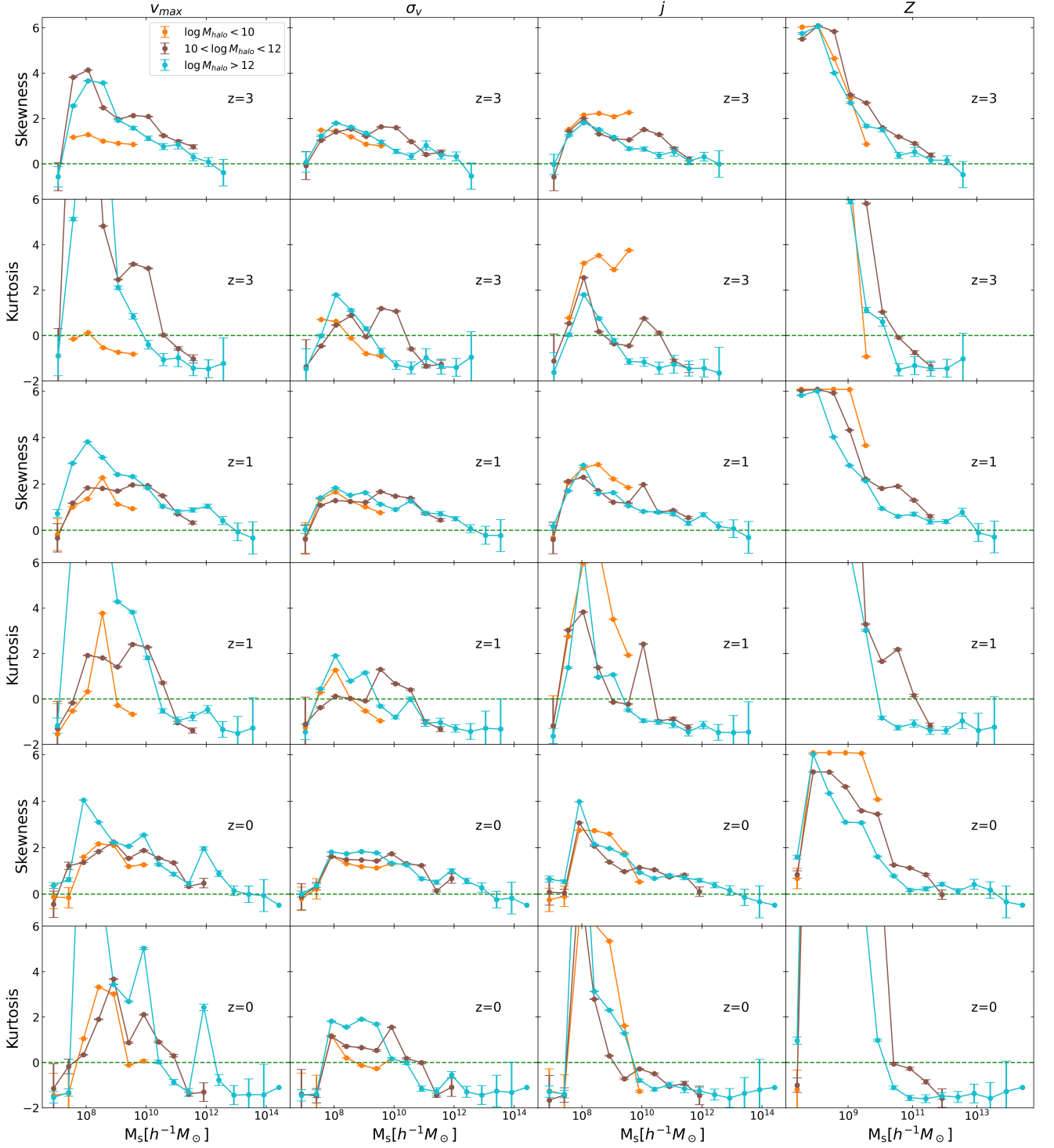
Figure 12: Evolution of the skewness and kurtosis of the CDF of the subhalo properties at the TNG100 simulation defined within each subhalo mass bin, due to the fact that we are analyzing the first-order scaling relations, at three different halo mass bins: $\log M_h[h^{-1}M_\odot] \leq 10$ (in orange), $10 < \log M_h[h^{-1}M_\odot] \leq 12$ (in brown) and $\log M_[h^{-1}M_\odot] > 12$ (in blue). The properties analyzed are, from left to right, $V_{\max}$, σ_v, j and Z, respectively. The dashed green line at the 0 value on the horizontal axis represents the value at which the skewness and kurtosis take the same value that a Gaussian distribution would take. The first two rows represent respectively the skewness and kurtosis at $z = 3$, the next two rows at $z = 1$ and the last two rows at $z = 0$.

4.1.   Properties of the dark matter distribution

We aim now at describing some statistical properties of the dark matter density field in the simulation, which will be key to characterize the cosmic-web. We obtain the density field through an interpolation of the particle distribution as shown in Appendix (B), where we discuss some of the most used schemes (first order, NGP, and second order, CIC). This interpolation
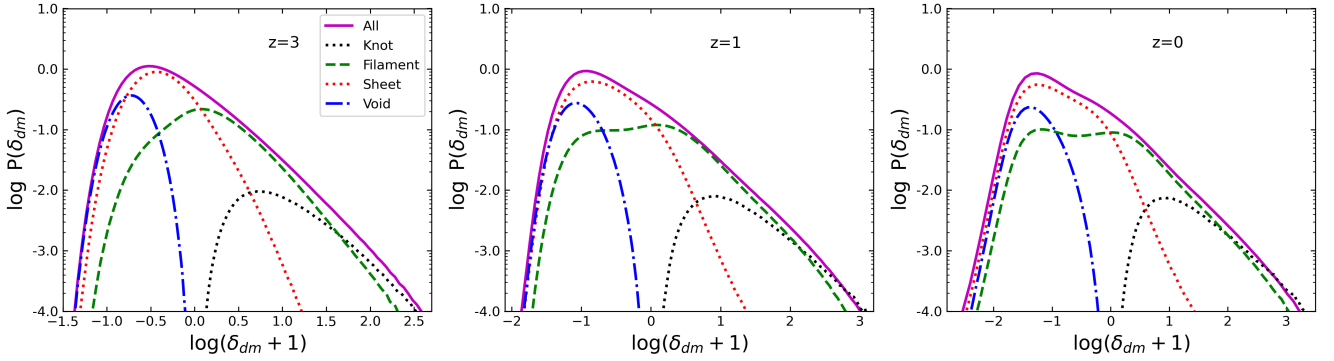
Figure 13: Probability distribution function of the different cosmic-web structures defined in §4.2, at the TNG100 simulation for the redshifts analyzed throughout the work, from left to right $z = 3$, $z = 1$ and $z = 0$. Note that what is labeled *All* gives probability distribution of the dark matter density as a whole.

is defined over a mesh of size N_{FT}^3 covering the volume of the simulation. We compute an overdensity $\delta = \rho/\bar{\rho} - 1$, where $\bar{\rho} = N_{tot}/N_{FT}^3$ is the mean number density of matter in the simulation and N_{tot} is the number of tracers within the simulated box. Appendix B, shows how the mass distribution $\rho(\mathbf{r})$ is calculated in this work.

The solid line in Fig. 13 shows the probability distribution of the dark matter density field at the three different redshifts analyzed during this work. As expected, the distribution at $z = 0$ shows the widest values of dark matter densities, meaning that the densest and the least dense regions are found in this redshift. At higher redshift, this distribution tends to become more Gaussian because it is evolving in a linear regime. To be more precise, we calculated the skewness and kurtosis of these distributions and the results are the following: At $z = 3$ the skewness is ~ 1.64 and the kurtosis is ~ 1.28, at $z = 1$ the skewness is ~ 1.71 and the kurtosis is ~ 1.68 and at $z = 0$ the skewness is ~ 1.9 and the kurtosis is ~ 2.5. This shift toward a more Gaussian distribution over time reflects the transition of dark matter from non-linear primordial conditions to more organized structures as the Universe has evolved.

Regarding the clustering of dark matter in the TNG simulation, Fig. 14 shows the power spectrum[4] at the TNG100 simulation compared to the linear (Eisenstein and Hu, 1999) and non-linear predictions (Takahashi et al., 2012). As predicted in §1.4, the power spectrum at large scales (i.e., low k) can be described by the linear theory but at small scales (i.e. high k) the power spectrum is described by the non-linear theory reflecting the formation of dense and compact structures. At the smallest scales the power spectrum we calculate does not match the theoretical prediction. This is because the corrections due to MAS are accurate up to $\sim 60\%$ of the Nyquist frequency, which in our case is $k_N = 21.45 h\mathrm{Mpc}^{-1}$ (see e.g. Cole et al., 2005). The theoretical predictions of power spectrum have been computed with the code `CosmiCCodes`[5].

4.2.   The cosmic-web classification

It has been observed (see e.g, Gao et al., 2005 ; Dalal et al., 2008 ; Hahn et al., 2009 ; Paranjape and Sheth, 2012 ; Wechsler and Tinker, 2018) that the statistical properties of dark matter halos can change according to both local and non-local properties of the underlying dark matter density field. Among other non-local properties, the so-called <u>tidal field</u>[6] (see e.g., Hahn et al., 2007 ; Paranjape et al., 2018).

In the current cosmological paradigm, i.e. in ΛCDM, galaxy properties are expected to depend strongly on the properties of the host halos. We have just seen in §3.3 an example of this: more massive halos are expected to host more massive subhalos. It is not clear to the community whether galaxy properties depend on the environmental properties at super-halo scales, since dynamical times (the time required to orbit across an equilibrium dynamical system), are longer or comparable to the Hubble time (defined as the inverse of the Hubble constant H_0 and estimates of the time scale on which the Universe evolves as a whole) at these scales. This indicates that there has not been enough time on super-halo scales to induce a direct environmental dependence by gravitational processes alone. However, it could still be possible for non-gravitational processes to introduce

---

[4]In Appendix D, we show how we have measured the power spectrum and its uncertainties.

[5]https://github.com/balaguera/CosmicCodes (Balaguera-Antolinez, A, 2024)

[6]The tidal field refers to the gravitational influence that a large body (such as a galaxy or a star cluster) exerts on a smaller body or on different parts of a stellar system. This phenomenon is crucial for understanding the dynamics and evolution of stellar systems because of its effects on the orbits and internal structure of the affected bodies (Ciotti, 2021).
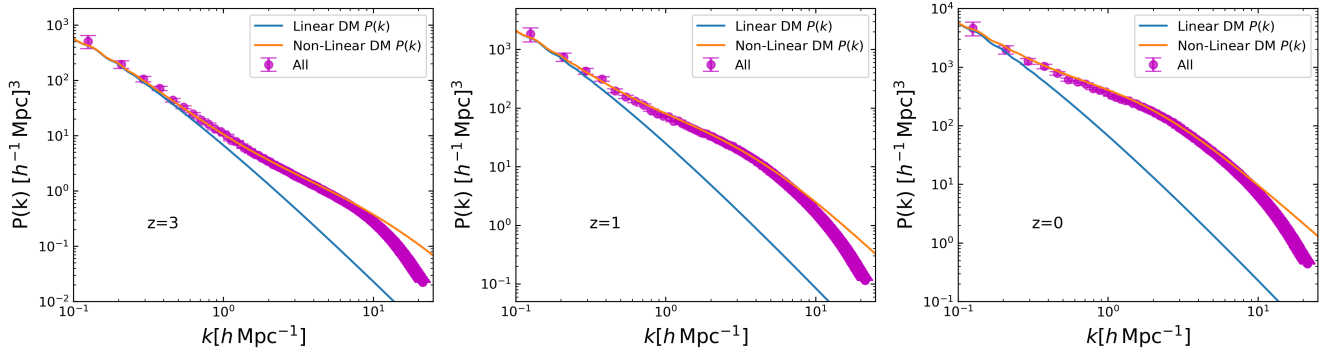
Figure 14: Dark matter power spectrum averaged in spherical shells at the TNG100 simulation at three different redshifts: from left to right $z = 3$, $z = 1$ and $z = 0$. The error bars denote the Gaussian approximation commented in §4.1. The measured power spectrum has been compared with the linear (blue line) and non-linear (orange line) predictions computed using the CosmiCCodes library (Balaguera-Antolinez, A, 2024) based on the fitting formulae by Eisenstein and Hu (1999) and the HaloFit revised by (Takahashi et al., 2012), respectively.

some environment dependence on large scales (Mo et al., 2010).

Numerical simulations and analytical works have shown that the gravitational amplification of small density fluctuations leads to a wealth of structures resembling the observed large-scale distribution of galaxies (see e.g. Davis et al., 1985 ; Springel et al., 2005). One of the most pioneering model was the one proposed by Zel'Dovich (1970), which showed us that the collapse of large scale perturbations takes place in an anisotropic way, occurring most rapidly along the shortest axis, taking the form of a pancake. The resulting mass density distribution can be thought to form a "cosmic web" (Bond et al., 1996) characterized by a complex network of *filaments* and *sheets* connecting *knots*, and separated by empty *voids*. Each of these environments has different statistical properties (see, e.g, Hahn et al., 2007), so it is inevitable to ask what the scaling relations of the objects living in these cosmological environments are like. Therefore, in this section we will characterize the dependencies of the scale relations in these environments.

Various techniques have been developed to define different environments present in the cosmic structure (see e.g., Schaap and Van De Weygaert, 2000 ; González and Padilla, 2010 ; Aragón-Calvo et al., 2010 ; Sousbie et al., 2011 ; Libeskind et al., 2018, and the references therein). In this work we use the most standard method, which is related with the eigenvalues of the tidal field. The tidal field is defined as the Hessian of the gravitational potential, i.e., $\mathcal{T}_{ij}(\mathbf{r}) = \partial_{ij}\phi(\mathbf{r})$ where $\phi(\mathbf{r})$ satisfies the Poisson equation

$$\nabla^2\phi(\mathbf{r}) = \delta_{dm}(\mathbf{r}). \tag{22}$$

To calculate the tidal field, we will solve the Poisson's equation using the *Fast Fourier Transform* (FFT) algorithm. Provided that the Fourier transform of the Laplacian operator acting over a function $g(\mathbf{r})$ is $\mathcal{F}\left[\nabla^2 g(\mathbf{r})\right] = -|\mathbf{k}|^2 \hat{g}(\mathbf{k})$, we can readily obtain the components of the tidal field as

$$\mathcal{T}_{ij} = \mathcal{F}^{-1}\left[\frac{k_i k_j}{k^2}\delta_{dm}(\mathbf{k})\right]. \tag{23}$$

Following Hahn et al. (2007), we characterize the cosmic-web using the eigenvalues λ_i, $(i = 1,2,3)$ of the tidal field. We use the number of eigenvalues of $\mathcal{T}_{ij}$ greater than the arbitrary λ_{th} to classify the four possible environments a halo may reside in. In analogy with Zel'dovich theory (Zel'Dovich, 1970), we define the following structures:

- *voids*: the region of space where $\mathcal{T}_{ij}$ has no eigenvalues above λ_{th}.

- *sheets*: the zones with one eigenvalue greater than λ_{th} and two eigenvalues less than λ_{th}.

- *filaments*: the sites with two eigenvalue greater than λ_{th} and one eigenvalues less than λ_{th}.

- *knots*: the region with all the three eigenvalues greater than λ_{th}.

We use $\lambda_{th} = 0$, which allows us to link knots (voids) with over-(under-) dense regions. At Appendix D, we show the code used to calculate this, at Code-Box 4 we calculate each component (i,j) of the tidal field and in Code-Box 5 the eigenvalues of the tidal field.

Combinations of the eigenvalues of the tidal field can provide information the different levels of anisotropy if cosmic environments. For example, the trace of the tidal tensor is the overdensity. This comes from the fact that the trace of the tidal tensor is $\text{Tr}(\mathcal{T}_{ij}) = \sum_i \mathcal{T}_{ii} = (\partial_{xx} + \partial_{yy} + \partial_{zz})\phi$, which is precisely the Laplacian of ϕ, which has been defined as the overdensity in Eq. (22).

One commonly used way to characterize the level of anisotropy of the cosmological environments is through the tidal shear q_R^2 (see e.g., Heavens and Peacock, 1988):

$$q_R^2 \equiv I_1^2 - 3I_2 = \frac{1}{2}[(\lambda_3 - \lambda_1)^2 + (\lambda_3 - \lambda_2)^2 + (\lambda_2 - \lambda_1)^2] \tag{24}$$

where $\lambda_1 \leq \lambda_2 \leq \lambda_3$ are the eigenvalues of $\mathcal{T}_{ij}$ and $I_1 = \lambda_1 + \lambda_2 + \lambda_3$ and $I_2 = \lambda_1\lambda_2 + \lambda_2\lambda_3 + \lambda_3\lambda_1$ are its first two rotational invariants. In general, q_R^2 reflects the anisotropy of the tidal environment at any scale R, vanishing for a perfectly isotropic environment. Other anisotropy parameters are the ellipticity e and the prolacticity p, defined as:

$$e = \frac{\lambda_3 - \lambda_1}{2\delta_{dm}} \, , \, p = \frac{\lambda_1 + \lambda_3 - 2\lambda_2}{2\delta_{dm}}.$$

Thus defined, e is a measure of the ellipticity in the (λ_1, λ_3) plane, and p determines the oblateness $(0 \leq p \leq e)$ or prolateness $(0 \geq p \geq -e)$ of the distribution of the dark matter particles. Otherwise, we can derive the tidal shear by $q_R^2 = \delta_{dm}^2(3e^2 + p^2)$. In this work, we compute the so-called tidal anisotropy parameter following Balaguera-Antolínez et al. (2024)

$$\mathcal{T}_A \equiv \frac{\sqrt{(\lambda_3 - \lambda_1)^2 + (\lambda_3 - \lambda_2)^2 + (\lambda_2 - \lambda_1)^2}}{2(2 + \delta_{dm})}. \tag{25}$$

where $2 + \delta_{dm}$ (instead of $1 + \delta_{dm}$) is used in the denominator to avoid divergences. Due to the threshold we chose to calculate the eigenvalues is 0, filaments and sheets will have a higher value of tidal anisotropy compared to voids and knots.

In Fig. 15 we present the relation between the halo mass and the tidal anisotropy ($\mathcal{T}_A$) of the cells where these halos are localized. We can observe that in all three redshifts shown, the tidal anisotropy in knots and voids is low compared to that seen in filaments and sheets. The halos at the low-mass end of the halos in filaments tend to be more anisotropic than the ones of mid-masses, where a minimum of anisotropy is reached (at $M_h \sim 10^{11} h^{-1} M_\odot$). The same trend appears at the halos living in knots but at smaller scales, so that at these masses the tidal forces will tend to be even more isotropic. In the case of the halos residing in sheets, at $z = 1$ and $z = 0$ the anisotropy reaches a maximum value at $M_h \sim 10^{9.5-10} h^{-1} M_\odot$.

4.3. Halo abundance in cosmic environments

The dotted lines in Fig. 13 shows the probability distribution of the dark matter density field for the different types of structures defined in §4.2 and for the three redshifts analyzed in the work. At $z = 3$, the range of halo densities goes from range of $\log(\delta_{dm} + 1) = [-1.5, 2.5]$, where voids and sheets dominate the under-density regions, and filaments and knots dominate the area where the density is positive (where, by definition, knots are those that are only positive). At lower redshifts, the CDF shifts more towards the low-density regions in the voids, and the opposite is true at the knots. This is understood as explained in §3.1, i.e. cosmic evolution implies that there is more collapse of matter, and therefore, there are both denser structures such as knots and less dense structures such as voids. On the other hand, the sheets and filaments span a much wider range of densities, with the sheets moving towards lower densities and the filaments towards higher densities when moving at lower redshifts.

The Tab. 5 shows the percentage of cells classified in the different cosmic-web environments. The effects of gravitational evolution and the formation of the cosmic-web is condensed in this table: as the Universe evolves, less cells are classified as knots and voids, but from Fig. 13 we know that these structures will tend to be denser and less dense, respectively. The number of cells classified as sheets and filaments increases with time.

In terms of halo abundances, Fig. 16 presents the mass functions of the haloes residing in the different environments. The low-mass end has the same slope in all environments for $z = 1$ and $z = 0$, but the position of the high-mass cutoff is a strong function of environment. As expected the mean halo density in higher in knots and lower in voids. At the low-mass end the filaments are the dominant structure of the mass function for all redshifts. The dominance of the knots in the mass function at $z = 3$ begins at $\sim 10^{9.5} h^{-1} M_\odot$ and at $z = 1$ and $z = 0$ at $\sim 10^{10} h^{-1} M_\odot$. At the high-mass end, the filaments dominate again the mass-function. Note that at $z = 1$ and $z = 0$ the knots don't have a contribution to the mass-function.

In Fig. 16, the filaments show a change of trend near the middle of the mass function. This trend is also shown in Fig. 13,
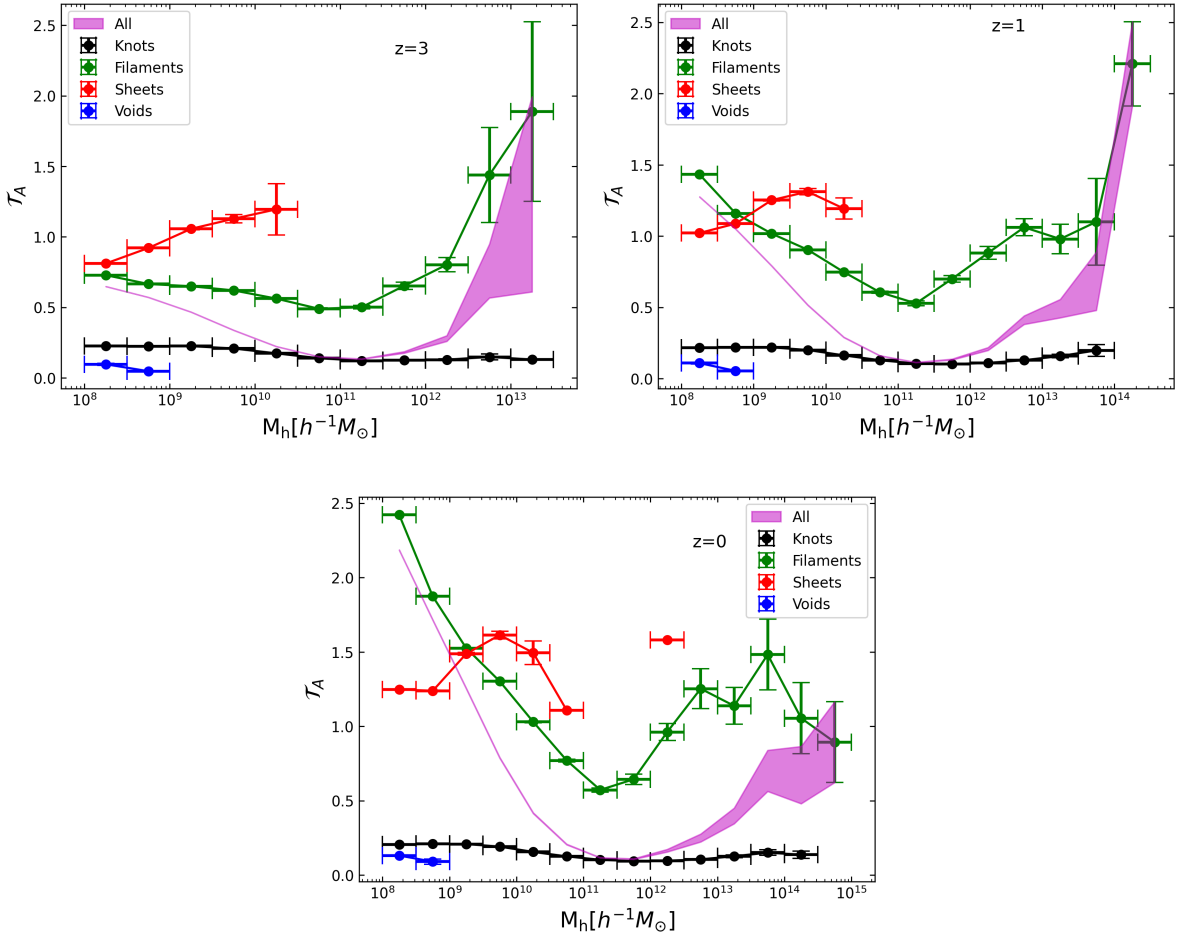
Figure 15: Relation between the halo mass and tidal anisotropy of the cells where this halos are localized defined in the different cosmic-web structures, i.e., *knots* (in black), *filaments* (in green), *sheets* (in red) and *voids* (in blue) at the TNG100 simulation for the redshifts analyzed throughout the work, from left to right $z = 3$, $z = 1$ and $z = 0$.
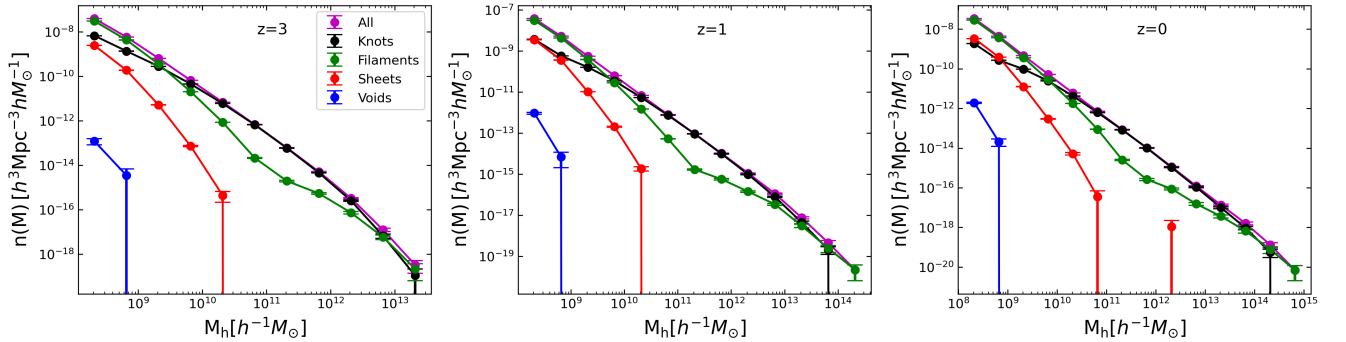

Figure 16: Binned mass function of haloes residing in the different cosmic-web structures, i.e., *knots* (in black), *filaments* (in green), *sheets* (in red) and *voids* (in blue) at the TNG100 simulation for the redshifts analyzed throughout the work, from left to right $z = 3$, $z = 1$ and $z = 0$. As in Fig. 2, the error bars are Poisson's bars.

where a plateau (at $z = 1$) or even a minimum (at $z = 0$) appear. At $z = 3$ there is a change of slope before the maximum at $\log(\delta_{dm} + 1) = 0$. All this information shows a bimodality of the distribution for the filaments near the mean density, i.e, $\log(\delta_{dm} + 1) = 0$. One hypothesis for this bimodality is that there are two distinct populations of halos residing on filaments and differentiated by the density of the underlying dark matter density field. Understanding this bimodality may be a goal of future work.

	$z = 3$	$z = 1$	$z = 0$
Void	16.53	15.58	13.36
Sheet	61.81	62.78	63.69
Filament	20.77	21.15	22.64
Knot	0.89	0.49	0.31

Table 5: Percentage of cells classified according to cosmic web classification (as mentioned in §4.2 at the TNG100 simulation, with $\lambda_{th} = 0$) for the redshifts $z = 3$, $z = 1$ and $z = 0$ (from left to right).

4.4.   Scaling relations in different cosmic environments

In this section we calculate the first- and second-order scaling relations for the different cosmic environments defined in §4.2. The first-order scaling relations of the properties expressed in §3 are shown in Fig. 17. At first glance, subhalos living on filaments and knots tend to have the largest values for each property and each redshift. Apart from that, the properties in the voids at $z = 3$ do not follow the same trends as the other environments, but over time these trends will eventually become the same.

The slopes for $V_{\max}$ (i.e. the first row in Fig. 17) of the subhalos living in halos residing in knots are a bit lower that the slopes of the filaments at $z = 3$, since at the low-mass end, the $V_{\max}$ of the knots dominate the distribution and at the high-mass end, the filaments will have the same $V_{\max}$ as the knots. The difference of the slopes increase with redshift. The slopes of the sheets also are higher following the same argumentation. For all redshifts the filaments are the environment with the highest $V_{\max}$ closely by the knots, and then the sheets and the voids. The filaments show a pair of values in the mean mass range at $z = 1$ and $z = 0$ that are off trend. As showed in §3.2, the main difference between the redshifts reside in the amplitude of the values, specifically in the low-mass end and in the high-mass end. This amplitude is higher at redshift but noticeable in knots and filaments in low mass subhalos and only in filaments at high masses.

The information we get from the velocity dispersion (second row in Fig. 17) is the same as the one just mentioned in the previous paragraph, i.e., the subhalos living in the filaments and knots tend to have higher velocity dispersion compared to the sheets and knots. In addition, we also find those values of σ_v higher than the trend for the intermediate masses.

With respect to spin (third row in Fig. 17), there are not very large differences between the different environments at the low-mass range, although the subhalos living in the sheets have on average less spin (except for the subhalos with $M_s \leq 10^8 h^{-1} M_\odot$). For $z = 3$ the subhalos living in the filaments will have the highest spin for all the distribution, while for $z = 1$ and $z = 0$ it is the knots that dominate. Despite this, the more massive subhalos residing in filaments at these last two redshifts will on average have higher spin, which makes sense because of the tidal forces suffered by the more massive subhalos are lower compared to the forces suffered by the massive subhalos in knots.

The metallicity is the property which more differences are shown between one environment to another. The first thing we realize is that the metallicity in voids is negligible since there are usually fewer interactions in these regions and therefore the probability of star formation is reduced. On the other hand, at low-mass ranges of subhalo masses, the knots present the highest fraction of metals compared with the other environments, This can be explained by the fact that in these environments gravitational interactions and mergers between galaxies are more common, leading to episodes of active star formation and metal accretion. Note that for higher masses, all environments converge to a value of ≈ 0.01, so we can conclude that at low mass there are differences between environments, but not at high mass.

Figure 18 shows the same plot showed in the Fig. 7 but for the four cosmic-web environments showed in §4.2. From the relationship between M_h and M_s, the average of the subhalos hosted by the halos (in practically the entire mass range) that are part of the knots will have on average more mass. This makes sense because the mass function showed in Fig. 16 also tends to that, meaning that the denser the environment, the higher subhalo mass they will accrete. The halos that are part of filaments will have, on the other hand, a larger amount of substructures for the whole mass range compared to the halos considered in knots, except for $z = 0$ where it is practically the same. Therefore, joining the information of these two plots, we conclude that although the halos with more substructures are those living in filaments, the halos living in knots will have on average the most massive subhalos. This is corroborated by the value of skewness since throughout the mass range, the ratio $M_s - M_h$ tends to have a higher value in filaments, which means that here the distribution of subhalos within each halo mass bin will tend to be more populated at lower values (in mass) of the distribution.

The mass of the subhalos that live in the halos that form the voids and sheets ascend monotonically with the mass of the halo
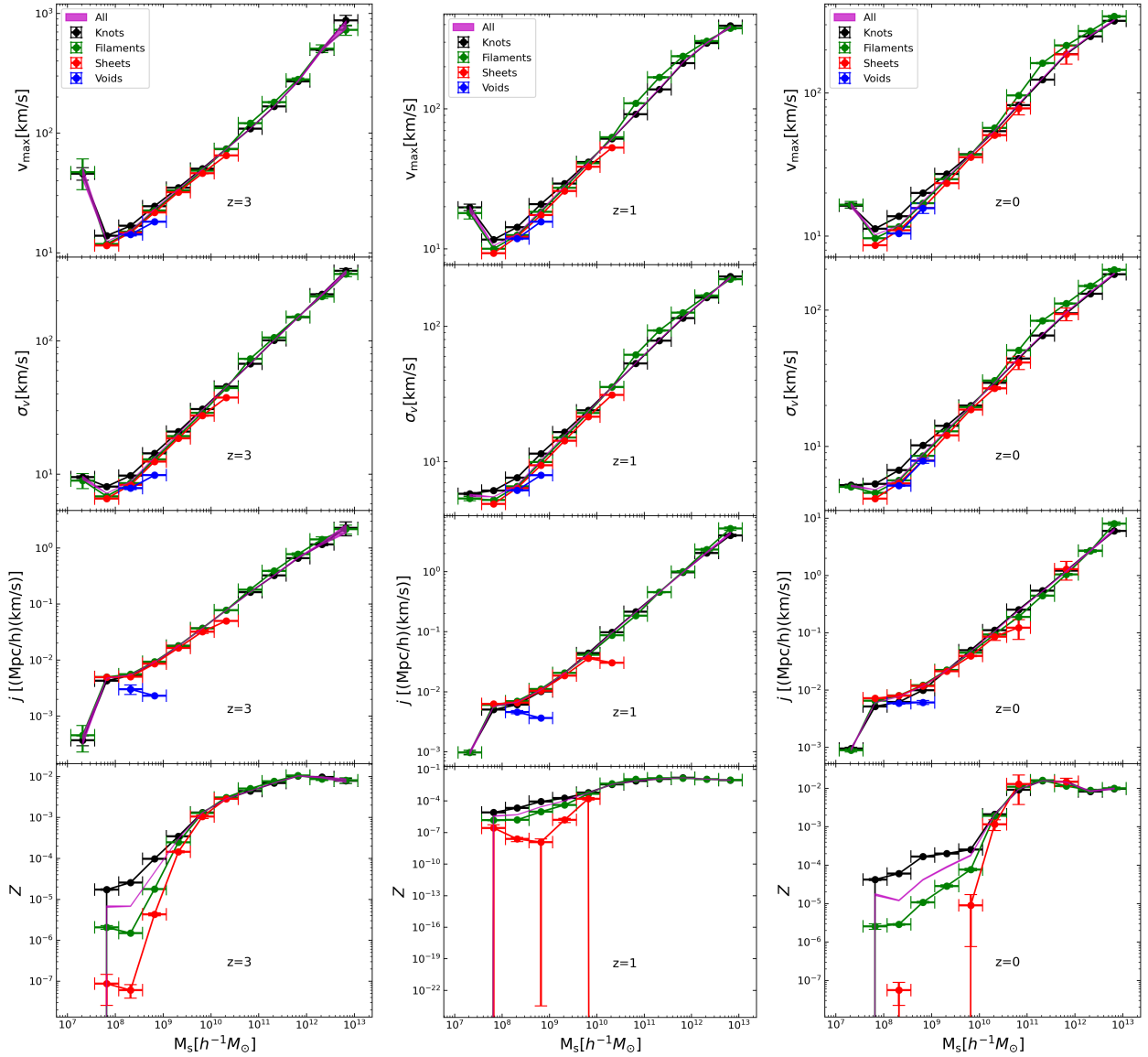
Figure 17: First-order scaling relations of the subhalo properties (i.e., with respect to M_s) at the TNG100 simulation at the four cosmic-web environments showed in §4.2: *knots* (in black), *filaments* (in green), *sheets* (in red) and *voids* (in blue). The properties analyzed from top to bottom are: σ_v, the spin, the metallicity and the $V_{\max}$, respectively and this has been done at three different redshifts, from left to right $z = 3$, $z = 1$ and $z = 0$. Note that what is labeled *All* gives the same information as in Fig. 5.

that hosts them. This is because, as explained in §3.3, the halo is formed from very few substructures. Despite this, the halos that form in the sheets can reach masses on the order of $\sim 10^{10} h^{-1} M_\odot$. At these masses the halos already begin to have a larger substructure and therefore, the relation $M_s - M_h$ begins to descend and starts to be a little out of the monotonic trend. At §3.3, we discuss that the mass at which the average $M_s - M_h$ scaling relation saturates is $M_h \sim 10^{10.5-11} M_\odot$. We do not have halos in sheets and voids with so much mass so for these structures there will be no noticeable saturation, so there will be no change of trend in the second order relations. In order to understand what form the second-order scaling relations will have in the different filaments and knots, we will obtain the best fit for the parameters a, b and c of Eq. 20, which are shown in Tab. 6. Using that information we can confirm that the $M_s - M_h$ relation saturates and, hence, second-order scaling relations in the knots and filaments will have a maximum value.

Figure 19 show the second-order scaling relations in the different cosmic environments, which confirm us that the voids and sheets do not have maxima in any of the analyzed properties as $M_{h,\max} < M_{h,\text{break}}$, as predicted above. Up to that mass, the scaling relations evolve analogously to the first-order scaling relation, as was the case in §3.3.

On the other hand, the scaling relations of the properties that give us a direct diagnostic of the depth of the potential well, i.e., $V_{\max}$ and σ_v will have a different amplitude at the time of maximum for filaments and knots, which decreases as redshift
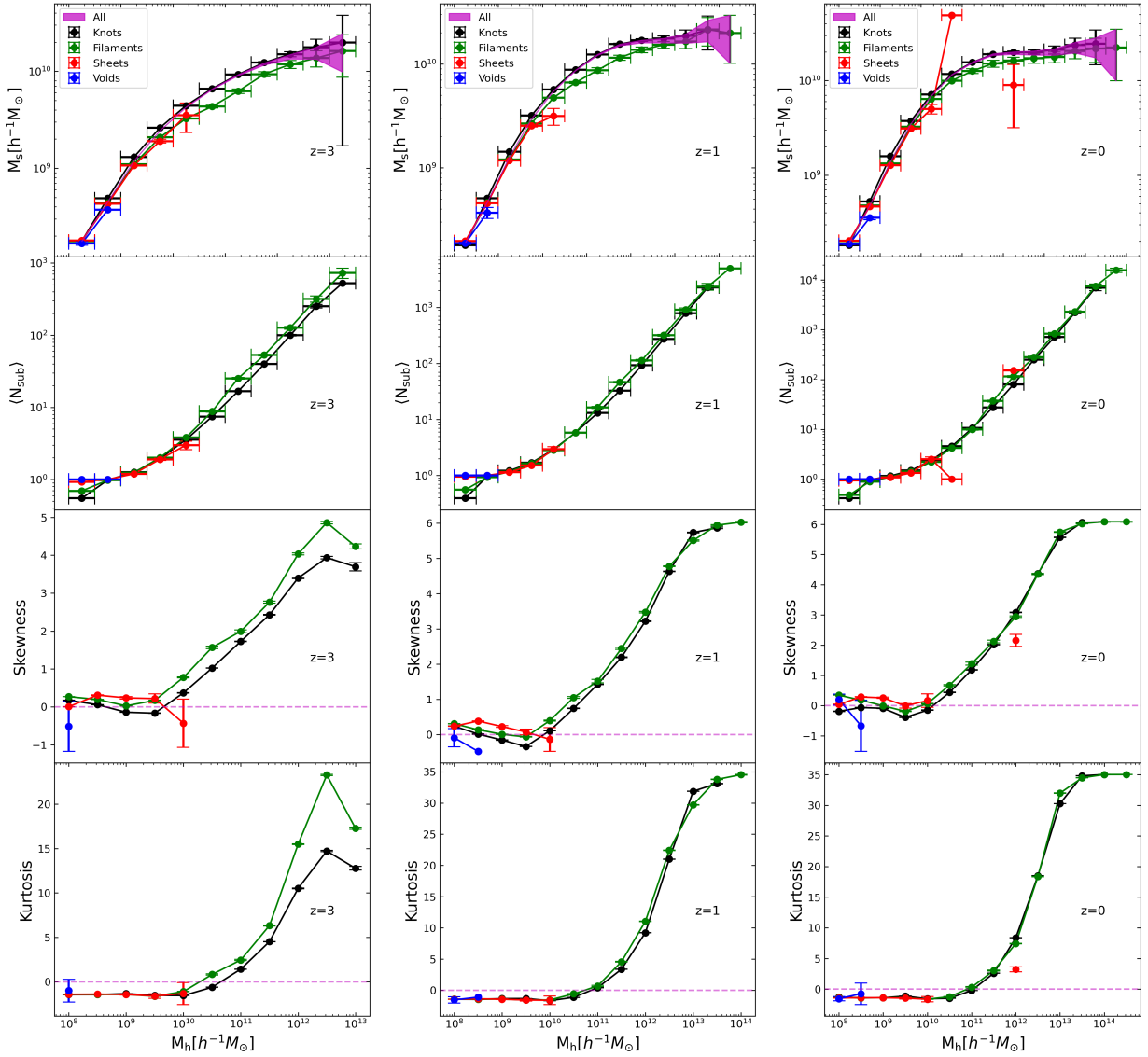
Figure 18: First row: Scaling relation of M_s with respect to M_h. second row: Halo occupation distribution. Third row: Skewness of the second-order scaling relation of M_s. Last row: Kurtosis of the second-order scaling relation of M_s. All this four plots are computed at the TNG100 simulation at three different redshifts, from left to right: $z = 3$, $z = 1$ and $z = 0$, respectively. Unlike the Fig. 7, this has been done at the four at the four cosmic-web environments showed in §4.2: *knots* (in black), *filaments* (in green), *sheets* (in red) and *voids* (in blue). Note that what is labeled *All* gives the same information as the first panel in Fig. 7.

decreases as well. This comes directly from the $M_s - M_h$ relation, because the slope of that relation in filaments increase as redshift decreases (see Tab. 6). From Fig. 17, we show that the slope of the scaling relation of the $V_{\max}$ and the σ_v with respect to the M_s is also higher in filaments. Thus, using the Eq. (21) We demonstrate that the difference in the mean value of $V_{\max}$ and σ_v at the time of maximum for filaments and knots decreases.

The ratio $j - M_h$ (third row in Fig. 19) has, in general, the same form obtained in Fig. 9. In spite of this, for redshifts $z = 1$ and $z = 0$, the subhalos that live in more massive halos within the filaments will have on average a greater j. This is because the tidal forces will be less intense in the less dense regions, affecting less, compared to the knots, to the reduction of angular momentum. As the redshift decreases, the halos belonging to the filaments will tend to have subhalos with higher angular momentum since the effect of tidal forces becomes more pronounced as the redshift decreases (see §3.4).

Finally, the ratio $Z - M_h$ shows that there are no obvious differences between the mean of Z of the subhalos in the considered higher density environments. On the other hand, the voids will have a negligible metallicity because, as shown earlier in this section. Finally the subhalos living in sheets tend to have a lower Z compared with the knots and filaments because the lower density causes structures to form fewer stars.
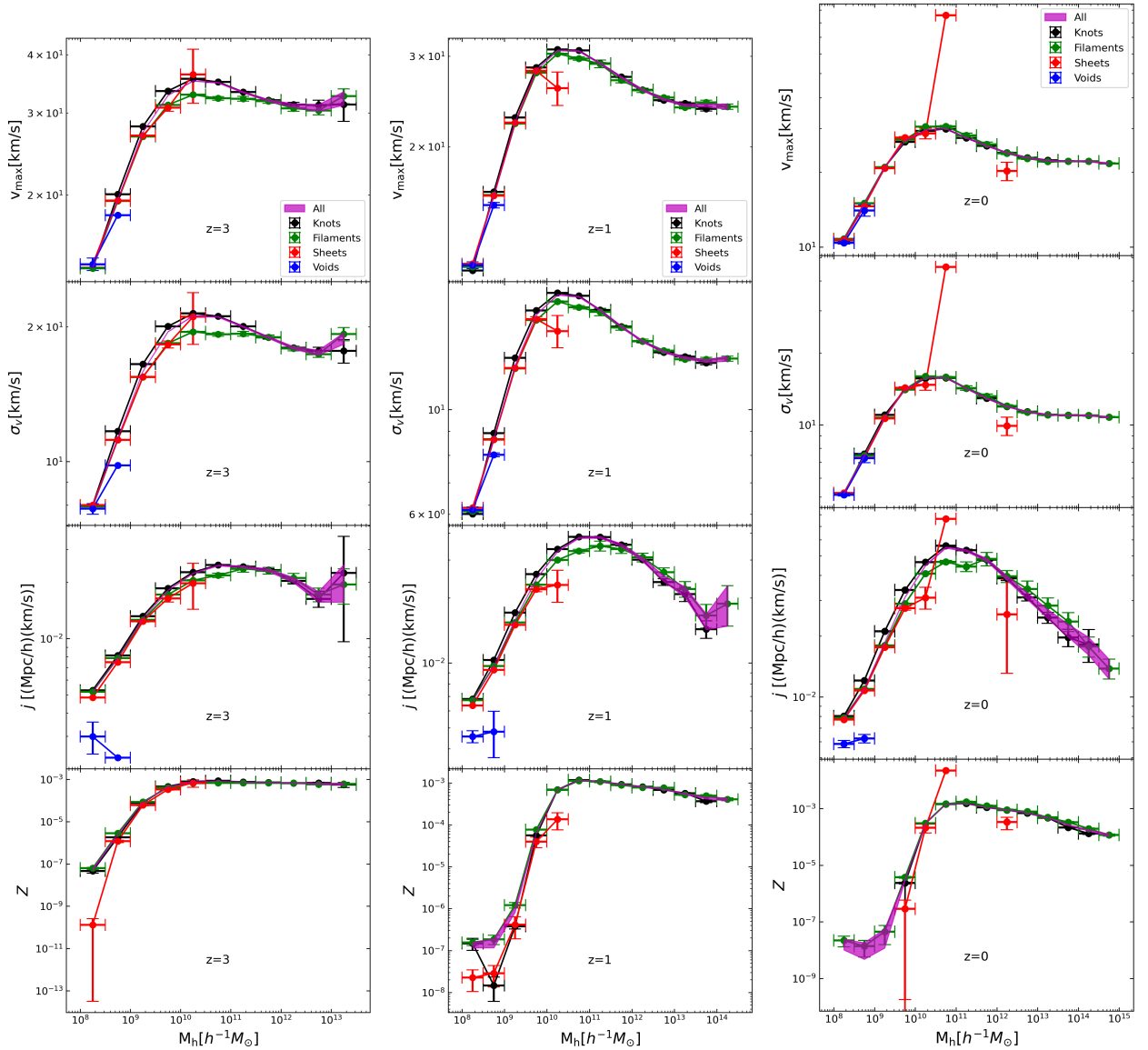
Figure 19: Second-order scaling relations of the subhalo properties (i.e., with respect to M_h) at the TNG100 simulation at the four cosmic-web environments showed in §4.2: *knots* (in black), *filaments* (in green), *sheets* (in red) and *voids* (in blue). The properties analyzed from top to bottom are: σ_v, the spin, the metallicity and the $V_{\max}$, respectively and this has been done at three different redshifts, from left to right $z = 3$, $z = 1$ and $z = 0$. Note that what is labeled *All* gives the same information as Fig. 7.

5. The halo bias and connection to large-scale analysis

5.1. Estimators of effective bias

Based on the Eq. (16), Paranjape et al. (2018) constructed an object-by-object estimator of large-scale linear halo bias, whose average reproduces the known trends derived from traditional estimators (as shown in Balaguera-Antolínez et al., 2024). To this aim we first measure the halo-matter cross power spectrum in the simulated box. For this we need the positions of the haloes indexed by a variable h. Once we have the positions of the halos $\mathbf{x}_h$ inside the simulated box of volume V_{box} and a grid with N_g cubic cells, we define the overdensity of the halos $\delta_{\text{halo}}(\mathbf{x})$ at the grid cell with position $\mathbf{x}$ as

$$\delta_{\text{halo}}(\mathbf{x}) \equiv n_{\text{halo}}(\mathbf{x})/\bar{n}_{\text{halo}}(\mathbf{x}) - 1 = \sum_h N_g \vartheta(\mathbf{x}, \mathbf{x}_h) / \sum_h -1, \tag{26}$$

		a	b	c
z=3	Knots	-4.70 ± 0.77	2.32 ± 0.15	-0.09 ± 0.01
	Filaments	-2.62 ± 0.86	1.92 ± 0.16	-0.07 ± 0.01
z=1	Knots	-5.79 ± 0.86	2.53 ± 0.16	-0.10 ± 0.01
	Filaments	-3.08 ± 0.84	2.01 ± 0.15	-0.07 ± 0.01
z=0	Knots	-5.71 ± 1.07	2.51 ± 0.19	-0.10 ± 0.01
	Filaments	-3.73 ± 1.06	2.13 ± 0.19	-0.08 ± 0.01

Table 6: Parameters of the best fit of the Eq. (20) for the halos residing in knots and filaments at three different redshifts, from top to bottom: $z = 3$, $z = 1$ and $z = 0$, respectively

where $\vartheta(\mathbf{x}, \mathbf{x}_h)$ is the selection function that gives the contribution of the halo at position $\mathbf{x}_h$ to cell $\mathbf{x}$ and satisfies that is 1 when summed over all cells. So the number density of the halos is $n_{\text{halo}}(\mathbf{x}) = \sum_h \vartheta(\mathbf{x}, \mathbf{x}_h)$ and the mean number density is $\bar{n}_{\text{halo}}(\mathbf{x}) = \sum_{\{\mathbf{x}\}} n_{\text{halo}}(\mathbf{x}) / \sum_{\{\mathbf{x}\}} = \sum_h 1/N_g$, since $\sum_{\{\mathbf{x}\}} = N_g$. The discrete Fourier transform of $\delta_{\text{halo}}(\mathbf{x})$ is:

$$\delta_{\text{halo}}(\mathbf{k}) \equiv \frac{1}{N_g} \sum_{\{\mathbf{x}\}} e^{i\mathbf{kx}} \delta_{\text{halo}}(\mathbf{x}) = \left[\sum_h \sum_{\{\mathbf{x}\}} e^{i\mathbf{kx}} \vartheta(\mathbf{x}, \mathbf{x}_h) / \sum_h \right] - \sum_{\{\mathbf{x}\}} e^{i\mathbf{kx}} / N_g = \sum_h e^{i\mathbf{kx}} / \sum_h -\delta_{\mathbf{k},0}^{\text{K}}, \tag{27}$$

where the superscript K in the last term refers to the Kronecker delta. This term tells us that k cannot be 0 since $\delta_{\text{halo}}(\mathbf{k})$ cancels out. With this, we can write the power spectra required to calculate the bias described in Eq. 16 by averaging over $\mathbf{k}$ spherical shells (which we denote as $\langle \rangle_k$). as $P_{hm}(k) = V_{box} \langle \delta_{\text{halo}}(\mathbf{k}) \delta^*(\mathbf{k}) \rangle_k = V_{box} \sum_h \langle e^{i\mathbf{kx}} \delta^*(\mathbf{k}) \rangle_k / \sum_h$ and $P_{\text{dm}} = V_{box} \langle \delta(\mathbf{k}) \delta^*(\mathbf{k}) \rangle_k$. Therefore, we can obtain

$$b_{hm}(k) = \sum_h \left(\frac{V_{box}}{P_{\text{dm}}} \langle e^{i\mathbf{kx}} \delta^*(\mathbf{k}) \rangle_k \right) / \sum_h \equiv \sum_h b_{1,h}(k) / \sum_h, \tag{28}$$

where $b_{1,h}(k)$ is the definition of the object-by-object, scale-dependent quantity. The effective bias estimator at large scales can be obtained from the average of the $b_{1,h}(k)$ values over a range of wavenumbers $k < k_{max}$ where the ratio between the halo and matter spectra is constant:

$$b_{1,h} = \sum_{}^{k<k_{max}} N_k b_{1,h}(k) / \sum_{}^{k<k_{max}} = \sum_{}^{k<k_{max}} N_k \left(\frac{V_{box}}{P_{\text{dm}}} \langle e^{i\mathbf{kx}} \delta^*(\mathbf{k}) \rangle_k \right) / \sum_{}^{k<k_{max}} N_k, \tag{29}$$

We will refer to this quantity as halo-by-halo (subhalo-by-subhalo) bias, when it has the subscript h (s). By assigning the bias to each object, we can statistically analyze the effective bias based on the properties of the halo, whether primary or secondary, without the need to divide the sample or use the statistic to two points. Eq. (28) has been implemented to calculate the assembly bias of both halos and galaxies (see e.g., Balaguera-Antolínez et al., 2024; Contreras et al., 2021; Paranjape et al., 2018; Ramakrishnan et al., 2019). In Fig. 22 we present the halo bias and subhalo bias at $z = 0$. In Fig. 21 we show the power spectrum of subhalos, halos[7] and dark matter, in order to see if the range of wavenumber in which both the ratio between halo and dark matter power spectrum and the ratio between subhalo and dark matter power spectrum is constant. At high redshifts we can see that the ratio between halo and dark matter power spectrum is constant (within error bars) until near $k = 1$. However, if we look at the third panel of Fig. 21, we realize that the ratios start to become scale-dependent earlier. Therefore, we will set the wavenumber range to $k \leq 0.3 h\text{Mpc}^{-1}$ for subhalos and $k \leq 0.4 h\text{Mpc}^{-1}$ for halos. With this, we ensure that all the biases we measure are of large-scale bias.

The first row of Fig. 23 shows the scaling relation between the effective bias of the halo and the mass of the halo for the $z = 3$ and $z = 1$ (note that $z = 0$ is showed in Fig. 22). The second row show shows the scaling relation between the effective bias of the subhalo and the mass of the subhalo. We also show fitting formula of Tinker et al. (2010), calibrated from N-body simulations of halos with a mass resolution of $\geq 10^{11} M_\odot$. In all the mentioned panels the prediction differs from the signal measured from the TNG.

From Fig. 22 and 23 we see how both the mean value of both biases and the range of these values increases with increasing redshift. In the case of subhalo bias it reaches maximum values of $b_{sm} \sim 9$ at $z = 3$, $b_{sm} \sim 5$ at $z = 1$ and $b_{sm} \sim 4$ at $z = 0$.

---

[7]Computed using the code shown in Appendix D, where the density field has been calculated by interpolating the catalog of halos or subhalos in a grid using CIC to later calculate the overdensity field.
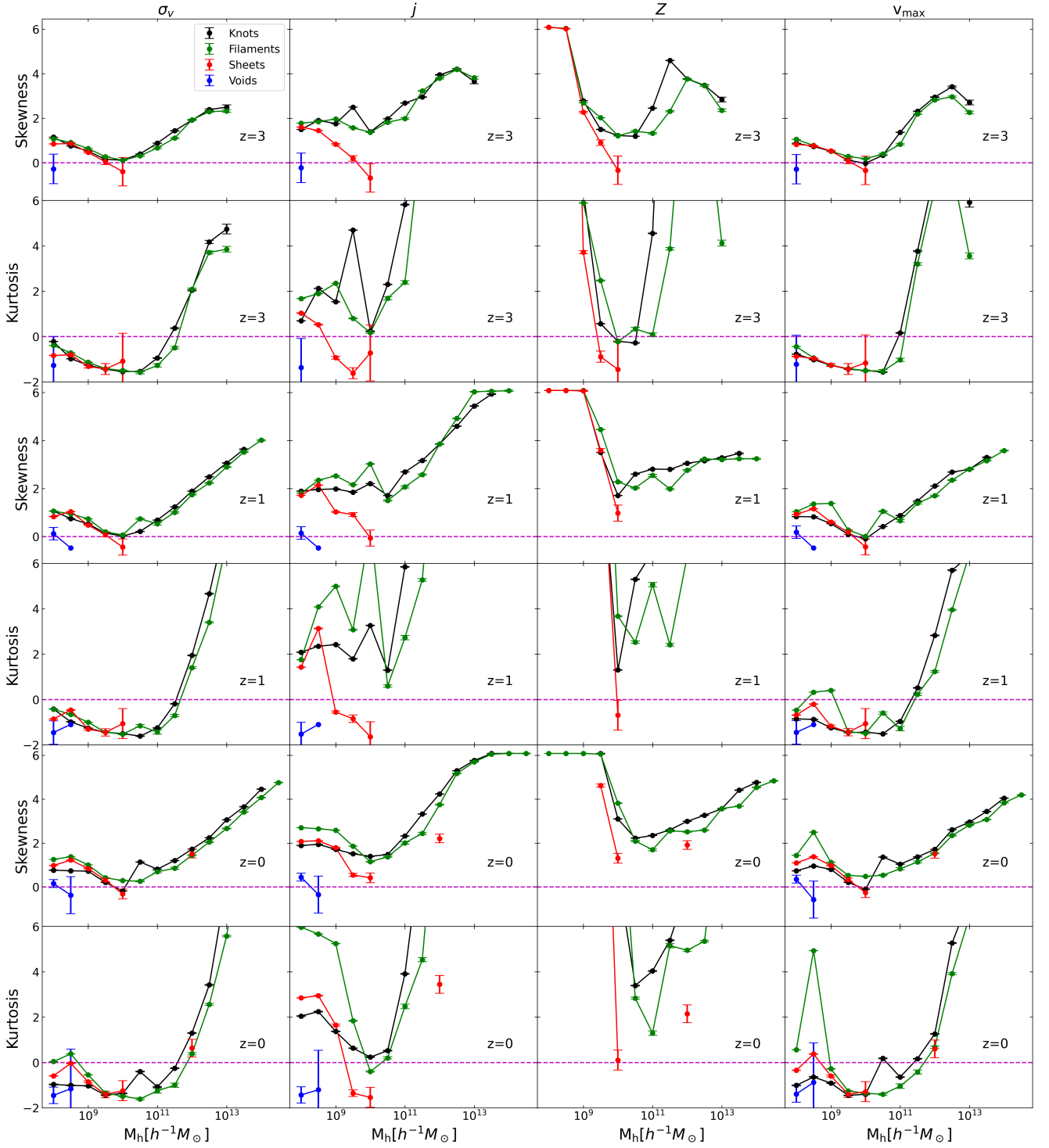
Figure 20: Evolution of the skewness and kurtosis of the CDF of the subhalo properties at the TNG100 simulation defined within each halo mass bin, due to the fact that we are analyzing the second-order scaling relations, at the four cosmic-web environments showed in §4.2: *knots* (in black), *filaments* (in green), *sheets* (in red) and *voids* (in blue). The properties analyzed are, from left to right, the σ_v, j and Z, $V_{\max}$, respectively. The dashed green line at the 0 value on the horizontal axis represents the value at which the skewness and kurtosis take the same value that a Gaussian distribution would take. The first two rows represent respectively the skewness and kurtosis at $z = 3$, the next two rows at $z = 1$ and the last two rows at $z = 0$.

This is mainly due to differences in the structure formation process at different redshifts. Dark matter halos form at peaks of density fluctuations, which were rarer and more extreme at higher redshift. As the Universe expands and evolves, these fluctuations grow and become more common, so structures at higher redshift tend to be more biased (see e.g., Bardeen et al., 1986b; Basilakos et al., 2008).
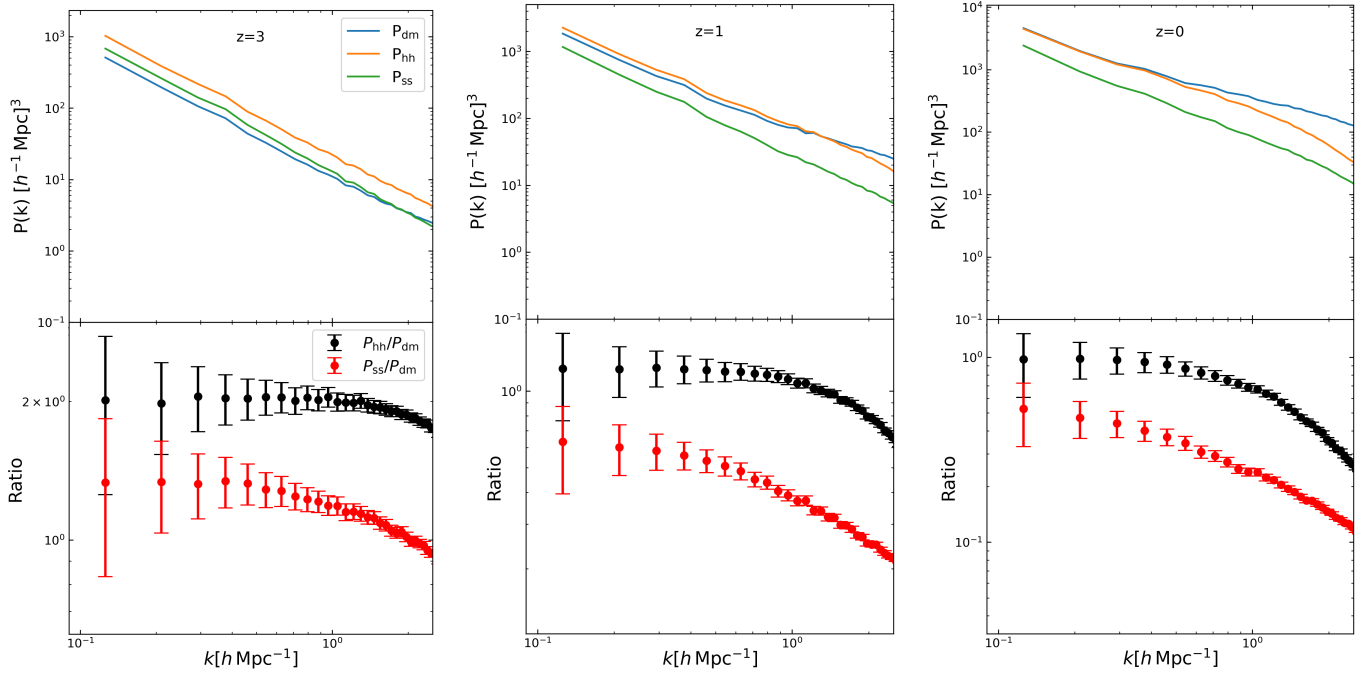
Figure 21: Top row: Comparison between the dark matter power spectrum, P_{dm} (in blue), the halo power spectrum, P_{hh} (in orange) and the subhalo power spectrum, P_{ss} (in green) averaged in spherical shells at the TNG100 simulation. Note that the power spectrum should be an errorbar plot (as shown in Fig. 14), but it is shown as a solid line for visual comparison. Bottom row: ratios $P_{\mathrm{hh}}/P_{\mathrm{dm}}$ (in black) and $P_{\mathrm{ss}}/P_{\mathrm{dm}}$. Both of them at three different redshifts: from left to right $z = 3$, $z = 1$ and $z = 0$.

Figure 24 shows the comparison between the b_{hm} and the b_{sm} as function of halo masses[8]. In general, the halos are more biased than the subhalos (except for the high-mass halos at $z = 0$) because halos form earlier than subhalos, which means that the density peaks where these halos form are less common than those where subhalos form, making it more clustered on average. Despite this, the distribution of both halos and subhalos is less than unity at $z = 0$, so we can be sure that dark matter will have higher clustering than these tracers. In other words, these tracers at this redshift and at large scales will tend to be organized slightly more homogeneously than dark matter.

Figure 25, shows the scaling relation of the b_{hm} and the b_{sm} as a function of halo and subhalo masses, respectively at the cosmic-web structures shown in §4.2. Voids show a negative bias for all redshifts indicating that the halos are anticorrelated with high density regions. On the other hand, low-mass halos living in knots tend to have lower clustering in comparison with the low-mass subhalos living in filaments and sheets, since there is a higher matter density in these regions, which means that the presence of these halos is more common and less distinct compared to the dense environment in which they are found. As the redshift decreases, the bias of the three structures that have a positive bias tend be less clustered. This is understandable from the point of view that with the decreasing redshift bias also decreases. Halos belonging to knots at $z = 0$ will have a clustering $\lesssim 0$.

The bias of subhalos living in knots, filaments and sheets tend to have the same clustering for all redshifts for subhalos of $M_s \sim 10^{8-8.5} h^{-1} M_\odot$. For all redshifts and in all mass ranges, the bias in the subhalos living in filaments will tend to be larger than that in knots. The sheets, on the other hand, at $z = 0$ have two mass bins (which are of low mass) in which it is lower than the subhalos of the knots. As in the halos, the voids show an anti-correlation with the matter density. The highest difference between the clustering of the subhalos in filaments and in knots is found at $z = 1$, at $M_s \sim 10^{13} h^{-1} M_\odot$. Summarizing, it is important to take into account the structures of the cosmic-web in which both halos and subhalos live when measuring the bias.

---

[8]Neither property corresponds exactly to the properties shown in lines 1 and 2, respectively, since b_{hm} has been measured up to $k \leq 0.3 k\mathrm{Mpc}^{-1}$ and b_{sm} is shown as a function of the mass of the halo in which the subhaloes live. This is done in order to be able to compare these two quantities.
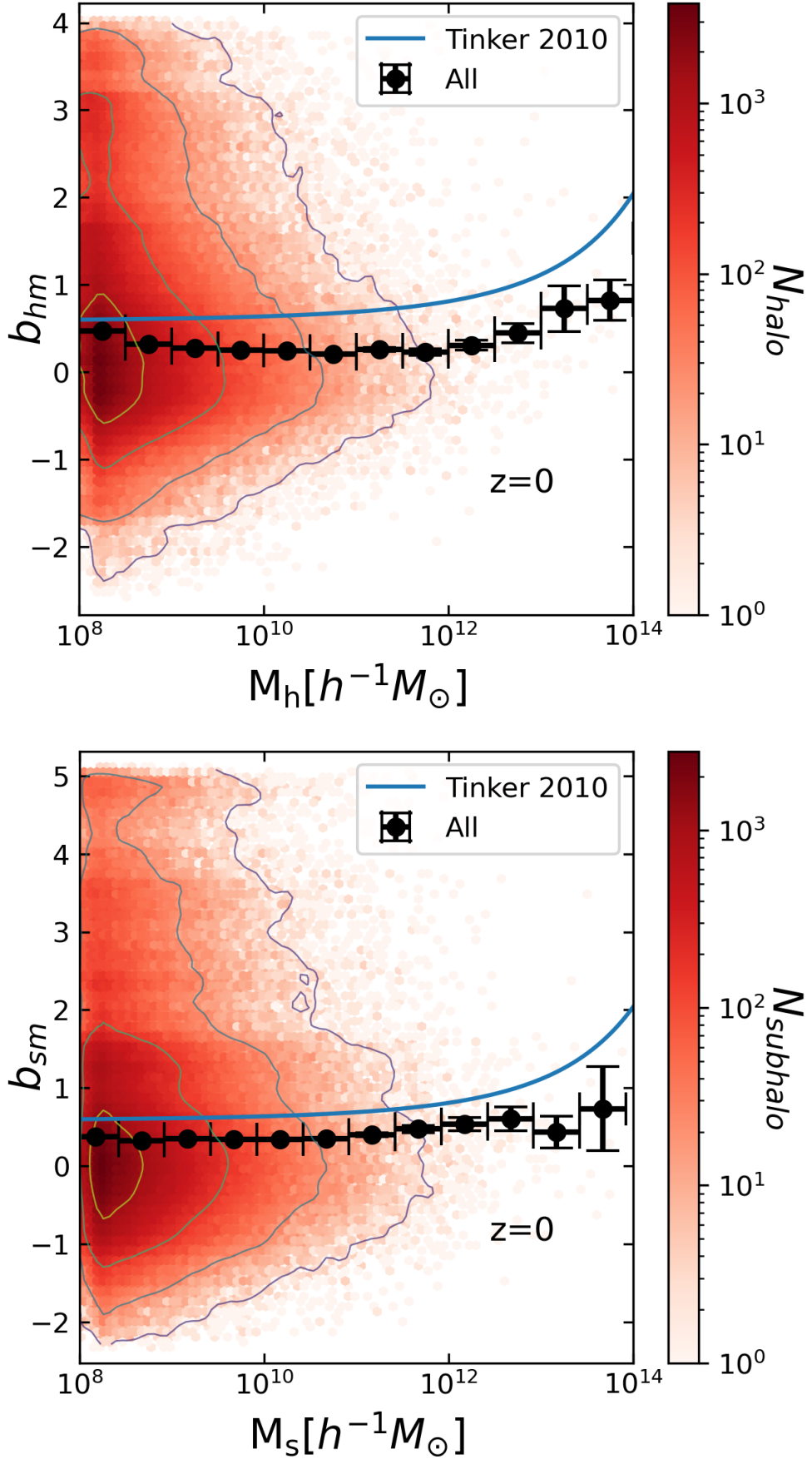
Figure 22: Upper plot: Halo effective bias b_{hm} computed with Eq. 28 as a function of halo mass at $z = 0$. Lower plot: Subhalo effective bias b_{hm} computed with Eq. 28 as a function of subhalo mass at $z = 0$. In both cases, the error bars denote the standard error of the mean in each mass bin. The blue line in this two rows shows the prediction of (Tinker et al., 2010). The contours indicate a region of an equal number of halos/subhalos $\log N = [3.1, 2.3, 1.4, 0.5]$.

Figure 23: First row: Halo effective bias b_{hm} computed with Eq. (28) as a function of the halo mass. Second row: Subhalo effective bias b_{sm} computed with Eq. (28) as a function of the subhalo mass. In both cases, the error bars denote the standard error of the mean in each mass bin. The blue line in this two rows shows the prediction of (Tinker et al., 2010). The contours indicate a region of an equal number of halos/subha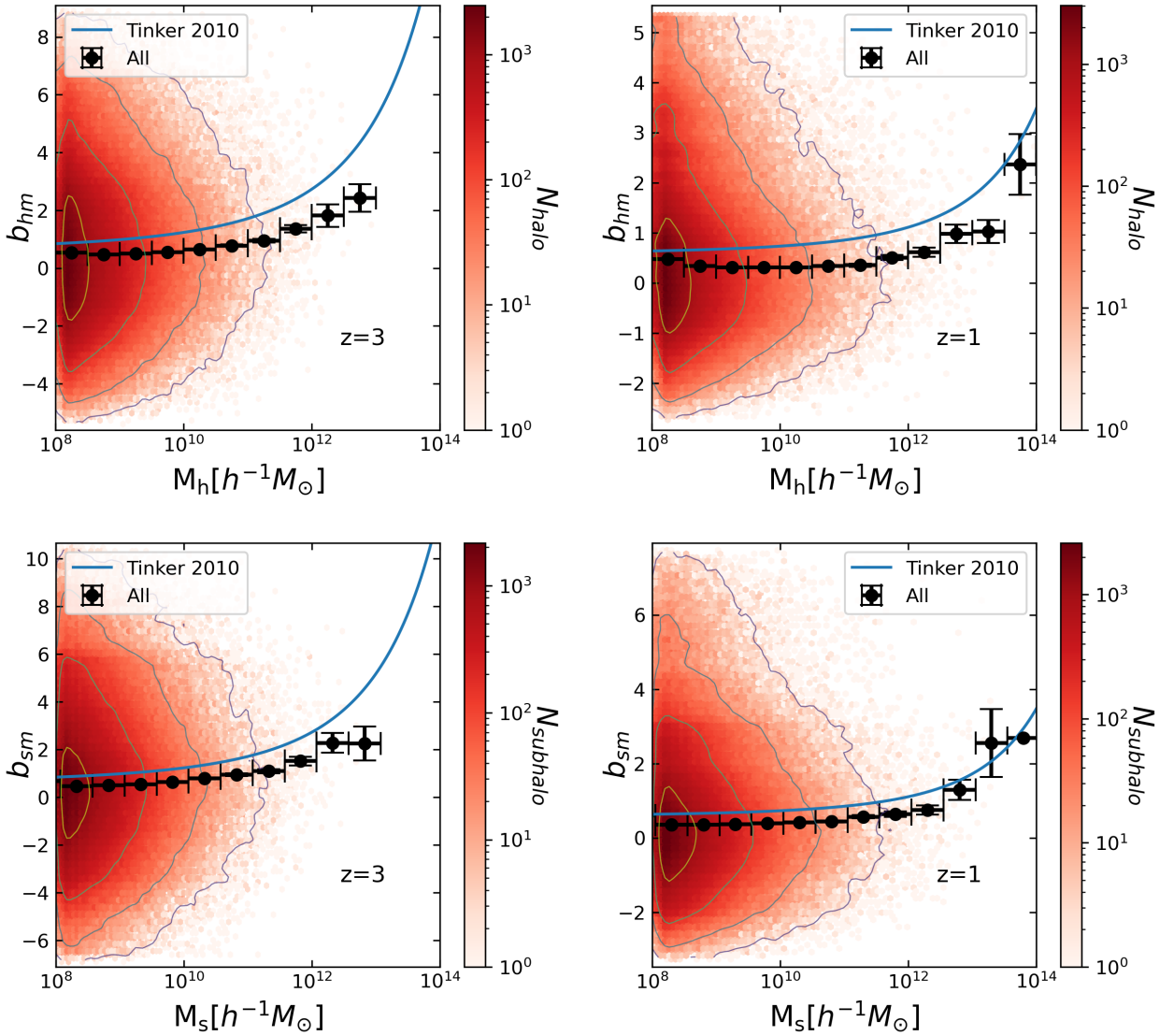los $\log N = [3.1, 2.3, 1.4, 0.5]$. Note that the plots at the two rows are shown at two redshifts, from left to right $z = 3$ and $z = 1$ ($z = 0$ is shown in Fig. 22)

5.2.   Secondary halo bias

The secondary halo bias is defined as the additional dependence of the spatial distribution of dark matter halos that cannot be explained by the mass of the halos alone. This additional bias is due to the internal properties of the halos or to the properties of the surroundings at a fixed mass (see e.g. for example, Balaguera-Antolínez et al., 2024; Montero-Dorta and Rodriguez, 2024, and references therein.). The secondary bias signal of the halos has been obtained by evaluating the mean value of the effective bias in each halo mass bin, where each bin has been divided into quartiles[9] of a secondary property (see e.g., Balaguera-Antolínez et al., 2024; Montero-Dorta and Rodriguez, 2024). In Fig. 26 we show the secondary halo bias in bins of halo mass using the local dark matter density as a secondary property. Up to $M_h \sim 10^{11} h^{-1} M_\odot$ the signal of secondary bias is dominated by the upper quartile, meaning that the halos that reside in denser regions tend to be more clustered. At $M_h \sim 10^{11} h^{-1} M_\odot$ we see a small secondary bias signal. From this mass onwards, at $z = 3$ the secondary bias signal is not as clear as the one that appeared at low masses. The secondary bias signal of massive halos at $z = 1$ and $z = 0$ is bigger than that at halos with $M_h \sim 10^{11} h^{-1} M_\odot$. At $z = 1$ the quartile that will have the highest clustering changes from one mass bin to

---

[9]Quartile is defined as a statistical concept that divides a set of ordered data into four equal parts. That is, quartiles are three values that divide a distribution into four equal parts and thus each part will have approximately 25% of the data (see e.g., Rohatgi and Saleh, 2015).
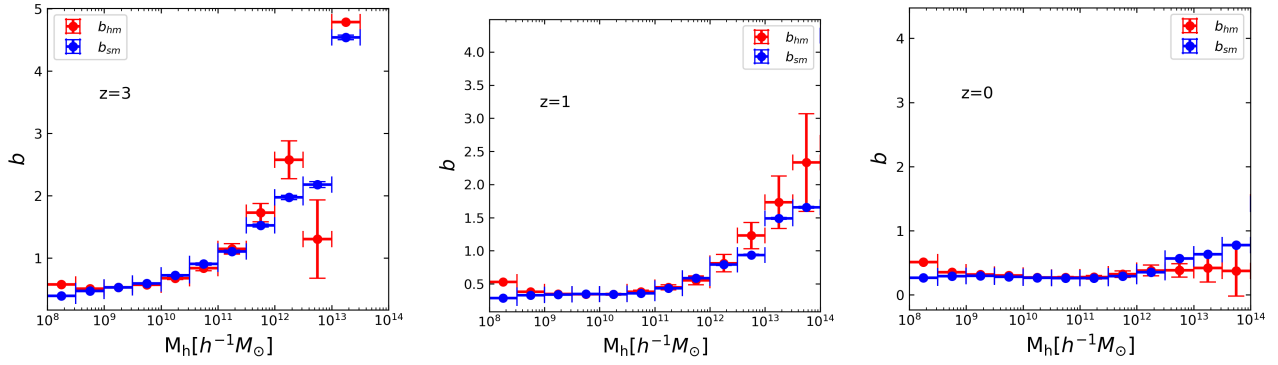
Figure 24: Comparison between the b_{hm} and the b_{sm} as a function of the halo mass. In order to make this comparison, the range of wavenumbers is equaled to $k \leq 0.3h\mathrm{Mpc}^{-1}$

another and at $z = 0$, we observe that throughout the range of massive halos, this signal of secondary bias is inverted, so the low density areas will be more clustered than the others. We also saw this in Fig. 25, where the halos living in filaments were more clustered than those living in knots.

5.3.   Secondary subhalo bias

Figure 27 shows the secondary bias of the subhalos. The properties we take to make the secondary bias are the ones we have been analyzing during the work, i.e., $V_{\max}$, σ_v, j and Z.

- *Maximum circular velocity*. The upper quartile of this property has more effective bias at subhalos with $M_s \leq 10^{12}h^{-1}M_\odot$ (except for the first bin). This secondary bias increases as the redshift decreases, which can be understood by the correlation coefficient seen in Tab. 1, which decreases with decreasing redshift. At higher subhalo masses this secondary bias becomes more pronounced, indicating that more massive subhaloes have higher scatter in the $V_{\max} - M_s$ relation. In Tab. 4 we have analyzed the correlation of subhalos living in the more massive halos, which is very small in this case. This is a good indicator of secondary bias but is not the definitive test. Finally at $z = 0$, in the last mass bin, there is an inversion, indicating that the subhalos having a lower $V_{\max}$, will be more clustered, compared to those having a higher $V_{\max}$.

- *Velocity dispersion*. We appreciate that there is a higher effective bias in those subhalos that have a higher σ_v up to $M_s \sim 10^{12}M_\odot$, where an inversion occurs. For all redshifts, the largest difference in terms of clustering between subhalos belonging to the upper and lower quartile is observed in the first and last mass bin. Comparing with $V_{\max}$, the information provided by the upper and lower quartiles is very similar in terms of clustering, which was predictable since both properties give us direct information about the depth of the potential well.

- *Spin*. At $z = 3$ for subhalos with $M_s \leq 10^{10}h^{-1}M_\odot$ the secondary bias signal is very small. From this mass onward, we begin to see that subhalos that have a higher j will have a higher effective bias. On the other hand, at $z = 1$ and $z = 0$, the secondary bias trend appears inverted, that is, the subhalos with a lower spin will be those that have a greater clustering. Comparing these last two redshifts, the difference between both quartiles is greater for $z = 0$. The spin does not provide a secondary bias signal as large as the two properties discussed above. This may be because this property is more correlated with M_s than the other two were (see Tab. 1).

- *Metallicity*. At $z = 3$, subhalos in masses between $M_s \sim 10^{8-9}h^{-1}M_\odot$ do not present a secondary bias with respect to Z. From this mass, the quartile that is most clustered changes as the mass bin changes. At the most massive subhalos, the effective bias signal will be higher in the lower quartile. Table 1 show that at these masses, the metallicity and mass of the subhalo are anticorrelated, i.e., $\rho < 0$. At $z = 1$, the subhalos have no secondary bias up to $M_s \sim 10^{10}h^{-1}M_\odot$. Here subhalos with higher Z will have higher effective bias. At $M_s \sim 10^{12}h^{-1}M_\odot$ the secondary bias signal is inverted, as seen at $z = 3$. At $z = 0$ there is no secondary bias up to subhalos of $M_s \sim 10^{10}h^{-1}M_\odot$. From this mass on, the secondary bias signal will be less than for $z = 1$.
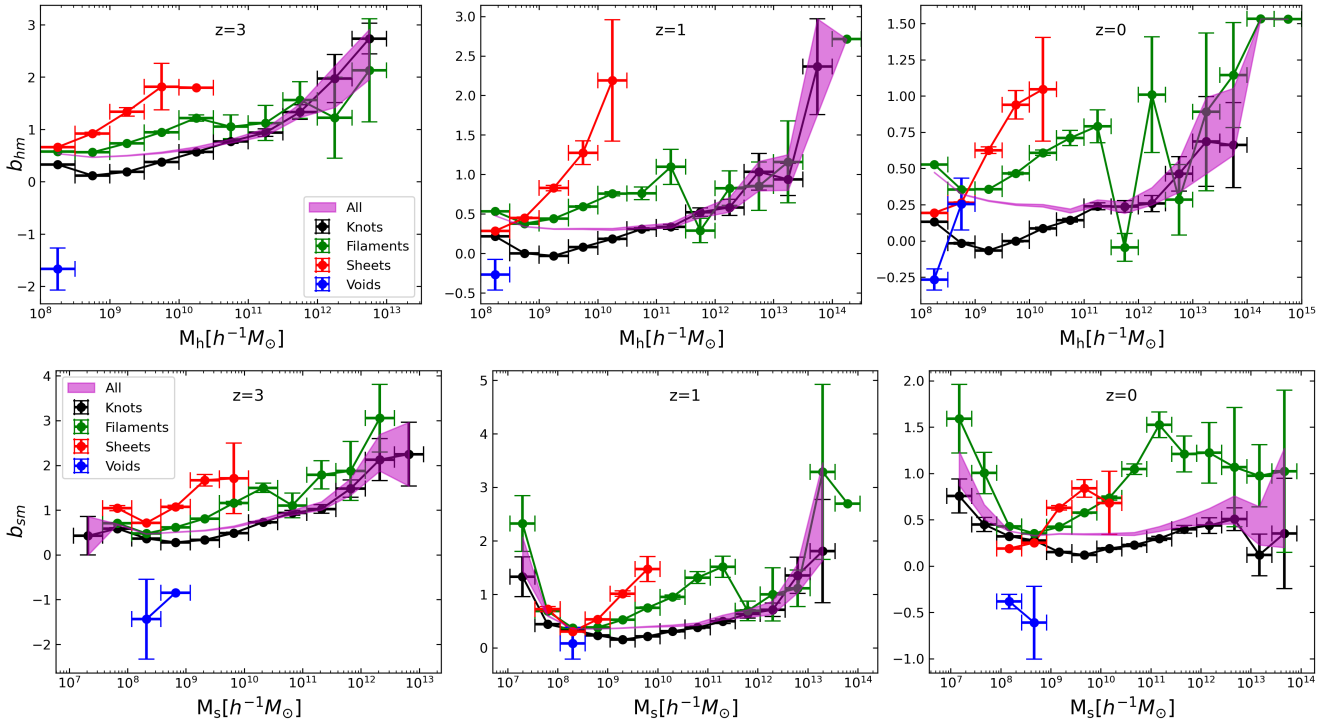
Figure 25: First row: Halo effective bias of TNG100 simulation with respect to the halo mass at the four cosmic-web environments showed in §4.2. Second row: Subhalo effective bias of TNG100 simulation with respect to the subhalo mass at the four cosmic-web environments showed in §4.2. Note that the plots at the two rows are showed at three different redshifts, from left to right $z = 3$, $z = 1$ and $z = 0$.

6. Conclusions

The connection between visible matter and the dark matter component contains cosmological information that deserves to be studied. In this work, we have used the IllustrisTNG-100 simulation to study this connection in different astrophysical and cosmological observables. In the first part of the work we have measured the scaling relations between subhalo properties as a function of halo and subhalo masses. We sum up the general analysis with the following points:

- The first-order scaling relations that can be predicted with a simple power law do not change the slope from one redshift to another while the amplitude does change. The MZ relation can be represented by a power law that saturates at high masses, in agreement with the works previously done.

- The first-order scaling relations that can be predicted with the virial theorem are in good agreement with the theoretical slope within the error bars. Despite this, the σ_v gives us a more accurate value to the theoretical ratio than the $V_{\max}$, so it will better characterize the potential well.

- $V_{\max}$ and σ_v will be less correlated with mass as we decrease the redshift, indicating that there will be more scatter. In the case of j, the opposite occurs, and for Z, there is no correlation at high masses and will have a correlation of $\rho \sim 0.5$ at low and intermediate masses.

- At all mass scales (except for the high-mass end) and redshifts, the scaling relation $P(\theta|M_s)$ (where θ are the subhalo properties) is not compatible with a Gaussian distribution. None of the second-order scaling relation is compatible with a normal distribution at any redshift and any mass scale.

- The $M_s - M_h$ relation saturates because the statistics of subhalos living high-intermediate mass halos is dominated by low-mass subhalos. We have fitted a quadratic function to this relation to check that this is the cause that the second-order scaling relations have a maximum.

- The scaling relations of the subhalo properties with respect to the halo mass, show that these properties are positively correlated at low masses for at all redshifts (except for the Z at $z = 0$), while are uncorrelated, i.e., $\rho \sim 0$ at mid-masses and high-masses.
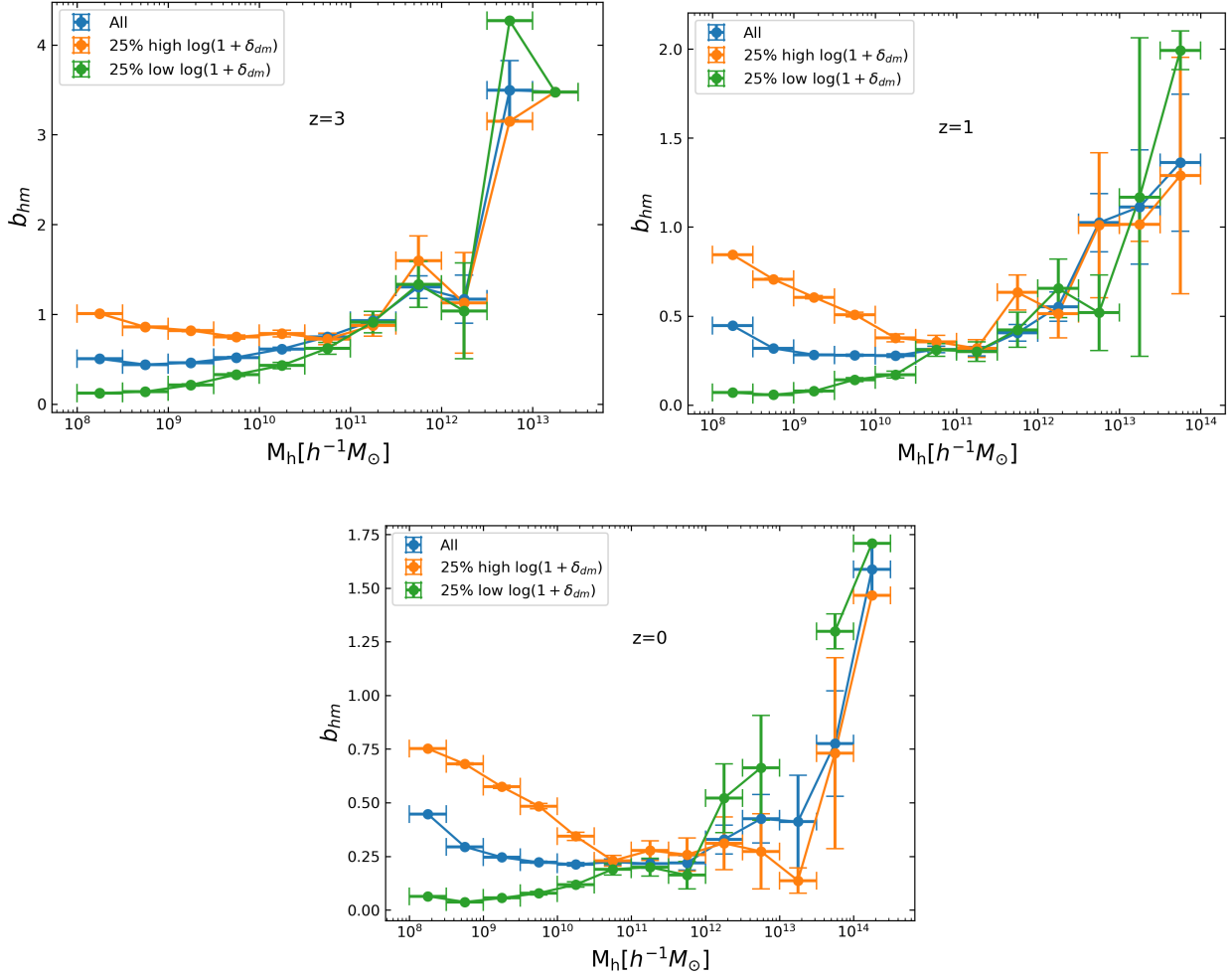
Figure 26: Secondary halo bias measured in bins of halo mass using the local dark matter density as a secondary property. In each mass-bin, the sample has been divided in quartiles of the property. We show the results from the lower (first) quartile (in green) and the upper (fourth) quartile (in orange), along with the results from the full sample (in blue), at three different redshifts, from left to right $z = 3$, $z = 1$ and $z = 0$.

- The scaling relations change when considering the subhalos living in halos with higher or lower masses. This is because the more massive halos have a higher probability of hosting more substructures, meaning that there are more tidal interactions between subhalos living in a same halo. These tidal forces cause both $V_{\max}$ and σ_v to be larger for subhalos living in more massive halos due to the extra acceleration these subhalos undergo, while causing angular momentum of the less massive subhalos to decrease because it is transferred to more massive subhalos.

At the second part of the work we constructed the dark matter density field, from where we measure the density distribution the power spectrum and the tidal tensor. The power spectrum match with the linear and non-linear predictions until the $\sim 60\%$ of the Nyquist frequency, where the corrections due to MAS aren't accurate anymore. We characterize the cosmic-web structures and analyze the halo abundance and the scaling relations in the different cosmic environments. From this analysis, we conclude:

- The cosmic-web environment also changes the scaling-relations. The subhalos living in halos that reside in filaments will have higher slopes in all the properties compared with the knots. The difference increases at low redshifts.

- The difference of the mean value of M_s with respect to M_h at the moment of saturation between knots and filaments decreases with decreasing redshift. The subhalos living in sheets show a trend that is similar to the one the filaments present at low masses.

- The second-order scaling relations change from one environment to another. The biggest difference between them for the $V_{\max}$ and σ_v is shown in $z = 3$ and for j is shown in $z = 0$. The biggest difference in the shape of the MZ relation from one environment to another is due to the density of these environments. The knots and filaments show a very similar shape between them, but in general, the sheets show lower values of Z. The voids have a negligible metallicity.
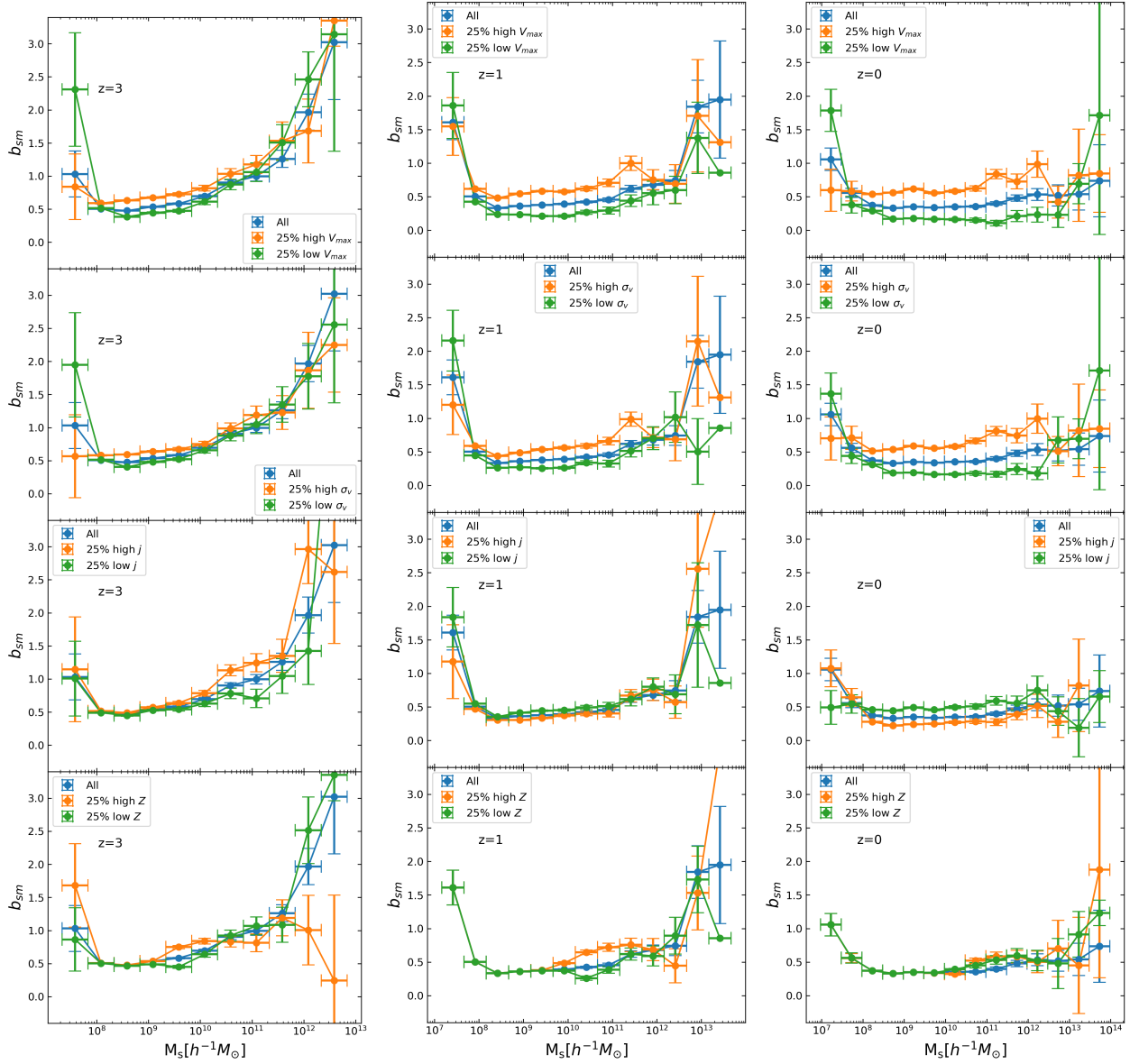
Figure 27: Secondary subhalo bias measured in bins of the subhalo mass using the subhalo properties as secondary properties, namely, from top to bottom: V_{max}, σ_v, j and Z. In each mass-bin, the sample has been divided in quartiles of the properties. We show the results from the lower (first) quartile (in green) and the upper (fourth) quartile (in orange), along with the results from the full sample (in blue), at three different redshifts, from left to right $z = 3$, $z = 1$ and $z = 0$.

At the last part of this master's thesis we have constructed an object-by-object estimator of large-scale linear bias, in order to analyze the large-scale structure of the dark matter, the halos and the subhalos in the TNG simulation. Finally, we have study the secondary halo and subhalo bias. The conclusions of this last part of the work are the following:

- We have measured the range of wavenumbers at which we can consider the large-scale effective bias by comparing the power spectrum of the halos and subhalos with the power spectrum of the dark matter. The ranges are $k \leq 0.3h\mathrm{Mpc}^{-1}$ for the subhalos and $k \leq 0.4h\mathrm{Mpc}^{-1}$ for halos.

- The mean values of the bias decreases with decreasing redshift, which is a consequence of the structure formation at different redshifts.

- Taking the same range of wavenumbers, the halos tend to be more biased than the subhalos, because, in general, the density peaks where these halos form were rarer than those where subhalos form.

- In terms of bias, is important to take into account the cosmic-web environment where the halos and subhalos live. In general, the most clustered halos up to $M_h \sim 10^{10}h^{-1}M_\odot$ are the ones that are located within the sheets. From that mass onward the halos living in filaments tend to be more clustered (except for the high-mass end in $z = 3$). For the

subhalos, the same happens, except for the low-mass end where the subhalos living in filaments are more clustered.

- The secondary bias signal appears when studying the evolution of bias in the upper and lower quartiles as a function of mass of a distribution, as reported numerous times in the literature.

- The halo bias show a secondary bias with respect to the dark matter density. This signal is clear at the low-mass end (where the halos living in a denser region are more clustered), reaches a minimum value at $M_h \sim 10^{11}h^{-1}M_\odot$ and show an inversion at the high-mass end. The evolution with redshift is reflected in the halo mass where the secondary bias inversion appears, which is smaller at low redshift ($M_h \sim 10^{12-12.5}h^{-1}M_\odot$ at $z = 0$) and increases with increasing redshift ($M_h \sim 10^{13}h^{-1}M_\odot$ at $z = 3$).

- The subhalo bias show a signal of secondary bias which increases with redshift (except for the Z). The properties that are related to the potential well of the subhalo present the highest secondary bias. The clustering in subhalos with a major angular momentum is the one with the most clustering for $z = 3$, but at $z = 1$ and $z = 0$ this trend is inverted. We don't appreciate secondary bias with the metallicity at low masses but from $M_s \sim 10^{10}h^{-1}M_\odot$ onwards a signal of secondary bias is induced, showing more clustering in the high quartile of Z. This trend is inverted at $M_s \sim 10^{12}h^{-1}M_\odot$. At $z = 1$ and $z = 0$, the most massive halos will be more clustered when Z is higher.

References

Abbott, T. M. C. and DES Collaboration (2020). Dark Energy Survey Year 1 Results: Cosmological constraints from cluster abundances and weak lensing. , 102(2):023509.

Appleby, S., Tonegawa, M., Park, C., Hong, S. E., Kim, J., and Yoon, Y. (2023). Cosmological Parameter Constraints from the SDSS Density and Momentum Power Spectra. , 958(2):180.

Aragón-Calvo, M. A., Van De Weygaert, R., and Jones, B. J. (2010). Multiscale phenomenology of the cosmic web. Monthly Notices of the Royal Astronomical Society, 408(4):2163–2187.

Arnett, D. (1996). Supernovae and nucleosynthesis: an investigation of the history of matter, from the big bang to the present, volume 7. Princeton University Press.

Ashby, N. (2003). Relativity in the Global Positioning System. Living Reviews in Relativity, 6(1):1.

Balaguera-Antolínez, A., Bilicki, M., Branchini, E., and Postiglione, A. (2018). Extracting cosmological information from the angular power spectrum of the 2mass photometric redshift catalogue. Monthly Notices of the Royal Astronomical Society, 476(1):1050–1070.

Balaguera-Antolínez, A., Montero-Dorta, A. D., and Favole, G. (2024). Secondary halo bias through cosmic time-i. scaling relations and the connection with the cosmic web. Astronomy & Astrophysics, 685:A61.

Balaguera-Antolinez, A., Sánchez, A. G., Böhringer, H., and Collins, C. (2012). Constructing mock catalogues for the reflex ii galaxy cluster sample. Monthly Notices of the Royal Astronomical Society, 425(3):2244–2254.

Balaguera-Antolinez, A (2024). Notes in cosmology. access through https://abalant.wixsite.com/abalan/publications.

Bardeen, J. M., Bond, J. R., Kaiser, N., and Szalay, A. S. (1986a). The statistics of peaks of Gaussian random fields. , 304:15–61.

Bardeen, J. M., Bond, J. R., Kaiser, N., and Szalay, A. S. (1986b). The Statistics of Peaks of Gaussian Random Fields. , 304:15.

Bartelmann, M. and Maturi, M. (2016). Weak gravitational lensing. arXiv preprint arXiv:1612.06535.

Basilakos, S., Plionis, M., and Ragone-Figueroa, C. (2008). The Halo Mass-Bias Redshift Evolution in the ΛCDM Cosmology. , 678(2):627–634.

Bennett, C. L., Larson, D., Weiland, J. L., Jarosik, N., Hinshaw, G., Odegard, N., Smith, K. M., Hill, R. S., Gold, B., Halpern, M., Komatsu, E., Nolta, M. R., Page, L., Spergel, D. N., Wollack, E., Dunkley, J., Kogut, A., Limon, M., Meyer, S. S., Tucker, G. S., and Wright, E. L. (2013). Nine-year Wilkinson Microwave Anisotropy Probe (WMAP) Observations: Final Maps and Results. , 208(2):20.

Binney, J. and Tremaine, S. (2011). Galactic dynamics, volume 13. Princeton university press.

Bond, J. R., Kofman, L., and Pogosyan, D. (1996). How filaments of galaxies are woven into the cosmic web. Nature, 380(6575):603–606.

Bose, S., Eisenstein, D. J., Hernquist, L., Pillepich, A., Nelson, D., Marinacci, F., Springel, V., and Vogelsberger, M. (2019). Revealing the galaxy–halo connection in illustristng. Monthly Notices of the Royal Astronomical Society, 490(4):5693–5711.

Branch, D. and Wheeler, J. C. (2017). Supernova explosions, volume 4. Springer.

Bryan, G. L. and Norman, M. L. (1998). Statistical properties of x-ray clusters: Analytic and numerical comparisons. The Astrophysical Journal, 495(1):80.

Cepa, J. (2007). Cosmología física. Ediciones Akal.

Ciotti, L. (2021). Introduction to Stellar Dynamics. Cambridge University Press.

Cole, S., Percival, W. J., Peacock, J. A., Norberg, P., Baugh, C. M., Frenk, C. S., Baldry, I., Bland-Hawthorn, J., Bridges, T., Cannon, R., et al. (2005). The 2df galaxy redshift survey: power-spectrum analysis of the final data set and cosmological implications. Monthly Notices of the Royal Astronomical Society, 362(2):505–534.

Contreras, S., Angulo, R., and Zennaro, M. (2021). A flexible modelling of galaxy assembly bias. Monthly Notices of the Royal Astronomical Society, 504(4):5205–5220.

Cooray, A. and Sheth, R. (2002). Halo models of large scale structure. Phys. Rep., 372:1–129.

Cramér, H. (1999). Mathematical methods of statistics, volume 26. Princeton university press.

Cui, W. et al. (2008). An ideal mass assignment scheme for measuring the power spectrum with ffts apj, 687: p. 738. arXiv preprint arXiv:0804.0070.

Dalal, N., White, M., Bond, J. R., and Shirokov, A. (2008). Halo assembly bias in hierarchical structure formation. The Astrophysical Journal, 687(1):12.

Davis, M., Efstathiou, G., Frenk, C. S., and White, S. D. (1985). The evolution of large-scale structure in a universe dominated by cold dark matter. Astrophysical Journal, Part 1 (ISSN 0004-637X), vol. 292, May 15, 1985, p. 371-394. Research supported by the Science and Engineering Research Council of England and NASA., 292:371–394.

Dawson, K. S. e. a. (2016). The SDSS-IV Extended Baryon Oscillation Spectroscopic Survey: Overview and Early Data. , 151(2):44.

Dekel, A. and Lahav, O. (1999). Stochastic nonlinear galaxy biasing. The Astrophysical Journal, 520(1):24.

Demir, S. (2022). Comparison of normality tests in terms of sample sizes under different skewness and kurtosis coefficients. International Journal of Assessment Tools in Education, 9(2):397–409.

DESI Collaboration (2024). DESI 2024 VI: Cosmological Constraints from the Measurements of Baryon Acoustic Oscillations. arXiv e-prints, page arXiv:2404.03002.

Desjacques, V., Jeong, D., and Schmidt, F. (2018). Large-scale galaxy bias. Physics reports, 733:1–193.

Dodelson, S. (2003). Modern Cosmology. Elsevier Science.

Dodelson, S. (2017). Gravitational lensing. Cambridge University Press.

Dolag, K., Borgani, S., Murante, G., and Springel, V. (2009). Substructures in hydrodynamical cluster simulations. Monthly Notices of the Royal Astronomical Society, 399(2):497–514.

Eddington, A. S. (1919). The total eclipse of 1919 May 29 and the influence of gravitation on light. The Observatory, 42:119–122.

Einstein, A. (1915). Erklärung der Perihelbewegung des Merkur aus der allgemeinen Relativitätstheorie. Sitzungsberichte der Königlich Preussischen Akademie der Wissenschaften, pages 831–839.

Eisenstein, D. J. and Hu, W. (1999). Power spectra for cold dark matter and its variants. The Astrophysical Journal, 511(1):5.

Engler, C., Pillepich, A., Joshi, G. D., Nelson, D., Pasquali, A., Grebel, E. K., Lisker, T., Zinger, E., Donnari, M., Marinacci, F., et al. (2021). The distinct stellar-to-halo mass relations of satellite and central galaxies: insights from the illustristng simulations. Monthly Notices of the Royal Astronomical Society, 500(3):3957–3975.

Euclid Collaboration, Blanchard, A., Camera, S., Carbone, C., Cardone, V. F., Casas, S., Clesse, S., Ilić, S., Kilbinger, M., Kitching, T., Kunz, M., Lacasa, F., Linder, E., Majerotto, E., Markovič, K., Martinelli, M., Pettorino, V., Pourtsidou, A., Sakr, Z., Sánchez, A. G., Sapone, D., Tutusaus, I., Yahia-Cherif, S., Yankelevich, V., Andreon, S., Aussel, H., Balaguera-Antolínez, A., Baldi, M., Bardelli, S., Bender, R., Biviano, A., Bonino, D., Boucaud, A., Bozzo, E., Branchini, E., Brau-Nogue, S., Brescia, M., Brinchmann, J., Burigana, C., Cabanac, R., Capobianco, V., Cappi, A., Carretero, J., Carvalho, C. S., Casas, R., Castander, F. J., Castellano, M., Cavuoti, S., Cimatti, A., Cledassou, R., Colodro-Conde, C., Congedo, G., Conselice, C. J., Conversi, L., Copin, Y., Corcione, L., Coupon, J., Courtois, H. M., Cropper, M., Da Silva, A., de la Torre, S., Di Ferdinando, D., Dubath, F., Ducret, F., Duncan, C. A. J., Dupac, X., Dusini, S., Fabbian, G., Fabricius, M., Farrens, S., Fosalba, P., Fotopoulou, S., Fourmanoit, N., Frailis, M., Franceschi, E., Franzetti, P., Fumana, M., Galeotta, S., Gillard, W., Gillis, B., Giocoli, C., Gómez-Alvarez, P., Graciá-Carpio, J., Grupp, F., Guzzo, L., Hoekstra, H., Hormuth, F., Israel, H., Jahnke, K., Keihanen, E., Kermiche, S., Kirkpatrick, C. C., Kohley, R., Kubik, B., Kurki-Suonio, H., Ligori, S., Lilje, P. B., Lloro, I., Maino, D., Maiorano, E., Marggraf, O., Martinet, N., Marulli, F., Massey, R., Medinaceli, E., Mei, S., Mellier, Y., Metcalf, B., Metge, J. J., Meylan, G., Moresco, M., Moscardini, L., Munari, E., Nichol, R. C., Niemi, S., Nucita, A. A., Padilla, C., Paltani, S., Pasian, F., Percival, W. J., Pires, S., Polenta, G., Poncet, M., Pozzetti, L., Racca, G. D., Raison, F., Renzi, A., Rhodes, J., Romelli, E., Roncarelli, M., Rossetti, E., Saglia, R., Schneider, P., Scottez, V., Secroun, A., Sirri, G., Stanco, L., Starck, J. L., Sureau, F., Tallada-Crespí, P., Tavagnacco, D., Taylor, A. N., Tenti, M., Tereno, I., Toledo-Moreo, R., Torradeflot, F., Valenziano, L., Vassallo, T., Verdoes Kleijn, G. A., Viel, M., Wang, Y., Zacchei, A., Zoubian, J., and Zucca, E. (2020). Euclid preparation. VII. Forecast validation for Euclid cosmological probes. , 642:A191.

Favole, G., Montero-Dorta, A. D., Artale, M. C., Contreras, S., Zehavi, I., and Xu, X. (2022). Subhalo abundance matching through the lens of a hydrodynamical simulation. Monthly Notices of the Royal Astronomical Society, 509(2):1614–1625.

Feldman, H. A., Kaiser, N., and Peacock, J. A. (1994). Power-spectrum analysis of three-dimensional redshift surveys. , 426:23–37.

Fixsen, D. and Mather, J. (2002). The spectral results of the far-infrared absolute spectrophotometer instrument on cobe. The Astrophysical Journal, 581(2):817.

Fixsen, D. J., Cheng, E. S., Gales, J. M., Mather, J. C., Shafer, R. A., and Wright, E. L. (1996). The Cosmic Microwave Background Spectrum from the Full COBE FIRAS Data Set. , 473:576.

Fumagalli, A., Costanzi, M., Saro, A., Castro, T., and Borgani, S. (2024). Cosmological constraints from the abundance, weak lensing, and clustering of galaxy clusters: Application to the sdss. Astronomy & Astrophysics, 682:A148.

Gao, L., Springel, V., and White, S. D. (2005). The age dependence of halo clustering. Monthly Notices of the Royal Astronomical Society: Letters, 363(1):L66–L70.

Genel, S., Vogelsberger, M., Springel, V., Sijacki, D., Nelson, D., Snyder, G., Rodriguez-Gomez, V., Torrey, P., and Hernquist, L. (2014). Introducing the illustris project: the evolution of galaxy populations across cosmic time. Monthly Notices of the Royal Astronomical Society, 445(1):175–200.

González, R. E. and Padilla, N. D. (2010). Automated detection of filaments in the large-scale structure of the universe. Monthly Notices of the Royal Astronomical Society, 407(3):1449–1463.

Gunn, J. E. and Gott, J. Richard, I. (1972). On the Infall of Matter Into Clusters of Galaxies and Some Effects on Their Evolution. , 176:1.

Hadzhiyska, B., Bose, S., Eisenstein, D., and Hernquist, L. (2021). Extensions to models of the galaxy–halo connection. Monthly Notices of the Royal Astronomical Society, 501(2):1603–1620.

Hadzhiyska, B., Bose, S., Eisenstein, D., Hernquist, L., and Spergel, D. N. (2020). Limitations to the 'basic'hod model and beyond. Monthly Notices of the Royal Astronomical Society, 493(4):5506–5519.

Hahn, O., Porciani, C., Carollo, C. M., and Dekel, A. (2007). Properties of dark matter haloes in clusters, filaments, sheets and voids. Monthly Notices of the Royal Astronomical Society, 375(2):489–499.

Hahn, O., Porciani, C., Dekel, A., and Carollo, C. M. (2009). Tidal effects and the environment dependence of halo assembly. Monthly Notices of the Royal Astronomical Society, 398(4):1742–1756.

Heath, D. (1977). The growth of density perturbations in zero pressure friedmann–lemaître universes. Monthly Notices of the Royal Astronomical Society, 179(3):351–358.

Heavens, A. and Peacock, J. (1988). Tidal torques and local density maxima. Monthly Notices of the Royal Astronomical Society, 232(2):339–360.

Hockney, R. W. and Eastwood, J. W. (1988). Computer simulation using particles. Bristol: Hilger, 1988.

Ivanov, M. M., Simonović, M., and Zaldarriaga, M. (2020). Cosmological parameters from the BOSS galaxy power spectrum. , 2020(5):042.

Kaiser, N. (1987). Clustering in real space and in redshift space. , 227:1–21.

Kilbinger, M. (2015). Cosmology with cosmic shear observations: a review. Reports on Progress in Physics, 78(8):086901.

Lahav, O. (2002). The 2dF Galaxy Redshift Survey: Cosmological Parameters and Galaxy Biasing. In Sato, K. and Shiromizu, T., editors, New Trends in Theoretical and Observational Cosmology, page 145.

Lequeux, J., Peimbert, M., Rayo, J., Serrano, A., and Torres-Peimbert, S. (1979). Chemical composition and evolution of irregular and blue compact galaxies. Astronomy and Astrophysics, vol. 80, no. 2, Dec. 1979, p. 155-166., 80:155–166.

Lesci, G., Marulli, F., Moscardini, L., Sereno, M., Veropalumbo, A., Maturi, M., Giocoli, C., Radovich, M., Bellagamba, F., Roncarelli, M., et al. (2022). Amico galaxy clusters in kids-dr3: Cosmological constraints from counts and stacked weak lensing. Astronomy & Astrophysics, 659:A88.

Libeskind, N. I., Van De Weygaert, R., Cautun, M., Falck, B., Tempel, E., Abel, T., Alpaslan, M., Aragón-Calvo, M. A., Forero-Romero, J. E., Gonzalez, R., et al. (2018). Tracing the cosmic web. Monthly Notices of the Royal Astronomical Society, 473(1):1195–1217.

Marinacci, F., Vogelsberger, M., Pakmor, R., Torrey, P., Springel, V., Hernquist, L., Nelson, D., Weinberger, R., Pillepich, A., Naiman, J., et al. (2018). First results from the illustristng simulations: radio haloes and magnetic fields. Monthly Notices of the Royal Astronomical Society, 480(4):5113–5139.

Martizzi, D., Vogelsberger, M., Artale, M. C., Haider, M., Torrey, P., Marinacci, F., Nelson, D., Pillepich, A., Weinberger, R., Hernquist, L., Naiman, J., and Springel, V. (2019). Baryons in the Cosmic Web of IllustrisTNG - I: gas in knots, filaments, sheets, and voids. , 486(3):3766–3787.

Martizzi, D., Vogelsberger, M., Torrey, P., Pillepich, A., Hansen, S. H., Marinacci, F., and Hernquist, L. (2020). Baryons in the Cosmic Web of IllustrisTNG - II. The connection among galaxies, haloes, their formation time, and their location in the Cosmic Web. , 491(4):5747–5758.

Mitra, P., Murthy, C., and Pal, S. K. (2002). Unsupervised feature selection using feature similarity. IEEE transactions on pattern analysis and machine intelligence, 24(3):301–312.

Mo, H., Van den Bosch, F., and White, S. (2010). Galaxy formation and evolution. Cambridge University Press.

Molugaram, K., Rao, G. S., Shah, A., and Davergave, N. (2017). Statistical techniques for transportation engineering. Butterworth-Heinemann.

Montero-Dorta, A. D., Artale, M. C., Abramo, L. R., and Tucci, B. (2021a). On the kinetic sunyaev–zel'dovich effect as an observational probe for halo spin bias. Monthly Notices of the Royal Astronomical Society, 504(3):4568–4582.

Montero-Dorta, A. D., Artale, M. C., Abramo, L. R., Tucci, B., Padilla, N., Sato-Polito, G., Lacerna, I., Rodriguez, F., and Angulo, R. E. (2020). The manifestation of secondary bias on the galaxy population from illustristng300. Monthly Notices of the Royal Astronomical Society, 496(2):1182–1196.

Montero-Dorta, A. D., Chaves-Montero, J., Artale, M. C., and Favole, G. (2021b). On the influence of halo mass accretion history on galaxy properties and assembly bias. Monthly Notices of the Royal Astronomical Society, 508(1):940–949.

Montero-Dorta, A. D. and Rodriguez, F. (2024). The dependence of assembly bias on the cosmic web. Monthly Notices of the Royal Astronomical Society, 531(1):290–303.

Montero-Dorta, A. D., Rodriguez, F., Artale, M. C., Smith, R., and Chaves-Montero, J. (2024). Tracking the evolution of satellite galaxies: mass stripping and dark-matter deficient galaxies. Monthly Notices of the Royal Astronomical Society, 527(3):5868–5885.

Naiman, J. P., Pillepich, A., Springel, V., Ramirez-Ruiz, E., Torrey, P., Vogelsberger, M., Pakmor, R., Nelson, D., Marinacci, F., Hernquist, L., et al. (2018). First results from the illustristng simulations: A tale of two elements–chemical evolution of magnesium and europium. Monthly Notices of the Royal Astronomical Society, 477(1):1206–1224.

Nelson, D., Pillepich, A., Springel, V., Weinberger, R., Hernquist, L., Pakmor, R., Genel, S., Torrey, P., Vogelsberger, M., Kauffmann, G., et al. (2018). First results from the illustristng simulations: the galaxy colour bimodality. Monthly Notices of the Royal Astronomical Society, 475(1):624–647.

Padmanabhan, T. (1993). Structure formation in the universe. Cambridge university press.

Paranjape, A., Hahn, O., and Sheth, R. K. (2018). Halo assembly bias and the tidal anisotropy of the local halo environment. Monthly Notices of the Royal Astronomical Society, 476(3):3631–3647.

Paranjape, A. and Sheth, R. K. (2012). Peaks theory and the excursion set approach. Monthly Notices of the Royal Astronomical Society, 426(4):2789–2796.

Peacock, J. A. (1998). Cosmological physics. Cambridge university press.

Peebles, P. J. E. (1980). The large-scale structure of the universe, volume 12. Princeton university press.

Peebles, P. J. E. (1993). Principles of physical cosmology, volume 27. Princeton university press.

Penzias, A. A. and Wilson, R. W. (1965). A measurement of excess antenna temperature at 4080 mhz. In A Source Book in Astronomy and Astrophysics, 1900–1975, pages 873–876. Harvard University Press.

Percival, W. J. (2005). Cosmological structure formation in a homogeneous dark energy background. , 443(3):819–830.

Perlmutter, S., Aldering, G., Goldhaber, G., Knop, R. A., Nugent, P., Castro, P. G., Deustua, S., Fabbro, S., Goobar, A., Groom, D. E., Hook, I. M., Kim, A. G., Kim, M. Y., Lee, J. C., Nunes, N. J., Pain, R., Pennypacker, C. R., Quimby, R., Lidman, C., Ellis, R. S., Irwin, M., McMahon, R. G., Ruiz-Lapuente, P., Walton, N., Schaefer, B., Boyle, B. J., Filippenko, A. V., Matheson, T., Fruchter, A. S., Panagia, N., Newberg, H. J. M., Couch, W. J., and Project, T. S. C. (1999). Measurements of Ω and Λ from 42 High-Redshift Supernovae. , 517(2):565–586.

Pillepich, A., Springel, V., Nelson, D., Genel, S., Naiman, J., Pakmor, R., Hernquist, L., Torrey, P., Vogelsberger, M., Weinberger, R., et al. (2018). Simulating galaxy formation with the illustristng model. Monthly Notices of the Royal Astronomical Society, 473(3):4077–4106.

Planck Collaboration (2016a). Planck 2015 results. XIII. Cosmological parameters. , 594:A13.

Planck Collaboration (2016b). Planck 2015 results. XXVII. The second Planck catalogue of Sunyaev-Zeldovich sources. , 594:A27.

Pollack, J. E., Smith, R. E., and Porciani, C. (2012). Modelling large-scale halo bias using the bispectrum. , 420(4):3469–3489.

Porciani, C., Dekel, A., and Hoffman, Y. (2002). Testing tidal-torque theory - II. Alignment of inertia and shear and the characteristics of protohaloes. , 332(2):339–351.

Press, W. H. and Schechter, P. (1974). Formation of galaxies and clusters of galaxies by self-similar gravitational condensation. Astrophysical Journal, Vol. 187, pp. 425-438 (1974), 187:425–438.

Ramakrishnan, S., Paranjape, A., Hahn, O., and Sheth, R. K. (2019). Cosmic web anisotropy is the primary indicator of halo assembly bias. Monthly Notices of the Royal Astronomical Society, 489(3):2977–2996.

Riess, A. G., Filippenko, A. V., Challis, P., Clocchiatti, A., Diercks, A., Garnavich, P. M., Gilliland, R. L., Hogan, C. J., Jha, S., Kirshner, R. P., Leibundgut, B., Phillips, M. M., Reiss, D., Schmidt, B. P., Schommer, R. A., Smith, R. C., Spyromilio, J., Stubbs, C., Suntzeff, N. B., and Tonry, J. (1998). Observational Evidence from Supernovae for an Accelerating Universe and a Cosmological Constant. , 116(3):1009–1038.

Rindler, W. (1977). Essential Relativity: Special, General, and Cosmological. Texts and monographs in physics. Van Nostrand Reinhold Company.

Rohatgi, V. K. and Saleh, A. M. E. (2015). An introduction to probability and statistics. John Wiley & Sons.

Ryden, B. (2017). Introduction to cosmology. Cambridge University Press.

Sánchez, A. G., Crocce, M., Cabré, A., Baugh, C. M., and Gaztañaga, E. (2009). Cosmological parameter constraints from SDSS luminous red galaxies: a new treatment of large-scale clustering. , 400(3):1643–1664.

Schaap, W. and Van De Weygaert, R. (2000). Continuous fields and discrete samples: reconstruction through delaunay tessellations. arXiv preprint astro-ph/0011007.

Shankar, F., Lapi, A., Salucci, P., De Zotti, G., and Danese, L. (2006). New relationships between galaxy properties and host halo mass, and the role of feedbacks in galaxy formation. The Astrophysical Journal, 643(1):14.

Sheth, R. K. and Tormen, G. (1999). Large-scale bias and the peak background split. Monthly Notices of the Royal Astronomical Society, 308(1):119–126.

Shi, J., Wang, H., Mo, H., Vogelsberger, M., Ho, L. C., Du, M., Nelson, D., Pillepich, A., and Hernquist, L. (2020). The formation history of subhalos and the evolution of satellite galaxies. The Astrophysical Journal, 893(2):139.

Smith, R. E., Scoccimarro, R., and Sheth, R. K. (2007). Scale dependence of halo and galaxy bias: Effects in real space. Physical Review D—Particles, Fields, Gravitation, and Cosmology, 75(6):063512.

Smoot, G. F., Bennett, C. L., Kogut, A., Wright, E., Aymon, J., Boggess, N., Cheng, E., De Amici, G., Gulkis, S., Hauser, M., et al. (1992). Structure in the cobe differential microwave radiometer first-year maps. Astrophysical Journal, Part 2-Letters (ISSN 0004-637X), vol. 396, no. 1, Sept. 1, 1992, p. L1-L5. Research supported by NASA., 396:L1–L5.

Sousbie, T., Pichon, C., and Kawahara, H. (2011). The persistent cosmic web and its filamentary structure–ii. illustrations. Monthly Notices of the Royal Astronomical Society, 414(1):384–403.

Springel, V. (2010). E pur si muove: Galilean-invariant cosmological hydrodynamical simulations on a moving mesh. Monthly Notices of the Royal Astronomical Society, 401(2):791–851.

Springel, V., Pakmor, R., Pillepich, A., Weinberger, R., Nelson, D., Hernquist, L., Vogelsberger, M., Genel, S., Torrey, P., Marinacci, F., et al. (2018). First results from the illustristng simulations: matter and galaxy clustering. Monthly Notices of the Royal Astronomical Society, 475(1):676–698.

Springel, V., White, S. D., Jenkins, A., Frenk, C. S., Yoshida, N., Gao, L., Navarro, J., Thacker, R., Croton, D., Helly, J., et al. (2005). Simulations of the formation, evolution and clustering of galaxies and quasars. nature, 435(7042):629–636.

Springel, V., White, S. D., Tormen, G., and Kauffmann, G. (2001). Populating a cluster of galaxies–i. results at z= 0. Monthly Notices of the Royal Astronomical Society, 328(3):726–750.

Takahashi, R., Sato, M., Nishimichi, T., Taruya, A., and Oguri, M. (2012). Revising the halofit model for the nonlinear matter power spectrum. The Astrophysical Journal, 761(2):152.

Tegmark, M., Hamilton, A. J. S., Strauss, M. A., Vogeley, M. S., and Szalay, A. S. (1998). Measuring the Galaxy Power Spectrum with Future Redshift Surveys. , 499(2):555–576.

Tinker, J., Kravtsov, A. V., Klypin, A., Abazajian, K., Warren, M., Yepes, G., Gottlöber, S., and Holz, D. E. (2008). Toward a halo mass function for precision cosmology: The limits of universality. The Astrophysical Journal, 688(2):709.

Tinker, J. L., Robertson, B. E., Kravtsov, A. V., Klypin, A., Warren, M. S., Yepes, G., and Gottlöber, S. (2010). The Large-scale Bias of Dark Matter Halos: Numerical Calibration and Model Tests. , 724(2):878–886.

Tremonti, C. A., Heckman, T. M., Kauffmann, G., Brinchmann, J., Charlot, S., White, S. D., Seibert, M., Peng, E. W., Schlegel, D. J., Uomoto, A., et al. (2004). The origin of the mass-metallicity relation: insights from 53,000 star-forming galaxies in the sloan digital sky survey. The Astrophysical Journal, 613(2):898.

Tutukov, A., Shustov, B., and Wiebe, D. (2000). The stellar epoch in the evolution of the galaxy. Astronomy Reports, 44:711–718.

Vogelsberger, M., Genel, S., Springel, V., Torrey, P., Sijacki, D., Xu, D., Snyder, G., Bird, S., Nelson, D., and Hernquist, L. (2014a). Properties of galaxies reproduced by a hydrodynamic simulation. Nature, 509(7499):177–182.

Vogelsberger, M., Genel, S., Springel, V., Torrey, P., Sijacki, D., Xu, D., Snyder, G., Nelson, D., and Hernquist, L. (2014b). Introducing the illustris project: simulating the coevolution of dark and visible matter in the universe. Monthly Notices of the Royal Astronomical Society, 444(2):1518–1547.

Watson, W. A., Iliev, I. T., D'Aloisio, A., Knebe, A., Shapiro, P. R., and Yepes, G. (2013). The halo mass function through the cosmic ages. Monthly Notices of the Royal Astronomical Society, 433(2):1230–1245.

Wechsler, R. H. and Tinker, J. L. (2018). The connection between galaxies and their dark matter halos. Annual Review of Astronomy and Astrophysics, 56:435–487.

Weinberg, S. (1972). Gravitation and cosmology: principles and applications of the general theory of relativity.

Weinberger, R., Springel, V., Hernquist, L., Pillepich, A., Marinacci, F., Pakmor, R., Nelson, D., Genel, S., Vogelsberger, M., Naiman, J., et al. (2016). Simulating galaxy formation with black hole driven thermal and kinetic feedback. Monthly Notices of the Royal Astronomical Society, 465(3):3291–3308.

White, M., Scott, D., and Silk, J. (1994). Anisotropies in the cosmic microwave background. Annual Review of Astronomy and Astrophysics, 32(1):319–370.

Zahid, H. J., Dima, G. I., Kudritzki, R.-P., Kewley, L. J., Geller, M. J., Hwang, H. S., Silverman, J. D., and Kashino, D. (2014). The universal relation of galactic chemical evolution: the origin of the mass–metallicity relation. The Astrophysical Journal, 791(2):130.

Zahid, H. J., Geller, M. J., Kewley, L. J., Hwang, H. S., Fabricant, D. G., and Kurtz, M. J. (2013). The chemical evolution of star-forming galaxies over the last 11 billion years. The Astrophysical Journal Letters, 771(2):L19.

Zahid, H. J., Hwang, H. S., and Geller, M. J. (2017). The dependence of the mass–metallicity relation on large-scale environment. Monthly Notices of the Royal Astronomical Society, 468(2):1881–1892.

Zel'Dovich, Y. B. (1970). Gravitational instability: An approximate theory for large density perturbations. Astronomy and Astrophysics, Vol. 5, p. 84-89, 5:84–89.

A.   Moments of the scaling relations

In this second part of the section, we will show how the scaling relations and their moments have been measured. First, let us define the moments derived from the scaling relations that we are going to calculate in this work. Note that we have distributed the whole sample into mass bins, either subhalo (first-order) or halo (second-order), so that the different moments of the distribution have been calculated within the sample of n objects falling into each mass bin.

The first two moments of a distribution are the mean and the variance. For a discrete data set as the one provided by the simulation, we compute these as sums over the tracers $\bar{x} = \sum_{i=1}^{n} x_i/n$, and $s^2 = \sum_{i=1}^{n} (x_i - \bar{x})^2/(n-1)$. A low variance indicates that the values are, in general, very close to the mean. A large variance indicates the opposite. If the distribution were Gaussian, these two moments would be sufficient to describe it, since the higher moments are zero (Peebles, 1980). However, we will verify that many of the scaling relationships follow a non-Gaussian distribution. Therefore, it is necessary to obtain the higher moments to achieve a complete description of the distribution.

The skewness is a measure of asymmetry of the probability distribution of a real-valued random variable around its mean, and it's calculates following Cramér (1999) as:

$$\gamma_1 = \frac{\frac{1}{n}\sum_{i=1}^{n}(x_i - \bar{x})^3}{s^3}, \tag{30}$$

where negative skewness indicates that the tail is on the left side of the distribution, and positive skewness indicates that the tail is on the right. If the skewness is zero, we can consider the distribution to be symmetric about its mean value.

On the other hand, kurtosis is a measure of the "tailedness" of the probability distribution of a real-valued random variable. For this measure, higher kurtosis corresponds to a sharper peak. It is usual to compare the kurtosis value with that of the normal distribution by subtracting the kurtosis value of the normal distribution, which is 3, from the kurtosis value of the distribution we are analyzing. We obtain the value of the kurtosis following Cramér (1999) as:

$$\gamma_2 = \frac{\frac{1}{n}\sum_{i=1}^{n}(x_i - \bar{x})^4}{s^2} - 3. \tag{31}$$

Here what we will have is that for a positive kurtosis, sharper peaks (named leptokurtic) and for a negative kurtosis, flatter peaks (named platykurtic). In this work, to calculate skewness and kurtosis, a continuous normal random variable was derived with the mean and standard deviation defined within each mass bin. This variable has been compared with the histogram defined within each mass bin using the mean value theorem defined for a property θ as $f(\theta^i) = (\Delta\theta)^{-1}\int_{\Delta\theta} f(\theta)\,d\theta$ where $\Delta\theta$ is the bin width and $f(\theta^i)$ is the distribution function at the i-th bin of mass. Standard errors for the skewness and the kurtosis are calculated using the following (Demir, 2022):

$$\sigma_{\text{Skew}} = \sqrt{\frac{6n(n-1)}{(n-2)(n+1)(n+3)}} \tag{32}$$

$$\sigma_{\text{Kurt}} = 2\sigma_{\text{Skew}}\sqrt{\frac{n^2-1}{(n-3)(n-5)}}, \tag{33}$$

where n is the number of objects taken into account for calculating the skewness and the kurtosis. With this, we will be able to determine if the scale relations can be defined by a Gaussian distribution or not, since if the value of skewness and kurtosis (including its error) are 0 the distribution can be considered as a Gaussian distribution.

On the other hand, in the tables of the scaling relations of this work (see e.g., Tab. 1), we have shown correlation coefficients that we have calculated using Pearson's correlation coefficient defined as follows

$$\rho_{XY} = \frac{\sigma_{X,Y}}{\sigma_X \sigma_Y} \tag{34}$$

where σ_X and σ_Y are the standard deviations of the variables and the $\sigma_{X,Y}$ is the covariance of two variables defined as $\sigma_{X,Y} = (1/n)\sum_i^n (X_i - \bar{X})(Y_i - \bar{Y})$. With the correlation coefficient is an indicator of scatter of one property with respect to the other (see e.g., Mitra et al., 2002). In our work we have used `np.corrcoef` to generate the correlation coefficient matrix. Correlation values are those outside the diagonal.

Code-Box 1: NGP interpolation

```
1  @jit(nopython=True)
2  def NGP(data, densidad_particle,xmin,ymin,zmin,delta_L,nFFT):
3      for j in range(len(data)):
4          for i in range(3):
5              if data[j, i]>=L:
6                  data[j, i]=data[j, i]-L
7              if data[j, i]<0:
8                  data[j, i]=data[j, i]+L
9          I = np.floor((data[j, 0] - xmin) / delta_L)
10         J = np.floor((data[j, 1] - ymin) / delta_L)
11         K = np.floor((data[j, 2] - zmin) / delta_L)
12         index = int(K + J*nFFT + I*nFFT**2)
13         densidad_particle[index] += 1
14
```

B. Mass assignment scheme

In N-body simulations the mass distribution $\rho(\mathbf{r})$ is represented by a collection of discrete tracers, i.e., $\rho(\mathbf{r}) = \sum_i \delta_D^3(\mathbf{r}-\mathbf{r}_i)$. In order to provide a smooth representation of this quantity, an interpolation on a grid is applied. Different degrees of interpolation (or mass assignment scheme, MAS hereafter) are implemented, represented by a filtering function $W(\mathbf{r})$.

$$\rho(\mathbf{r}_g) = \int \rho(\mathbf{r})W(\mathbf{r}-\mathbf{r}_g)d\mathbf{r} = \sum_i W(\mathbf{r}_i - \mathbf{r}_g), \tag{35}$$

where the vector $\mathbf{r}_g$ takes the values of the centers of the cells in configuration space, $g = L/N_{FFTW}$ is the spatial resolution (minimum distance between two centers), L is the size of the box and N_{FFTW}^3 is the number of cells on the grid (see e.g., Cui et al., 2008, and references therein). First- and second-order MAS used for interpolating particles onto the grid are the *Nearest Grid Points* (NGP) and the *Cloud-In-Cell* (CIC) (Hockney and Eastwood, 1988). In this work we only analyze these two MAS, but we know that higher order MAS can be used, such as, *Triangular Shape Cloud* (TSC) or *Piecewise Cubic Spline* (PCS). Their forms can be described by $W(\mathbf{x}) = \prod_i W(x_i)$, with (see e.g. Cui et al., 2008)

$$W(x_i) = \begin{cases} 1 & |x_i| < 0.5 \\ 0 & \text{else} \end{cases} \qquad \text{NGP}, \tag{36}$$

and,

$$W(x_i) = \begin{cases} 1 - |x_i| & |x_i| < 1 \\ 0 & \text{else} \end{cases} \qquad \text{CIC}, \tag{37}$$

where x_i (i = 1,2,3) is the i-th component of $\mathbf{x}$. This MAS have been computed in this work with the script shown in Code-Boxes 1 and 2.

In Fig. 28 we show the dark matter density field interpolated from the particle distribution using the NGP and the CIC interpolation schemes. There are no very significant changes, although the density field using CIC offers us a much wider and more precise range of values, as we would expect because this scheme spreads the information of the localization of a particle over the nearest cell and over the closest cells to this. Therefore, from now on we will continue to use the interpolation of the CIC because it offers us more precise results than those offered by NGP. Note that the grid selected to do the work is the one with 512^3 cells. A full discussion on the number of cells in the grid is done in Appendix C[10].

---

[10]The discussion in Appendix C has been done by comparing the results of the cosmic-web classification (which will be discussed in §4.2) on each grid.

Code-Box 2: CIC interpolation

```
1  @jit(nopython=True)
2  def CIC(data, densidad_particle, xmin, ymin, zmin, delta_L, nFFT):
3      for j in range(len(data)):
4          for i in range(3):
5              if data[j, i]>=L:
6                  data[j, i]=data[j, i]-L
7              if data[j, i]<0:
8                  data[j, i]=data[j, i]+L
9          I = np.floor((data[j, 0] - xmin) / delta_L)
10         J = np.floor((data[j, 1] - ymin) / delta_L)
11         K = np.floor((data[j, 2] - zmin) / delta_L)
12         dx = (data[j, 0] - xmin) / delta_L - (I + 0.5)
13         dy = (data[j, 1] - ymin) / delta_L - (J + 0.5)
14         dz = (data[j, 2] - zmin) / delta_L - (K + 0.5)
15         paso_x, paso_y, paso_z = (1 if dx >= 0 else -1), (1 if dy >= 0 else -1), (1 if dz >= 0
   else -1)
16         w_x, w_y, w_z = np.array([1 - np.abs(dx), np.abs(dx)]),np.array([1 - np.abs(dy), np.abs(
   dy)]),np.array([1 - np.abs(dz), np.abs(dz)])
17         for di in range(2):
18             for dj in range(2):
19                 for dk in range(2):
20                     if 0 <= I + paso_x * di < nFFT:
21                         ind_i = I + paso_x * di
22                     elif 0 > I + paso_x * di:
23                         ind_i = nFFT-1
24                     elif I + paso_x * di >= nFFT:
25                         ind_i = 0
26                     #(same for ind_j and ind_k)
27                     index = int((ind_i)*nFFT**2+(ind_j)*nFFT+(ind_k))
28                     densidad_particle[index] += w_x[di] * w_y[dj] * w_z[dk]
29
```

C.   Discussion on the number of cells in the grid

In the following section we will see how the cosmic-web classification changes with the number of cells in the mesh. We only analyzing three of the grids (128^3, 256^3 and 512^3). First, we achieved the cosmic-web classification of our simulation from the tidal field using the procedure explained in §4.2. Tab. 7 represents the percentages of each cosmic-web environment for the meshes to be compared. We can observe that, as the number of cells increases, the number of denser structures, such as filaments and knots, decreases in favor of less dense structures, such as sheets and voids. To explain this, let us take an example. Imagine that the mesh of 128^3 cells classifies a random cell as a knot. When classifying that same environment with the mesh of 256^3 cells, it might classify 5 cells as knot, 2 as filament and 1 as sheet (remember that from 1 cell in the 128^3 grid we get 8 in the 256^3 grid) and so on with the biggest one. This will increase the cells classified as sheets and voids at the expense of knots and filaments.

In Fig. 29, we show the probability distribution of the dark matter density plot and the mass function plot, both of them in the four cosmic-web types defined in §4.2. These two plots have been made to compare the resolutions of the different grids to be analyzed.

The information encoded in the upper row in Fig. 29 reveals that as the number of cells in the grid increases, the halos are more distributed in density, i.e., the grid with 128^3 grid cells has values in the range of $\log(\delta_{dm} + 1) = [-1.2, 2.0]$ while the one with 512^3 grid cells has values in range of $\log(\delta_{dm} + 1) = [-1.5, 2.5]$. Moreover, it is evident that increasing the number of cells increases the resolution and, therefore, the accuracy of the classification. This can be seen in the fact that the distributions become smoother and better defined as the number of cells increases. Further evidence of this are the mass functions (shown in the bottom row of Fig. 29), since as the number of cells increases, fewer massive halos are classified as voids and sheets. In summary, the cell that gives us the best results without using a huge amount of computational resources and that we will therefore use to carry out this work will be the 512^3-cell grid.
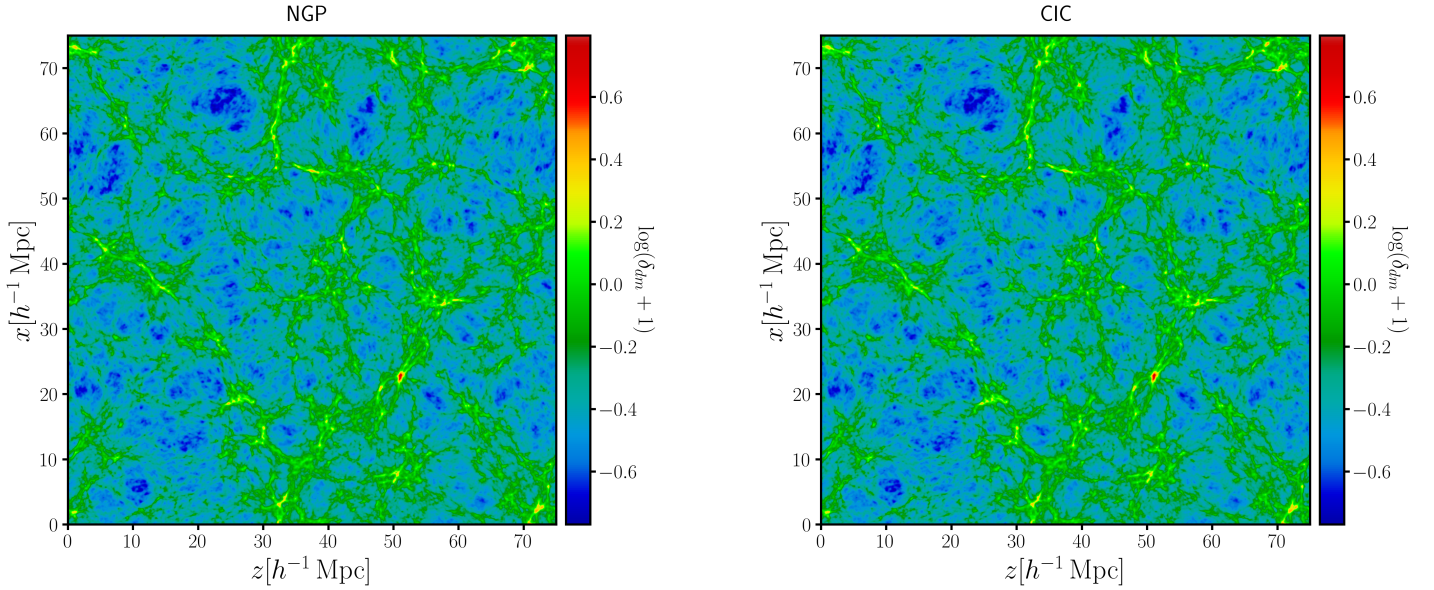
Figure 28: Slices of 10x75x75 h^{-3} Mpc^3 at the TNG100 simulation showing the dark matter density field in a grid of 512^3 cells. On the left the one calculated using NGP interpolation and on the right the one calculated using CIC. The maps are color-coded according to the value of the density in each cell of the grid.

	128^3	256^3	512^3
Void	14.54	15.54	16.53
Sheet	57.23	59.84	61.81
Filament	26.35	23.33	20.77
Knot	1.88	1.29	0.89

Table 7: Percentage of cells classified according to cosmic web classification (as mentioned in §4.2, with $\lambda_{th} = 0$) for the 128^3, 256^3 and 512^3 cell grids respectively at $z = 3$.

D.   Measurement of the power spectrum

The power spectrum shown in § 4.1 has been measured using the fast Fourier transform, which uses a version of the interpolated density field, in this case using CIC. The fast Fourier transform takes this density field and transforms it into a complex vector $\delta(\mathbf{k})$ which given Hermite symmetry provides the positive part on the z-axis of the complex plane, because the negative part on the z-axis can be obtained with the complex conjugate. To measure the power spectrum, we average it in spherical shells, i.e., $P(k) = \langle |\delta(\mathbf{k})|^2 \rangle_{V_k}$, where the bins in k are defined according to the fundamental mode, which is $\Delta k = 2\pi/L_{box} = 0.0838 h\text{Mpc}^{-1}$. The average is done by adding the values of $\delta(\mathbf{k})^2$ in each of those bins and dividing by the number of modes in each of those bins. The error bars shown in the work have been calculated based in a Gaussian approximation whose expression is given by $\sigma_P(k) = \sqrt{2P(k)^2/(VV_k)}$, where $V_k = (4\pi k^2 \Delta_k)/(2\pi)^3$ is the volume of the spherical shell centered at k and width Δ_k (Dodelson, 2003).

Code-Box 3 shows how to calculate the power spectrum and error bars. To do this, we have done the Fourier transform of the density field, to traverse the quadrant defined by k_x, k_y, k_z positive and calculate the power spectrum for all four quadrants, given that the coordinates are k-symmetric. We then define the power spectrum in spherical shells as the amount of the spectrum divided by the number of modes of each shell. This has been normalized to $N = V/N_g^2$, where V is the volume of the simulation box and N_g is the number of cells taken for the grid (see e.g.,). The error bars are given by the Gaussian approximation as described above.

E.   Codes for the calculation of the tidal field and its the eigenvalues

The Code-Box 4, shows how the *i,j* component of the tidal field is constructed. This code was created by us and it consists in the calculus of the Hessian of the overdensity by multiplying a term $k_1 k_2/k^2$ to the Fourier transform of the overdensity and
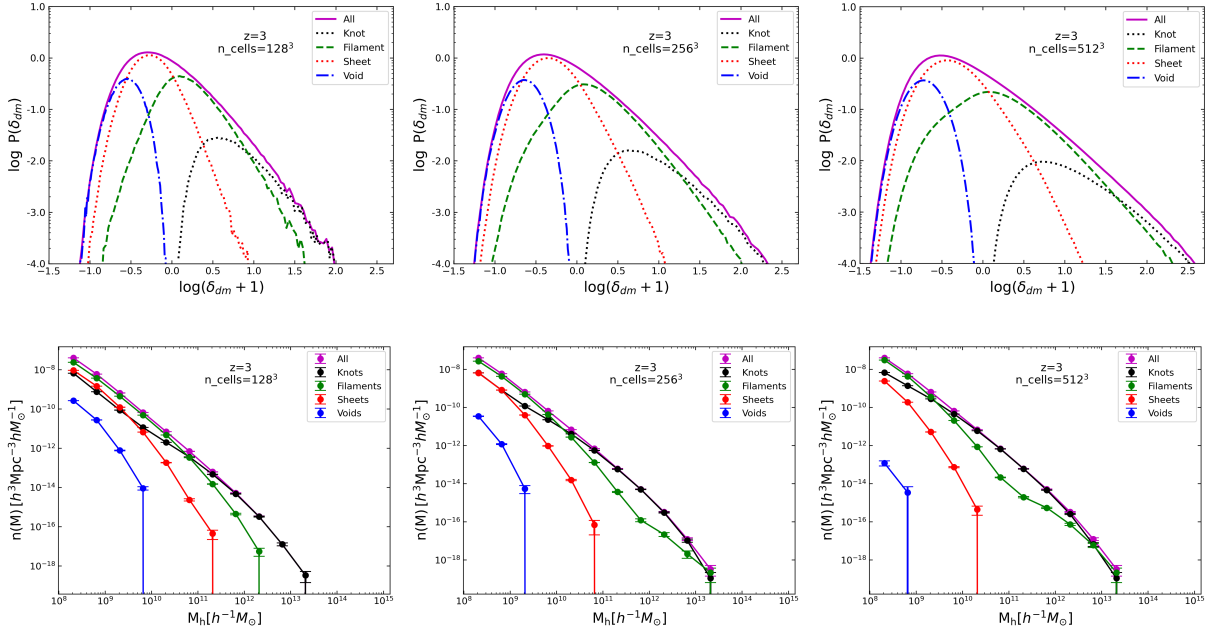
Figure 29: Plots used to compare three different grids, whose number of cells are, from left to right: 128^3, 256^3 and 512^3. Top row: Probability distribution function of the different cosmic-web structures, i.e., knots (in black), filaments (in green), sheets (in red) and voids (in blue) . Bottom row: Binned mass function of haloes residing in the same cosmic-web structures as defined above. The error bars are Poisson's bars, i.e., $n(M)/\sqrt{N}$, where N is the number of objects falling into each bin for each structure. Both plots have been done for the TNG100 simulation at $z = 3$.

then calculating the anti-Fourier transform of the Hessian itself (as previously said, the physical meaning will be discussed in the next section). For this code, we have used the pyFFTW library of Python for obtaining the FT and the anti-FT of it. The Code-Box 5, shows how we calculate the eigenvalues of the tidal field. Consists basically in creating the whole tidal tensor, i.e., the tidal field in each cell of the grid and using `np.linalg.eigvals` compute the eigenvalues for each cell.

Code-Box 3: Calculation of the power spectrum

```python
def power_spec(sobredensidad, nFFT):
    dens = sobredensidad.reshape((nFFT, nFFT, nFFT))
    delta = scipy.fft.rfftn(dens)
    delta_k = 2 * np.pi / L
    coords = np.fft.fftfreq(nFFT, L / nFFT) * 2 * np.pi
    pk = np.zeros((nFFT // 2), dtype=np.float64)
    nk = np.zeros((nFFT // 2), dtype=np.float64)
    k_max = nFFT * np.pi / L
    norm = (L**3) / (nFFT**3)**2
    for i in range(nFFT // 2):
        for j in range(nFFT // 2):
            for k in range(nFFT // 2 + 1):
                kv = np.sqrt(coords[i] ** 2 + coords[j] ** 2 + coords[k] ** 2)
                if kv != 0 and kv < k_max:
                    kbin = int(np.floor((kv - 0.) / delta_k))
                    pk[kbin] += delta[i, j, k].real**2 + delta[i, j, k].imag**2
                    nk[kbin] += 1
                    if j > 0 and k > 0:
                        pk[kbin] += delta[i, nFFT - j, k].real**2 + delta[i, nFFT - j, k].imag**2
                        nk[kbin] += 1
                    if i > 0 and (j > 0 or k > 0):
                        pk[kbin] += delta[nFFT - i, j, k].real**2 + delta[nFFT - i, j, k].imag**2
                        nk[kbin] += 1
                    if i > 0 and j > 0 and k > 0:
                        pk[kbin] += delta[nFFT - i, nFFT - j, k].real**2 + delta[nFFT - i, nFFT - j, k].imag**2
                        nk[kbin] += 1
    bin_k = np.arange(0, k_max + 1e-2, step=delta_k)
    x = (bin_k[1:] + bin_k[:-1]) / 2
    power_spectrum = np.empty((nFFT // 2), dtype=np.float64)
    desv = np.empty((nFFT // 2), dtype=np.float64)
    power_spectrum = pk / nk * norm
    vk = 4 * np.pi * x**2 * delta_k / (2 * np.pi)**3
    desv = np.sqrt(2 / (L**3 * vk) * (power_spectrum**2))
    return x, power_spectrum, desv
```

Code-Box 4: Calculation of the component i j of the tidal field

```python
def tidal_field_in_ij_SP(densidad, nFFT, ind_1, ind_2):
    dens=densidad.reshape((nFFT,nFFT,nFFT))
    fft_densidad= scipy.fft.rfftn(dens)
    coords = np.fft.fftfreq(nFFT, L / nFFT) * 2 * np.pi
    Tij = np.empty((nFFT , nFFT , nFFT),dtype='float32')
    hessian = pyfftw.empty_aligned(fft_densidad.shape, dtype='complex64')
    for i in range(nFFT):
        for j in range(nFFT):
            for k in range(nFFT//2+1):
                ind = index_3d(i,j,k,nFFT,(nFFT//2+1))
                kv2 = coords[i] ** 2 + coords[j] ** 2 + coords[k] ** 2
                if ind_1 == 0:
                    k1 = coords[i]
                elif ind_1 == 1:
                    k1 = coords[j]
                elif ind_1 == 2:
                    k1 = coords[k]
                if ind_2 == 0:
                    k2 = coords[i]
                elif ind_2 == 1:
                    k2 = coords[j]
                elif ind_2 == 2:
                    k2 = coords[k]
                term = 0.
                if kv2 > 0:
                    term = (k1 * k2) / kv2
                hessian[i,j,k] = term * fft_densidad[i,j,k]
    Tij = scipy.fft.irfftn(hessian)
    Tij_resh=Tij.reshape(nFFT**3)
    return Tij_resh
```

Code-Box 5: Calculation of the eigenvalues of the tidal field

```python
def eigenvalues_SP(densidad,nFFT):
    tidal_11=tidal_field_in_ij_SP(densidad,nFFT,0,0)
    (...)
    tidal_33=tidal_field_in_ij_SP(densidad,nFFT,2,2)
    matriz=np.empty((len(tidal_11),3,3))
    for i in range(len(tidal_11)):
        matriz[i]=np.array([tidal_11[i],tidal_12[i],tidal_13[i],&
                            tidal_21[i],tidal_22[i],tidal_23[i],&
                            tidal_31[i],tidal_32[i],tidal_33[i]]).reshape((-1,3,3))
    eig=np.linalg.eigvals(matriz)
    eig.sort()
    return eig
```